REPORT NO.
UCD/CGM-23/02

CENTER FOR GEOTECHNICAL MODELING

PM4SILT (VERSION 2.1): A SILT PLASTICITY MODEL FOR EARTHQUAKE ENGINEERING APPLICATIONS

BY

R. W. BOULANGER

K. ZIOTOPOULOU

UCDAVIS

DEPARTMENT OF CIVIL & ENVIRONMENTAL ENGINEERING
COLLEGE OF ENGINEERING
UNIVERSITY OF CALIFORNIA AT DAVIS

February 2023
(Revised June 2023)

PM4Silt (Version 2.1):
A Silt Plasticity Model for Earthquake Engineering Applications

by

Ross W. Boulanger

and

Katerina Ziotopoulou

Report No. UCD/CGM-23/02

Center for Geotechnical Modeling
Department of Civil and Environmental Engineering
University of California
Davis, California

February 2023
(revised June 2023)

First Edition (PM4Silt Version 1) January 2018

Revised July 2018

Second Edition (PM4Silt Version 2) July 2022

Revised (PM4Silt Version 2.1) February 2023

Revised June 2023

ABSTRACT

The PM4Silt plasticity model for representing clays and plastic silts in geotechnical earthquake engineering applications is presented herein. The PM4Silt model builds on the framework of the stress ratio-controlled, critical state-based, bounding surface plasticity PM4Sand model (Version 3.2) described in Boulanger and Ziotopoulou (2022) and Ziotopoulou and Boulanger (2016). Modifications to the model were developed and implemented to improve its ability to approximate undrained monotonic and cyclic loading responses of clays and plastic silts, as opposed to those for purely nonplastic silts or sands. Emphasis was given to obtaining reasonable approximations of undrained monotonic shear strengths, undrained cyclic shear strengths, and shear modulus reduction and hysteretic damping responses across a range of initial static shear stress and overburden stress conditions. The model does not include a cap, and therefore is not suited for simulating consolidation settlements or strength evolution with consolidation stress history. The model is cast in terms of the state parameter relative to a linear critical state line in void ratio versus logarithm of mean effective stress. The primary input parameters are the undrained shear strength ratio (or undrained shear strength) at critical state, the shear modulus coefficient, the contraction rate parameter, and an optional post-strong-shaking shear strength reduction factor. All secondary input parameters are assigned default values based on a generalized calibration. Secondary parameters that are most likely to warrant adjustment based on site-specific laboratory test data include the shear modulus exponent, plastic modulus coefficient (adjusts modulus reduction with shear strain), bounding stress ratio parameters (affects peak friction angles and undrained stress paths), fabric-related parameters (affects rate of shear strain accumulation at larger strains and shape of stress-strain hysteresis loops), maximum excess pore pressure ratio, initial void ratio, and compressibility index. The model is coded as a user defined material in a dynamic link library (DLL) for use with the commercial programs FLAC 8.1 (Itasca 2019) and FLAC2D 9.00 (Itasca 2023). The numerical implementation and DLL module are described. The behavior of the model is illustrated by simulations of element loading tests covering a range of conditions, including undrained monotonic and cyclic loading under a range of initial confining and shear stress conditions. The model is shown to provide reasonable approximations of behaviors important to many earthquake engineering applications and to be relatively easy to calibrate.

TABLE OF CONTENTS

PM4Silt (Version 2.1): A Silt Plasticity Model for Earthquake Engineering Applications

1. INTRODUCTION

Nonlinear seismic deformation analyses in geotechnical practice require approximating the stress-strain responses of a broad range of soil types and consistencies. Soil types can span from clearly sand-like (e.g., clean sands, gravels, gravelly sands) to clearly clay-like (e.g., sedimentary high plasticity clays), with a broad range of intermediate soil types that are more difficult to characterize (e.g., low plasticity clays and silts, sandy clays and silts, and clayey and silty sands). Soil consistency can range from loose or soft to dense or hard in natural deposits or man-made fills. The choice of engineering procedures for characterizing a soil's properties (e.g., correlations, in-situ tests, laboratory tests) depends on its type and consistency, along with a number of project-specific considerations. The choice of a constitutive model for representing a specific soil in a nonlinear dynamic analysis (NDA) similarly depends on the soil type, its consistency, and a number of project-specific considerations.

Constitutive models for representing sand and sand-like soils in two-dimensional (2D) or three-dimensional (3D) NDAs range from relatively simplified, uncoupled cycle-counting models to more complex plasticity models (e.g., Wang et al. 1990, Cubrinovski and Ishihara 1998, Dawson et al. 2001, Papadimitriou et al. 2001, Yang et al. 2003, Byrne et al. 2004, Dafalias and Manzari 2004, Boulanger and Ziotopoulou 2020, Yang et al. 2022). Each constitutive model has certain advantages and limitations that can be illustrated by examining the constitutive response of the model in single element simulations that cover the range of the loading conditions important to various applications in practice.

Constitutive models for representing clay and clay-like soils in 2D or 3D NDAs are relatively limited by comparison to those available for sands. The elastic-plastic Mohr Coulomb model is widely used in practice, which may be attributed to its simplicity, wide availability, and lack of alternatives. More complex plasticity models for clay are available that focus on stress-strain behaviors important for static problems (e.g., Pestana and Whittle 1999) and cyclic loading responses (e.g., Dafalias et al. 2006, Yang et al. 2008, Taiebat et al. 2010, Seidalinov and Taiebat 2014, Hu and Liu 2015, Ni et al. 2015, Qiu and Elgamal 2020), but there remains a need for implementation and validation of these types of models in the various analysis programs most commonly used in engineering practice. For some geotechnical structures and loading conditions, the simple Mohr Coulomb model may prove adequate for representing the clay-like materials in the system, particularly if the overall response and deformations are more strongly controlled by other soil types (e.g., liquefiable soils). For other geotechnical structures and loading conditions, the limitations of the Mohr Coulomb model can raise significant concerns regarding the reliability of the computed responses and deformations.

The selection of a constitutive model for representing low-plasticity silts and clays in 2D or 3D NDAs requires even greater compromises in practice. Low-plasticity silts and clays can exhibit behaviors that range from sand-like in some aspects to clay-like in other aspects (Boulanger and Idriss 2006), such that constitutive models developed for either sand or clay may not reproduce certain behaviors that the analyst suspects may be important to the system response. Nonetheless, most efforts at modeling cyclic loading responses of intermediate soil types have involved adjustments to existing models for sand to improve certain aspects of behavior. For example, efforts have been made toward

adjusting the UBCSAND model to produce stress-strain responses that better approximate responses of low-plasticity silts for specific projects (E. Naesgaard, personal communication 2017).

The information available for the calibration of constitutive models in design practice varies with the soil type. For sands and sand-like soils, the information will most commonly include basic classification index tests (e.g., grain size distributions), penetration resistances (e.g., SPT or CPT), and shear wave velocity (V_s) measurements. For clays and clay-like soils, the information can also include laboratory strength and consolidation test data for field samples, results of other in-situ tests (e.g., vane shear test), and knowledge of a site's consolidation stress history. For low-plasticity silts and clays, the availability and quality of any laboratory strength and consolidation test data can depend on the nature of the soil and project-specific considerations (e.g., future loading conditions), which determine whether the influence of sampling disturbance can be reasonably assessed or managed (e.g., Hoeg et al. 2000, Dahl et al. 2010).

Constitutive models for geotechnical earthquake engineering applications must be able to approximate the range of conditions encountered in the field. For example, a single geotechnical structure like the schematic earth dam shown in Figure 1.1 can have strata or zones ranging from very loose (or soft) to dense (or hard) under a wide range of confining stresses, initial static shear stresses (e.g., at different points beneath the slope), drainage conditions (e.g., above and below the water table), and loading conditions (e.g., various levels of shaking). The engineering effort is greatly reduced if the constitutive model can reasonably approximate the predicted stress-strain behaviors under all these different conditions. If the model cannot approximate the trends across all these conditions, then extra engineering effort is required in deciding what behaviors should be prioritized in the calibration process, and sometimes by the need to repeat the calibrations for the effects of different initial stress conditions within the same geotechnical structure.

The PM4Silt (Version 2.1) plasticity model for low-plasticity silts and clays in geotechnical earthquake engineering applications is presented herein. The PM4Silt model builds on the framework of the stress ratio-controlled, critical state-based, bounding surface plasticity PM4Sand model (Version 3.2) described in Boulanger and Ziotopoulou (2022) and Ziotopoulou and Boulanger (2016). Modifications to the model were developed and implemented to improve its ability to approximate undrained monotonic and cyclic loading responses of low-plasticity silts and clays, as opposed to those for purely nonplastic silts or sands (Boulanger and Ziotopoulou 2019). The following stress-strain responses and engineering correlations were of primary focus in the development of the PM4Silt model:

- Monotonic undrained shear strengths (s_u) for low-plasticity silts and clays often exhibit a stress-history normalization, with undrained shear strength ratios (e.g., s_u/σ'_{vc}) being strongly dependent on the soil's over-consolidation ratio (OCR) (e.g., Figure 1.2).
- Undrained cyclic loading of soft low-plasticity silts and clays can generate significant excess pore pressures (Δu) and rapid accumulation of cyclic shear strains (e.g., Figures 1.3, 1.4, and 1.5), even if the excess pore water pressure ratios (e.g., $r_u = \Delta u/\sigma'_{vc}$ in direct simple shear loading) do not reach 100%.
- Undrained cyclic strength can often be normalized by the monotonic undrained shear strength, to arrive at a cyclic strength ratio (τ_{cyc}/s_u) that depends on the failure criterion (e.g., a peak shear strain) and number of uniform loading cycles (e.g., Figures 1.6 and 1.7). Cyclic and monotonic strengths generally increase with loading rate, such that τ_{cyc}/s_u can exceed unity at small

numbers of loading cycles because τ_{cyc} is measured at fast loading rates (applicable to earthquake loading) whereas s_u is commonly measured at standardized slow loading rates (applicable to static loading). The slope of the τ_{cyc}/s_u versus number of loading cycles curve (Figure 1.6) is flatter than observed for most sands. The influence of overburden stress is accounted for by its effects on s_u and OCR, such that τ_{cyc}/s_u is relatively unaffected.

- The presence of initial static shear stress reduces cyclic strengths, with the influence being greatest for normally consolidated soils and decreasing with increasing OCR or s_u/σ'_{vc} ratio (e.g., Figures 1.8 and 1.9).
- Shear modulus and hysteretic damping behaviors for low-plasticity silts and clays vary with consolidation stress, consolidation stress history, mineralogy [e.g., often represented by indices like the plasticity index (PI)], age, and other factors (e.g., Kokusho et al. 1982, Vucetic and Dobry 1991). The small-strain shear modulus (G_{max}) for these soils can have weaker or stronger dependence on the effective confining stress than for sands depending on these various factors. Relationships for secant shear modulus reduction (G/G_{max}) and equivalent damping ratios versus cyclic shear strain amplitude become less nonlinear (for the same strain amplitude) with increasing PI (e.g., Figure 1.10) and show less dependence on confining stress than observed for sands (e.g., Kokusho et al. 1982, Vucetic and Dobry 1991).

The PM4Silt model does not include a cap and therefore is not suited for simulating consolidation processes, predicting consolidation settlements, or predicting the evolution of undrained shear strength with consolidation stress history. The model is also not formulated to approximate anisotropic strengths and is currently limited to plane strain applications.

The organization of this report is structured as follows:

- Section 2 of this report contains a description of the model formulation.
- Section 3 contains a description of the model's implementation as a user defined material in a dynamic link library for use in the commercial program FLAC 8.1 (Itasca 2019).
- Section 4 of this report contains a summary of the model input parameters, guidance on model parameter selections, and illustrations of the model responses to a range of elemental loading conditions.
- Section 5 contains summary remarks regarding the model and its use in practice.

Revisions to PM4Silt in Version 2 relative to Version 1 include a revision to the initial back-stress ratio initialization routine and a modification to the elastic shear modulus equation. The initial back-stress ratio at the time of model initialization is now limited to have a magnitude that is no greater than 90% of the bounding surface stress ratio (M^b); this constraint eliminates a problem that can occur when the model is initialized with consolidation stress states that are outside the bounding surface. The equation for the elastic shear modulus includes a C_{SR} term that reduces the elastic shear modulus at stress ratios close to the bounding surface. The C_{SR} term is normalized in Version 2 to produce a value of unity at the time of model initialization, which simplifies calibration of the model. The C_{SR} term is further restricted to values less than or equal to unity (February 2023 Version 2.1). These changes do not significantly affect the general features of model responses, but do affect responses for a given set of calibration parameters. Therefore, calibrations may need to be revised when switching from PM4Silt Version 1 to Version 2 or from Version 2 to Version 2.1.

The simulations presented in this report were prepared using FLAC 8.1 with the PM4Silt Version 2.1 DLL module *modelpm4silt005_64.dll* compiled on February 2, 2023; note that the compilation date is included in the properties of the DLL file. This DLL module was compiled using Microsoft Visual Studio Community 2015 C++.

PM4Silt Version 2.1 was subsequently compiled for use with FLAC2D 9.00. The PM4Silt Version 2.1 DLL module *cmodelPM4Silt2D009.dll* was compiled on June 12, 2023, and produces the same responses as obtained with the FLAC 8.1 version. This DLL module was compiled using Microsoft Visual Studio Community 2022 C++.

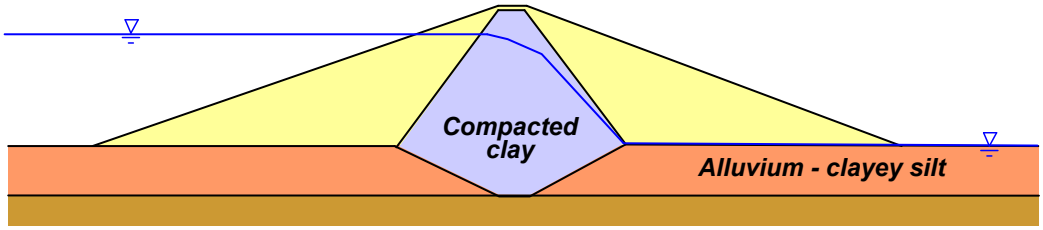

Figure 1.1. Schematic cross-section for an earth dam with a clay core and a clayey silt foundation.

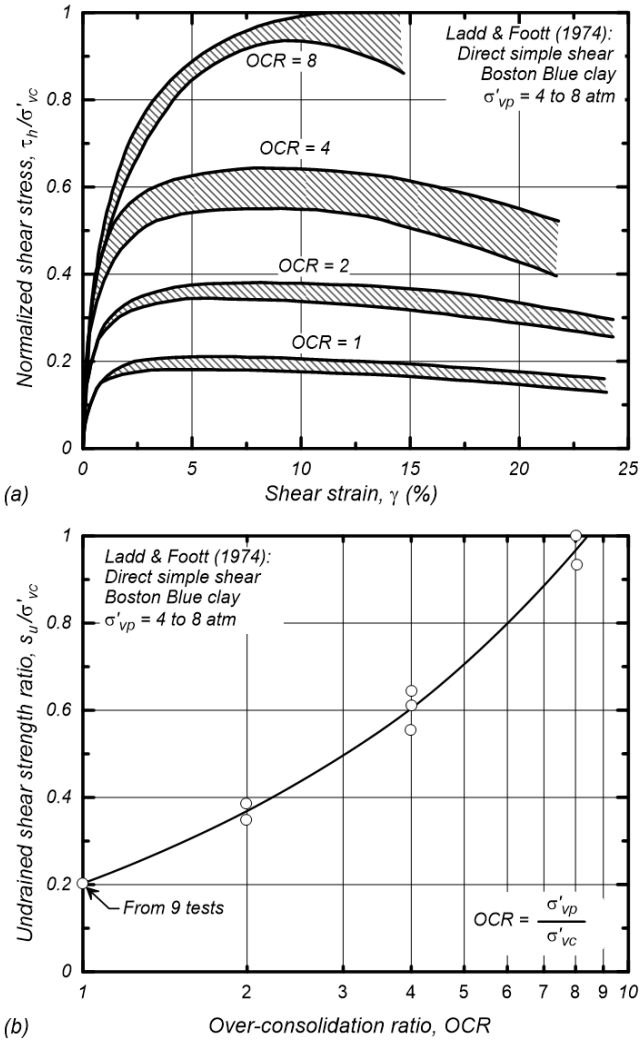

Figure 1.2. Normalized shear stress versus shear strain response of Boston Blue clay in undrained direct simple shear tests on samples with preconsolidation stresses of 400 to 800 kPa and OCR of 1, 2, 4 and 8, and the variation of normalized shear strength versus OCR (Ladd and Foott 1974).

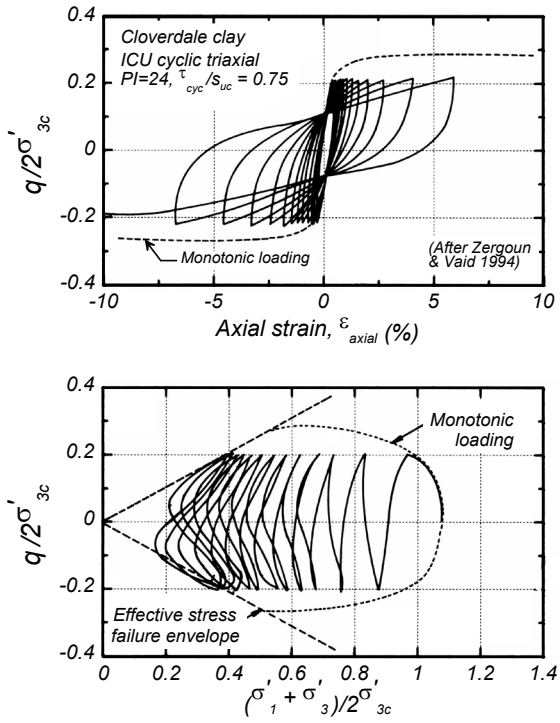

Figure 1.3. Stress-strain le clay during undrained slow cyclic loading (Zergoun and Vaid 1994).

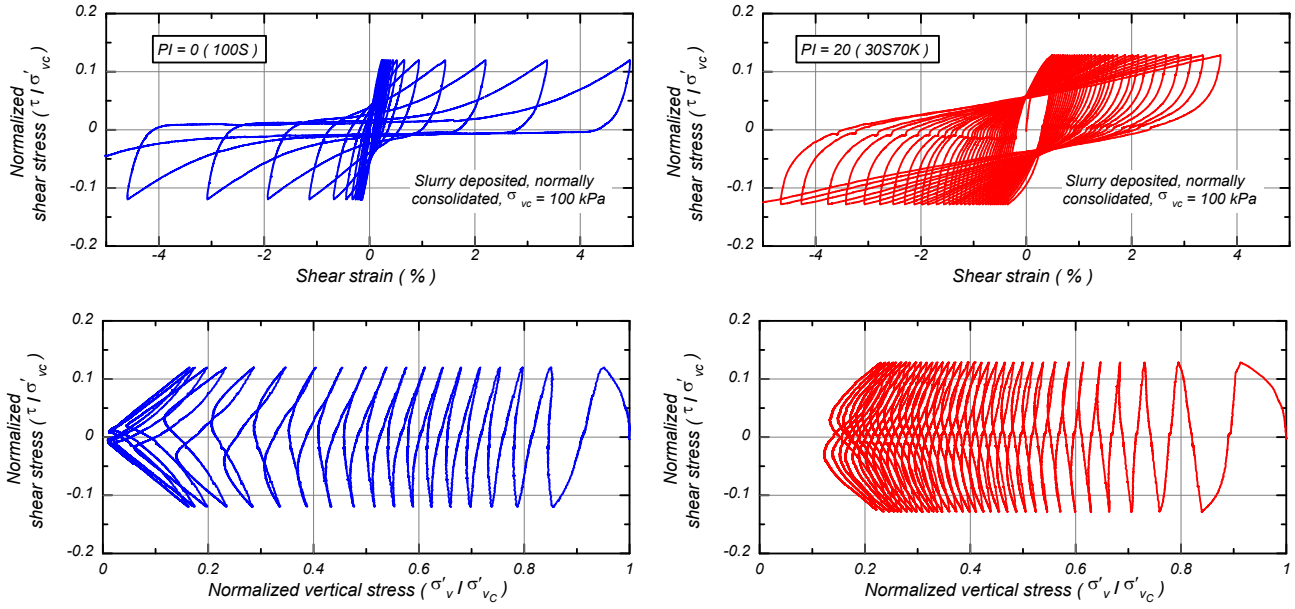

Figure 1.4. Undrained cyclic direct simple shear test results for normally consolidated, slurry sedimented specimens of PI=0 silt (left side) and PI=20 clayey silt (right side) (Boulanger et al. 2016).

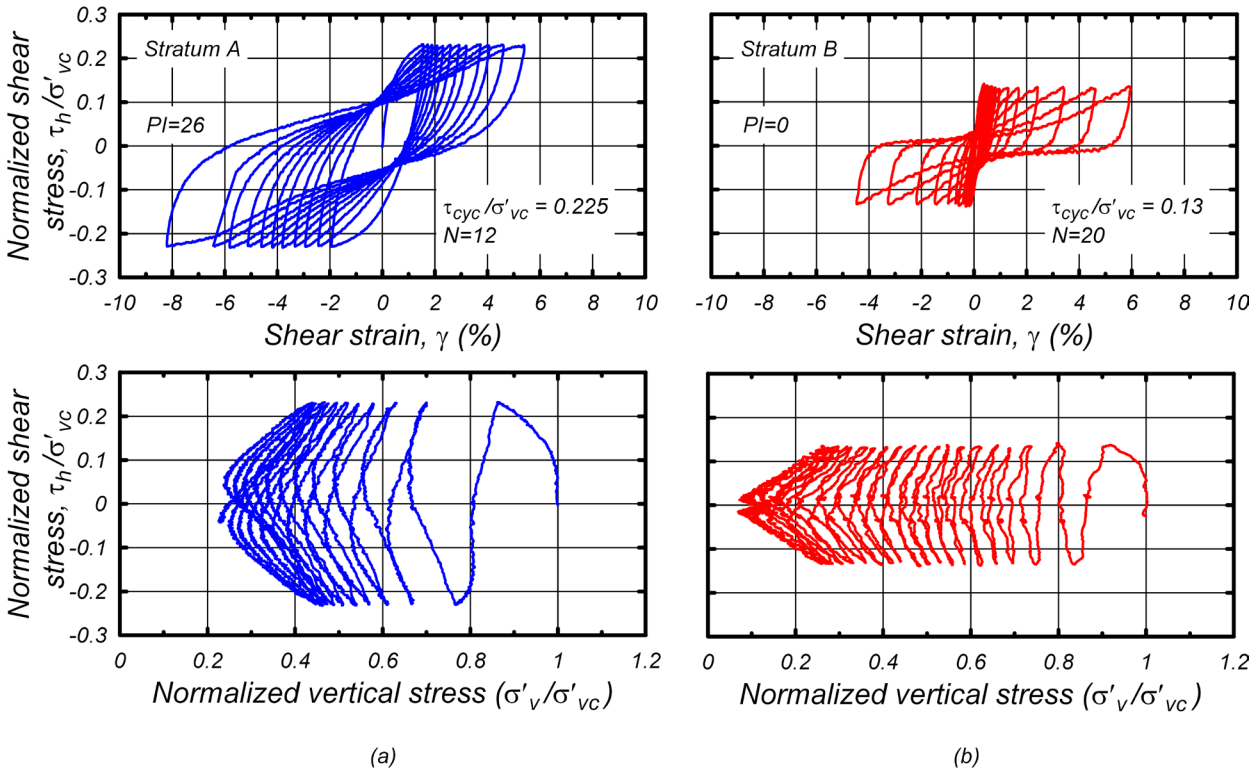

Figure 1.5. Undrained cyclic direct simple shear tests results for undisturbed field samples from Potrero Canyon (Dahl et al. 2014): (a) Stratum A of soft clay and loose silt, and (b) Stratum B of loose silty sand and sandy silt.

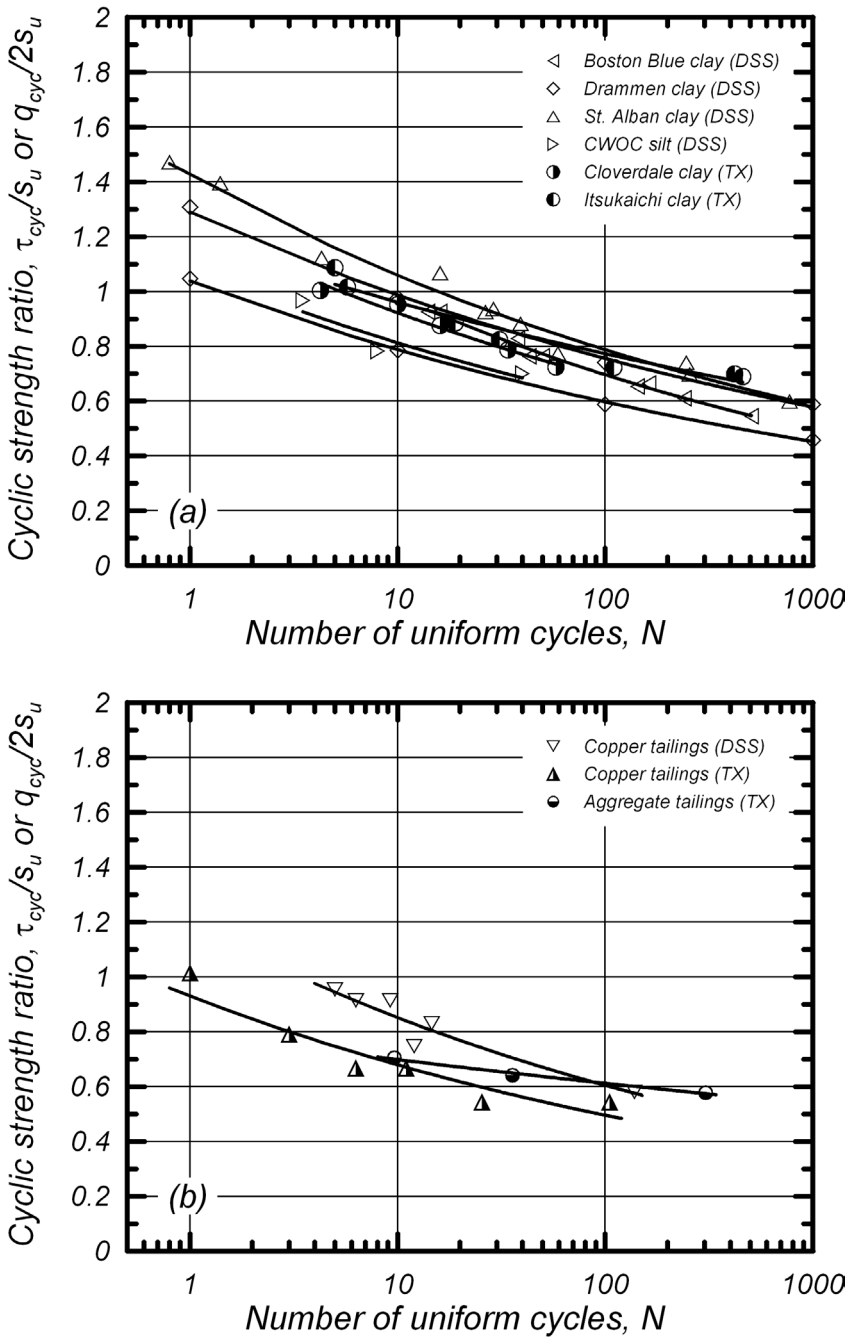

Figure 1.6. Cyclic strength ratios to cause a peak shear strain of 3% versus number of uniform loading cycles at a frequency of 1 Hz (from Boulanger and Idriss 2007):
(a) samples from natural deposits [Andersen et al. 1988, Azzouz et al. 1989, Hyodo et al. 1994, Lefebvre and Pfendler 1996, Woodward-Clyde 1992a, Zergoun and Vaid 1994], and
(b) samples from tailings deposits [Moriwaki et al. 1982, Romero 1995, Woodward-Clyde 1992b].

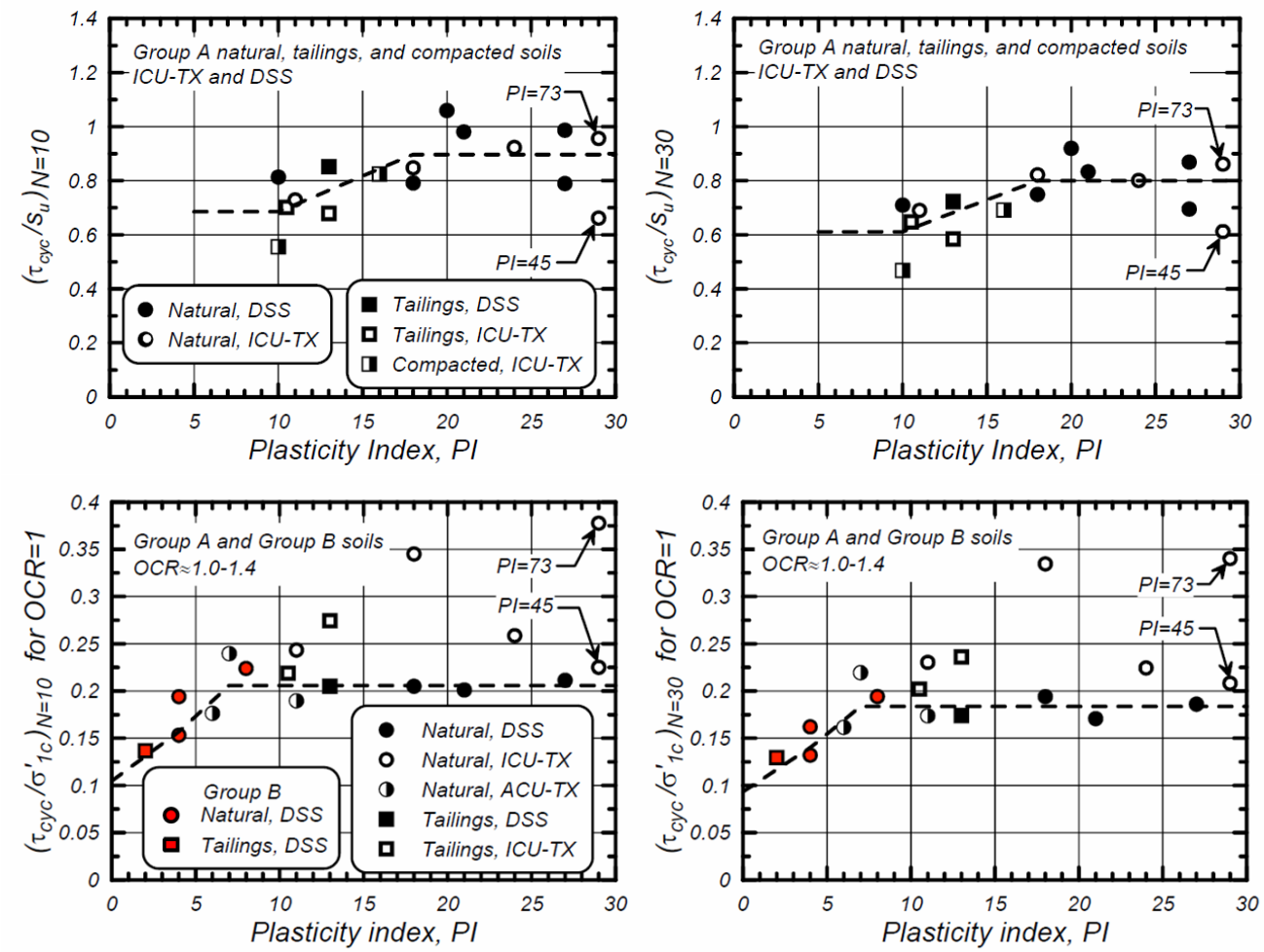

Figure 1.7. Variations in cyclic strength ratios with plasticity index for fine-grained soils: Group A soils exhibiting clearly clay-like behaviors, and Group B soils exhibiting intermediate behaviors in some aspects (Dahl 2011).

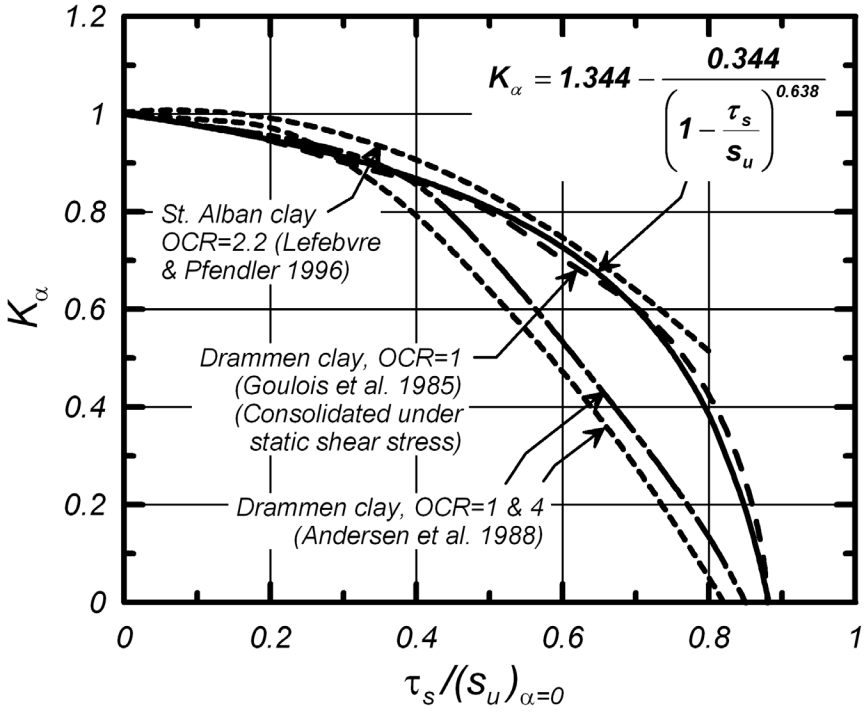

Figure 1.8. K_α versus $\tau_s/(s_u)_{\alpha=0}$ relation for clay-like soils; note that specimens were not consolidated under the static shear stress except as otherwise noted (Boulanger and Idriss 2007).

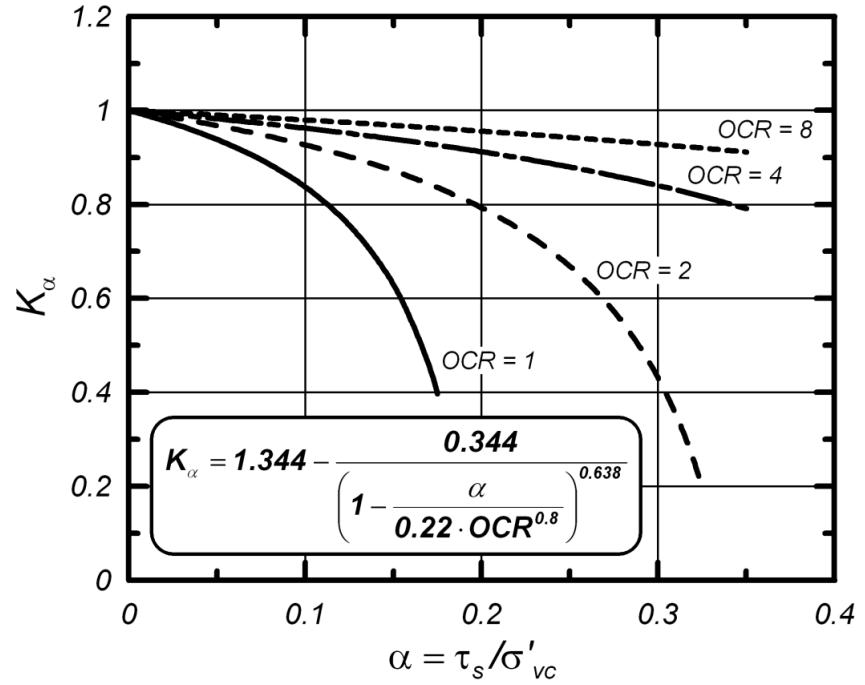

Figure 1.9. K_α factor describing the effect that sustained static shear stress ratio ($\alpha=\tau_s/\sigma'_{vc}$) has on cyclic resistance ratio of sands (Boulanger and Idriss 2007).

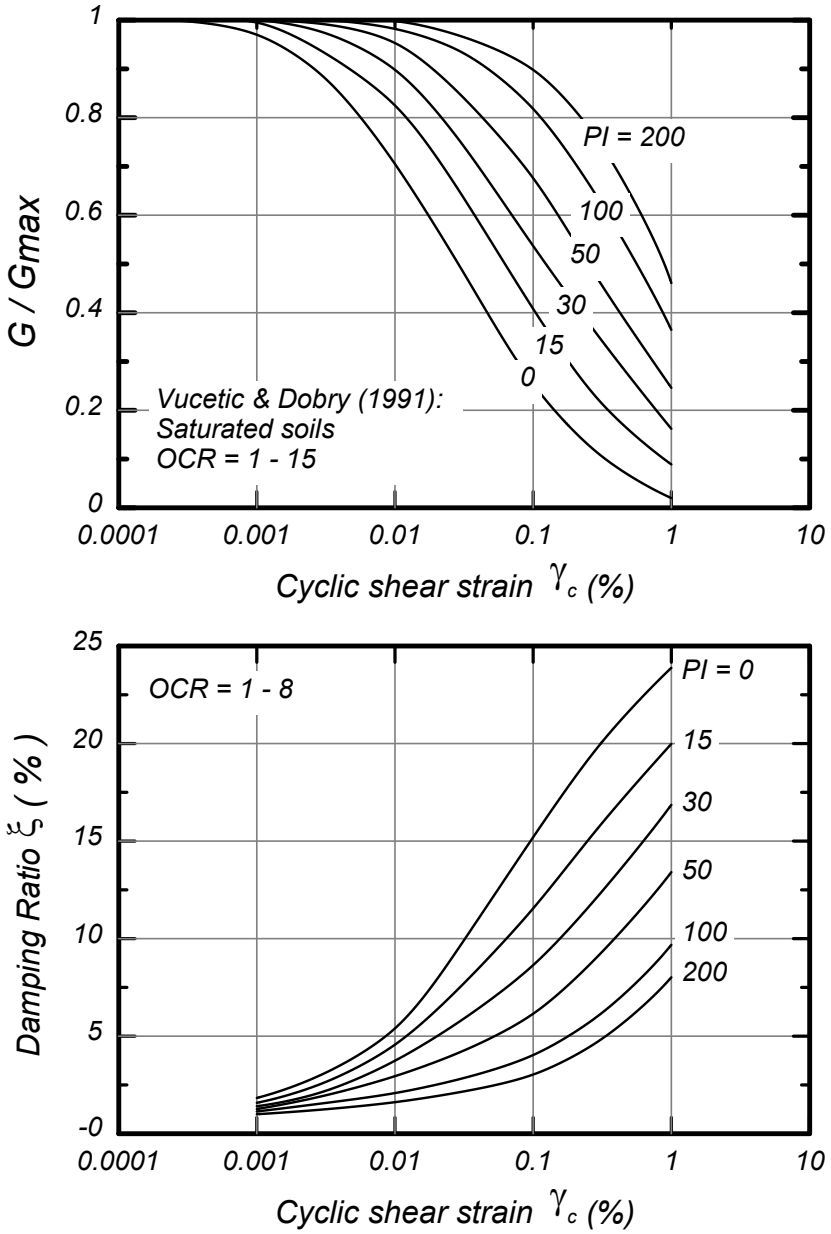

Figure 1.10. Shear modulus reduction and equivalent damping ratio relationship for clays (Vucetic and Dobry 1991).

2. MODEL FORMULATION

The PM4Silt model presented herein follows the basic framework of the stress ratio-controlled, critical state based, bounding surface plasticity PM4Sand (Version 3.2) model presented by Boulanger and Ziotopoulou (2022) and Ziotopoulou and Boulanger (2016). The PM4Sand model was built on the framework provided by Dafalias and Manzari (2004), which had extended the previous work by Manzari and Dafalias (1997) by adding a fabric-dilatancy related tensor quantity to account for the effect of fabric changes during loading. The fabric-dilatancy related tensor was used to macroscopically model the effect that microscopically-observed changes in sand fabric during plastic dilation have on the contractive response upon reversal of loading direction. Dafalias and Manzari (2004) provide a detailed description of the motivation for the model framework, beginning with a triaxial formulation that simplifies its presentation, followed by a multi-axial formulation. Additional background information on the PM4Sand model (Version 3.2) is provided in Boulanger and Ziotopoulou (2022) and Ziotopoulou and Boulanger (2016). Details of PM4Silt Version 1 were also published in Boulanger and Ziotopoulou (2019). The user is referred to the above publications for background information and details.

2.1 Basic stress and strain terms

The basic stress and strain terms for the model are as follows. The model is based on effective stresses, with the conventional prime symbol dropped from the stress terms for convenience because all stresses are effective for the model. The stresses are represented by the tensor $\boldsymbol{\sigma}$, the principal effective stresses σ_1, σ_2, and σ_3, the mean effective stress p, the deviatoric stress tensor **s**, and the deviatoric stress ratio tensor **r**. The present implementation was simplified by casting the various equations and relationships in terms of the in-plane stresses only. This limits the present implementation to plane-strain applications and is not correct for general cases, but it has the advantage of simplifying the implementation and improving computational speed by reducing the number of operations. Expanding the implementation to include the general case should not affect the general features of the model. Consequently, the relationships between the various stress terms can be summarized as follows:

$$\boldsymbol{\sigma} = \begin{pmatrix} \sigma_{xx} & \sigma_{xy} \\ \sigma_{xy} & \sigma_{yy} \end{pmatrix} \tag{1}$$

$$p = \frac{\sigma_{xx} + \sigma_{yy}}{2} \tag{2}$$

$$\boldsymbol{s} = \boldsymbol{\sigma} - p\boldsymbol{I} = \begin{pmatrix} s_{xx} & s_{xy} \\ s_{xy} & s_{yy} \end{pmatrix} = \begin{pmatrix} \sigma_{xx} - p & \sigma_{xy} \\ \sigma_{xy} & \sigma_{yy} - p \end{pmatrix} \tag{3}$$

$$\boldsymbol{r} = \frac{\boldsymbol{s}}{p} = \begin{pmatrix} r_{xx} & r_{xy} \\ r_{xy} & r_{yy} \end{pmatrix} = \begin{pmatrix} \dfrac{\sigma_{xx} - p}{p} & \dfrac{\sigma_{xy}}{p} \\ \dfrac{\sigma_{xy}}{p} & \dfrac{\sigma_{yy} - p}{p} \end{pmatrix} \tag{4}$$

Note that the deviatoric stress and deviatoric stress ratio tensors are symmetric with $r_{xx} = -r_{yy}$ and $s_{xx} = -s_{yy}$ (meaning a zero trace), and that **I** is the identity matrix.

The model strains are represented by a tensor **ε**, which can be separated into the volumetric strain ε_v and the deviatoric strain tensor **e**. The volumetric strain is,

$$\varepsilon_v = \varepsilon_{xx} + \varepsilon_{yy} \tag{5}$$

and the deviatoric strain tensor is,

$$\boldsymbol{e} = \boldsymbol{\varepsilon} - \frac{\varepsilon_v}{3} I = \begin{pmatrix} \varepsilon_{xx} - \dfrac{\varepsilon_v}{3} & \varepsilon_{xy} \\ \varepsilon_{xy} & \varepsilon_{yy} - \dfrac{\varepsilon_v}{3} \end{pmatrix} \tag{6}$$

In incremental form, the deviatoric and volumetric strain terms are decomposed into an elastic and a plastic part,

$$d\boldsymbol{e} = d\boldsymbol{e}^{el} + d\boldsymbol{e}^{pl} \tag{7}$$

$$d\varepsilon_v = d\varepsilon_v^{el} + d\varepsilon_v^{pl} \tag{8}$$

where

$d\boldsymbol{e}^{el}$ = elastic deviatoric strain increment tensor
$d\boldsymbol{e}^{pl}$ = plastic deviatoric strain increment tensor
$d\varepsilon_v^{el}$ = elastic volumetric strain increment
$d\varepsilon_v^{pl}$ = plastic volumetric strain increment

2.2 Critical state

The model presented herein uses the state parameter (ξ) (Been and Jefferies 1985), which is the difference between the current void ratio (e) and the critical state void ratio (e_{cs}) at the same mean effective stress (p). The critical state line is approximated as linear in void ratio versus natural logarithm

of mean effective stress space, with a slope λ and intercept e_{1kPa} when p' = 1 kPa. Thus, the void ratio at critical state (e_{cs}) is related to the mean effective stress at critical state (p_{cs}) by the following expression,

$$e_{cs} = e_{1kPa} - \lambda \cdot \ln\left(\frac{p}{1kPa}\right) \tag{9}$$

$$\xi = e - e_{cs} \tag{10}$$

The relationship between the critical state line and above parameters is shown in Figure 2.1. For silts and clays with sufficient plasticity to exhibit stress history normalization of strengths, the slope of the critical state line is often approximately parallel to the slope of the virgin consolidation line (C_c). The value of C_c is generally taken as the slope in void ratio versus logarithm (base 10) of mean effective stress space, and thus C_c and λ are related as,

$$\lambda = \frac{\log(10)}{\ln(10)} C_c = 0.434 \cdot C_c \tag{11}$$

2.3 Bounding, dilatancy, and critical surfaces

The model incorporates bounding, dilatancy, and critical stress ratio surfaces. The bounding and dilatancy surfaces are functions of the state parameter, and collapse to the critical stress ratio surface when the state parameter is zero. Lode angle dependency was removed to simplify the model (e.g., friction angles are the same for compression or extension loading).

The dilatancy (M^d) ratio is related to the critical stress ratio (M) by the expression,

$$M^d = M \cdot \exp\left(n^d \xi\right) \tag{12}$$

where the model parameter n^d is a positive number so that M^d is smaller than M for dense-of-critical states and greater than M for loose-of-critical states. For the present implementation, the mean normal stress p is taken as the average of the in-plane normal stresses (Equation 2), q is the difference in the major and minor principal in-plane stresses, and the relationship for M is reduced to,

$$M = 2 \cdot \sin\left(\phi_{cv}\right) \tag{13}$$

where ϕ_{cv} is the constant volume or critical state effective friction angle.

The bounding (M^b) ratio has different forms for dense- versus loose-of-critical states. For loose-of-critical states (i.e., the "wet" side), M^b is related to M by the expression,

$$M^b = M \cdot \exp\left(-n^{b,wet}\xi\right) \tag{14}$$

where the model parameter $n^{b,wet}$ is a positive number so that M^b is smaller than M on the wet side. For dense-of-critical states (i.e., the "dry" side), M^b is related to M by the expression,

$$M^b = M \cdot \left(\frac{1 + C_{Mb}}{\frac{p}{p_{cs}} + C_{Mb}} \right)^{n^{b,dry}} \tag{15}$$

$$C_{Mb} = \frac{1}{\left(\frac{M^{b,\max}}{M} \right)^{1/n^{b,dry}} - 1} \tag{16}$$

$$M^{b,\max} = 2 \cdot \sin\left(\phi_{\max}\right) \tag{17}$$

The above expression produces M^b values that smoothly vary from equal to M at critical state (i.e., $p/p_{cs} = 1$) to a maximum value $M^{b,max}$ at the origin (i.e., $p = 0$). The value of $M^{b,max}$ corresponds to the maximum friction angle than can be mobilized near the origin, ϕ_{max}.

For a fixed value of state parameter (with corresponding fixed values for p/p_{cs}, M^d, and M^b), the bounding, dilatancy, and critical stress ratio surfaces can be visualized as linear lines on a q-p plot (where $q=\sigma_1-\sigma_3$) as shown in Figure 2.2 or as circular surfaces on a stress ratio graph of $\mathbf{r}_{yy}$ versus $\mathbf{r}_{xy}$ as shown in Figure 2.3. As the model is sheared toward critical state ($\xi = 0$, $p/p_{cs} = 1$), the values of M^b and M^d will both approach the value of M. Thus, the bounding and dilatancy surfaces move together during shearing until they coincide with the critical state surface when the soil has reached critical state.

For soil at a fixed void ratio, the locus of points on the bounding surface in a q-p plot will be curved because changes in p will correspond to changes in state parameter and M^b. This is illustrated in Figure 2.4 showing q/p_{cs} versus p/p_{cs} for points on the bounding surface for soil at a fixed void ratio. For loose-of-critical states (i.e., $p/p_{cs} > 1$), the locus of q-p points on the bounding surface becomes flat for $n^{b,wet} = 1.0$ and becomes steeper with decreasing values of $n^{b,wet}$ until it follows M at the limit of $n^{b,wet} = 0.0$. For dense-of-critical states (i.e., $p/p_{cs} < 1$), the concave locus of q-p points on the bounding surface is stretched outward for larger values of $n^{b,dry}$ and pulls closer to M with decreasing values of $n^{b,dry}$. The functional forms for the bounding stress ratio, as illustrated in this figure, are later shown (Section 4.2) to be important for controlling undrained (i.e., constant void ratio) behaviors in monotonic and cyclic loading.

2.4 Yield surface and image back-stress ratio tensors

The yield surface and back-stress ratio tensor (α) follow those of the Dafalias and Manzari (2004) model, although their final form is considerably simplified by the prior assumption of removing any Lode angle dependency. The yield surface is a small cone in stress space, and is defined in stress terms by the following expression:

$$f = \left[(\boldsymbol{s} - p\boldsymbol{\alpha}) : (\boldsymbol{s} - p\boldsymbol{\alpha}) \right]^{1/2} - \sqrt{1/2}\, pm = 0 \tag{18}$$

The back-stress ratio tensor α defines the center of the yield surface, and the parameter m defines the radius of the cone in terms of stress ratio. The parameter m is assigned a default value of 0.01 based on results showing it provides reasonable modeling and numerical stability. The yield function can be rewritten to emphasize the role of stress ratio terms as follows,

$$f = \sqrt{(\boldsymbol{r} - \boldsymbol{\alpha}) : (\boldsymbol{r} - \boldsymbol{\alpha})} - \sqrt{1/2}\, m = 0 \tag{19}$$

The yield function can then be visualized as related to the distance between the stress ratio **r** and the back-stress ratio α, as illustrated in Figure 2.3.

The bounding surface formulation now requires that bounding and dilatancy stress ratio tensors be defined. Dafalias and Manzari (2004) showed that it is more convenient to track back-stress ratios and to similarly define bounding and dilatancy surfaces in terms of back-stress ratios. An image back-stress ratio tensor for the bounding surface (α^b) is defined as,

$$\boldsymbol{\alpha}^b = \sqrt{1/2} \left[M^b - m \right] \boldsymbol{n} \tag{20}$$

where the tensor **n** is normal to the yield surface. An image back-stress ratio tensor for the dilatancy surface (α^d) is similarly defined as,

$$\boldsymbol{\alpha}^d = \sqrt{1/2} \left[M^d - m \right] \boldsymbol{n} \tag{21}$$

The computation of constitutive responses can now be more conveniently expressed in terms of back-stress ratios rather than in terms of stress ratios, as noted by Dafalias and Manzari (2004).

2.5 Stress reversal and initial back-stress ratio tensors

The bounding surface formulation, as described in Dafalias (1986) and adopted by Dafalias and Manzari (2004), keeps track of the initial back-stress ratio (α_{in}) and uses it in the computation of the plastic modulus K_p. This tracking of one instance in loading history is essentially a first-order method for tracking loading history. A reversal in loading direction is then identified, following traditional bounding surface practice, whenever,

$$\left(\boldsymbol{\alpha}-\boldsymbol{a}_{in}\right):\boldsymbol{n}<0 \tag{22}$$

A reversal causes the current stress ratio to become the initial stress ratio for subsequent loading. Small cycles of load reversal can reset the initial stress ratio and cause the plastic modulus K_p to increase accordingly, in which case the stress-strain response becomes overly stiff after a small load reversal. This is a well-known problem in bounding surface formulations for which various approaches offer different advantages and disadvantages (e.g., Dafalias and Taiebat 2016, Duque et al. 2021).

The model presented herein tracks an initial back-stress ratio and a previous initial back-stress ratio ($\boldsymbol{\alpha}_{in}^{p}$), as illustrated in Figure 2.5a. When a reversal occurs, the previous initial back-stress ratio is updated to the initial back-stress ratio, and the initial back-stress ratio is updated to the current back-stress ratio.

In addition, the model tracks an apparent initial back-stress ratio tensor ($\boldsymbol{\alpha}_{in}^{app}$) as schematically illustrated in Figure 2.5b. The schematic in Figure 2.5b is similar to that of Figure 2.5a, except that the most recent loading reversals correspond to a small unload-reload cycle on an otherwise positive loading branch. The components of $\boldsymbol{\alpha}_{in}^{app}$ are taken as: (i) for positive loading directions, the minimum value they have ever had, but no smaller than zero, and (ii) for negative loading directions, the maximum value they have ever had, but no greater than zero. Figure 2.6 further illustrates these scenarios for four different loading cases. These minimum and maximum past back-stress ratios are stored for each component individually and for the entire loading history. The use of $\boldsymbol{\alpha}_{in}^{app}$ helps avoid the over-stiffening of the stress-strain response following small unload-reload cycles along an otherwise monotonically increasing branch of loading, without having to track the loading history through many cycles of load reversals.

The computation of K_p utilizes the values of $\boldsymbol{\alpha}_{in}^{app}$, $\boldsymbol{\alpha}_{in}^{true}$, and $\boldsymbol{\alpha}_{in}^{p}$, as defined in Figure 2.5b and Figure 2.6, to better approximate the stress-strain response during an unload-reload cycle. For the last positive loading branch in this figure, the value of K_p is initially most strongly controlled (inversely) by the distance $(\boldsymbol{\alpha} - \boldsymbol{\alpha}_{in}^{true}):\mathbf{n}$, such that the stiffness is initially large. As positive loading continues, the progressive reduction in K_p becomes increasingly dependent on $\boldsymbol{\alpha}_{in}^{app}$ as well. Once the positive loading exceeds the previous reversal point, the value of K_p becomes solely dependent on the distance $(\boldsymbol{\alpha} - \boldsymbol{\alpha}_{in}^{app}):\mathbf{n}$. Thus, the computation of K_p has the following dependencies:

$$\begin{aligned} &if\ \ (\boldsymbol{\alpha}-\boldsymbol{\alpha}_{in}^{p}):\boldsymbol{n}<0 \Rightarrow K_p = f\left(\boldsymbol{\alpha}_{in}^{true},\boldsymbol{\alpha}_{in}^{app}\right) \\ &else \qquad\qquad\qquad\ \ \Rightarrow K_p = f\left(\boldsymbol{\alpha}_{in}^{app}\right) \end{aligned} \tag{23}$$

The equations relating K_p to these back-stress ratios are given later in Section 2.7.

The impact of the above logic for defining $\boldsymbol{\alpha}_{in}$ on stress-strain responses is demonstrated in Figure 2.7 showing α_{xy} versus shear strain γ computed for two different drained DSS loading simulations. For these two examples, the reloading stiffness of the current loading branch (green line) is initially large because K_p is initially computed based on $\boldsymbol{\alpha}_{in} = \boldsymbol{\alpha}_{in}^{true}$. As the loading exceeds $\boldsymbol{\alpha}_{in}^{p}$, the loading stiffness becomes much softer because K_p is now computed based on $\boldsymbol{\alpha}_{in} = \boldsymbol{\alpha}_{in}^{app}$.

The initial back-stress ratio (α_{in}) is first established at initialization of the model or upon execution of FirstCall (see also Section 3). The value of α_{in} is established as being equal to the current back-stress ratio, subject to the limitation that its corresponding stress ratio be $\leq 0.9\ M^b$. This constraint on the magnitude of α_{in} at initialization avoids a problem that can otherwise occur when the initial consolidation stress state is above the bounding surface. In such cases, $K_p = 0$ since $M^{cur} > M^b$ and $D = 0$ since $\alpha - \alpha_{in} = 0$, which can result in no stress changes during shearing and hence an incorrect response. Linearly scaling α_{in} so its corresponding stress ratio is $\leq 0.9\ M^b$ upon initialization ensures that $D > 0$ at the start of shearing whenever the initial consolidation stress state corresponds to a stress ratio $> 0.9\ M^b$. Undrained shearing from such an initial consolidation stress state will thus be properly accompanied by contraction and associated strain softening.

2.6 Elastic strains and moduli

The elastic deviatoric strain and elastic volumetric strain increments are computed as,

$$d\boldsymbol{e}^{el} = \frac{d\boldsymbol{s}}{2G} \tag{24}$$

$$d\varepsilon_v^{el} = \frac{dp}{K} \tag{25}$$

where G is the elastic shear modulus and K is the elastic bulk modulus. The elastic shear modulus in the model presented herein is dependent on the mean effective stress according to,

$$G = G_o p_A \left(\frac{p}{p_A} \right)^{n_G} C_{SR} \tag{26}$$

where G_o and n_G are constants, p_A is the atmospheric pressure (101.3 kPa), and C_{SR} is a factor that accounts for stress ratio effects (described below).

Dafalias and Manzari (2004) had included dependence of G on void ratio following the form of Richart et al. (1970). This aspect was not included in the model herein because: (1) the effects of void ratio changes on G are small relative to those of confining stress, (2) the value of G is more strongly affected by environmental factors such as cementation and ageing, and (3) the calibration of G to in-situ shear wave velocity data is simplified by not including e.

The C_{SR} factor to account for stress ratio effects was included in the PM4Sand model and retained herein for the PM4Silt model. Yu and Richart (1984) showed that the small-strain elastic shear modulus of sand is dependent on the stress ratio and stress ratio history. The effect of stress ratio was shown to generally be less than about 10% when the ratio of major to minor principal effective stresses is less than about 2.5, but to also increase to about 20-30% at higher principal stress ratios. They also showed that stress ratio history caused a reduction in the small-strain elastic shear modulus when the maximum previous stress ratio was greater than the current stress ratio. The effect of stress ratio and stress ratio

history on the elastic shear modulus was approximately accounted for in the PM4Sand model by the factor C_{SR}. The equation for C_{SR} is similar in form to that used by Yu and Richart (1984) to represent stress ratio effects, except that it uses stress ratio terms consistent with the present model. The equation for C_{SR} was further normalized in PM4Silt Version 2.1 to produce a value of unity at the time of model initialization, and restricted to values less than unity thereafter, as,

$$C_{SR} = \frac{1 - C_{SR,o} \cdot \left(\frac{M}{M^b} \right)^{m_{SR}}}{\left[1 - C_{SR,o} \cdot \left(\frac{M}{M^b} \right)^{m_{SR}} \right]_{initial}} \leq 1.0 \tag{27}$$

The numerator in the above equation is the same form used in Version 1 of the model, while the denominator retains the value of the numerator from the time of model initialization. Thus, $C_{SR} = 1.0$ at the time of initialization. The above equation approximates Yu and Richart's (1984) results for stress ratio effects when $C_{SR,o} = 0.3$ and $m_{SR} = 2$. The effects of stress ratio history would cause further reductions, and is more complicated to represent. The calibration examples for PM4Sand worked well with $C_{SR,0} = 0.5$ and $m_{SR} = 4$, which result in the elastic modulus being 50% smaller when the stress ratio is on the bounding surface compared to when the soil is isotropically consolidated (i.e., when M = 0). The same default parameters are retained for PM4Silt, although the experimental basis for extending this relationship to low-plasticity silts and clays is lacking.

The elastic bulk modulus is related to the shear modulus through the Poisson's ratio as,

$$K = \frac{2(1+v)}{3(1-2v)} G \tag{28}$$

as was done by Dafalias and Manzari (2004).

2.7 Plastic components without fabric effects

Loading index

The loading index (L) is used to compute the plastic component of the volumetric strain increment and the plastic deviatoric strain increment tensor as,

$$d\varepsilon_v^{pl} = \langle L \rangle D \tag{29}$$

$$d\boldsymbol{e}^{pl} = \langle L \rangle \boldsymbol{R}' \tag{30}$$

where D is the dilatancy, **R** is the direction of $d\boldsymbol{\varepsilon}^{pl}$, **R′** is the deviatoric component of **R**, and <> are MacCauley brackets that set negative values to zero [i.e., <L> = L if L ≥ 0, and <L> = 0 if L < 0]. The tensor **R** for the assumption of no Lode angle dependency is,

$$\boldsymbol{R} = \boldsymbol{n} + \frac{1}{3} D\boldsymbol{I} \tag{31}$$

where **n** is the unit normal to the yield surface (Figure 2.3). Note that the assumption of no Lode angle dependency also means that **R′** = **n**. The dilatancy D relates the incremental plastic volumetric strain to the absolute value of the incremental plastic deviatoric strain,

$$D = \frac{d\varepsilon_v^{pl}}{\left| d\boldsymbol{e}^{pl} \right|} \tag{32}$$

The dilatancy D can be also related to the conventional engineering shear strain in this plane strain approximation, as

$$D = \frac{d\varepsilon_v^{pl}}{\sqrt{1/2}\left| d\gamma^{pl} \right|} \tag{33}$$

The loading index, as derived in Dafalias and Manzari (2004) is,

$$\begin{aligned} L &= \frac{1}{K_p} \frac{\partial f}{\partial \boldsymbol{\sigma}} : d\boldsymbol{\sigma} = \frac{1}{K_p} \left[\boldsymbol{n} : d\boldsymbol{s} - \boldsymbol{n} : \boldsymbol{r} dp \right] \\ L &= \frac{2G\boldsymbol{n} : d\boldsymbol{e} - \boldsymbol{n} : \boldsymbol{r} K d\varepsilon_v}{K_p + 2G - KD\boldsymbol{n} : \boldsymbol{r}} \end{aligned} \tag{34}$$

The stress increment for an imposed strain increment can then be computed as,

$$d\sigma = 2Gd\boldsymbol{e} + Kd\varepsilon_v \boldsymbol{I} - \left\langle L \right\rangle \left(2G\boldsymbol{n} + KD\boldsymbol{I} \right) \tag{35}$$

Hardening and the update of the back-stress ratio

Updating of the back-stress ratio is dependent on the hardening aspects of the model. Dafalias and Manzari (2004) updated the back-stress ratio according to bounding surface practice as,

$$d\boldsymbol{\alpha} = \langle L \rangle \left(\frac{2}{3} \right) h \left(\boldsymbol{\alpha}^b - \boldsymbol{\alpha} \right) \tag{36}$$

where h is the hardening coefficient. The factor of 2/3 was included for convenience so that model constants would be the same in triaxial and multi-axial derivations. They subsequently showed that the consistency condition $\delta f=0$ was satisfied when the plastic modulus K_p was related to the hardening coefficient as,

$$K_p = \frac{2}{3} p\, h \left(\boldsymbol{\alpha}^b - \boldsymbol{\alpha} \right) : \boldsymbol{n} \tag{37}$$

This expression can be rearranged so as to show that the consistency equation can be satisfied by expressing the hardening coefficient as,

$$h = \frac{3}{2} \frac{K_p}{p \left(\boldsymbol{\alpha}^b - \boldsymbol{\alpha} \right) : \boldsymbol{n}} \tag{38}$$

The relationship for the plastic modulus can subsequently take a range of forms, provided that the hardening coefficient and updating of the back-stress ratio follow the above expressions.

Plastic modulus

The plastic modulus in the multi-axial generalized form of Dafalias and Manzari (2004), after substituting in their expression for the hardening coefficient, can be expressed as,

$$K_p = \frac{2}{3} G\, h_o \left[\frac{1+e}{\left(2.97 - \mathrm{e} \right)^2} \left(1 - C_h e \right) \right] \frac{\left(\boldsymbol{\alpha}^b - \boldsymbol{\alpha} \right) : \boldsymbol{n}}{\left(\boldsymbol{\alpha} - \boldsymbol{\alpha}_{in} \right) : \boldsymbol{n}} \tag{39}$$

where h_o and C_h are scalar parameters and e is the void ratio. Setting aside the secondary influence of void ratio, this form illustrates that K_p is proportional to G, proportional to the distance of the back-stress ratio to the bounding back-stress ratio, and inversely proportional to the distance of the back-stress ratio from the initial back-stress ratio.

The plastic modulus relationship was revised in the model presented herein to provide an improved approximation of empirical relationships for secant shear modulus and equivalent damping ratios during drained strain-controlled cyclic loading. The plastic modulus is computed as,

$$K_p = G\, h_o \frac{\left[\left(\boldsymbol{\alpha}^b - \boldsymbol{\alpha} \right) : \boldsymbol{n} \right]^{0.5}}{\left[\exp\left[\left(\boldsymbol{\alpha} - \boldsymbol{\alpha}_{in}^{app} \right) : \boldsymbol{n} \right] - 1 \right] + C_{\gamma 1}} C_{rev} \tag{40}$$

$$C_{rev} = \frac{\left(\boldsymbol{\alpha} - \boldsymbol{\alpha}_{in}^{app}\right):\boldsymbol{n}}{\left(\boldsymbol{\alpha} - \boldsymbol{\alpha}_{in}^{true}\right):\boldsymbol{n}} \quad for \quad \left(\boldsymbol{\alpha} - \boldsymbol{\alpha}_{in}^{p}\right):\boldsymbol{n} \le \boldsymbol{0}$$
$$= 1 \quad otherwise \tag{41}$$

The factor C_{rev} accounts for the effect of unload-reload cycles as discussed in Section 2.5 and illustrated in Figures 2.5 and 2.6. The constant $C_{\gamma 1}$ in the denominator serves to avoid division by zero and has a slight effect on the nonlinearity and damping at small shear strains. If $C_{\gamma 1} = 0$, then the value of K_p will be infinite at the start of a loading cycle because $(\boldsymbol{\alpha} - \boldsymbol{\alpha}_{in}):\boldsymbol{n}$ will also be zero. In that case, nonlinearity will become noticeable only after $(\boldsymbol{\alpha} - \boldsymbol{\alpha}_{in}):\boldsymbol{n}$ becomes large enough to reduce K_p closer to the value of G (e.g., K_p/G closer to 100 or 200). Setting the value of $C_{\gamma 1} = h_o/200$ produces a reasonable response as will be demonstrated later with examples of modulus reduction and equivalent damping ratios. The stress ratio is precluded from being outside the greater of the bounding and dilatancy surfaces in the present implementation. The plastic modulus is further modified for the effects of fabric and fabric history, as described in a later section.

Plastic volumetric strains – Dilation

Plastic volumetric strains are related to plastic deviatoric strains through the dilatancy D (Equations 32 and 33), which is computed in the Dafalias and Manzari (2004) model and the base component of the model presented herein (with additional fabric effects described in a later section) as,

$$D = A_{do}\left[\left(\boldsymbol{\alpha}^{d} - \boldsymbol{\alpha}\right):\boldsymbol{n}\right] \tag{42}$$

Note that dilation (increasing void ratio) occurs whenever the term $(\boldsymbol{\alpha}^{\mathbf{d}} - \boldsymbol{\alpha}):\boldsymbol{n}$ is less than zero whereas contraction (decreasing void ratio) occurs when it is positive.

For sands, the constant A_{do} in this relationship can be related to the dilatancy relationship proposed by Bolton (1986), which follows from the work of Rowe (1962), through the following sequence of steps. Bolton showed that the difference between peak and constant volume friction angles in sands could be approximated as,

$$\phi_{pk} - \phi_{cv} = -0.8\psi \tag{43}$$

with

$$\psi = \tan^{-1}\left(\frac{d\varepsilon_v^{pl}}{\left|d\gamma^{pl}\right|}\right) \tag{44}$$

Since $\psi \approx \tan(\psi)$ for ψ less than about 0.35 radians (20 degrees), the difference between peak and constant volume friction angles (in radians) can be approximated as,

$$\phi_{pk} - \phi_{cv} = -0.8 \frac{d\varepsilon_v^{pl}}{\left| d\gamma^{pl} \right|} = -0.8 \sqrt{\frac{1}{2}} D \tag{45}$$

The peak friction angle is mobilized at the bounding surface, so this can be written as,

$$\phi_{pk} - \phi_{cv} = -0.8 \sqrt{\frac{1}{2}} A_{do} \left[\left(\boldsymbol{\alpha}^d - \boldsymbol{\alpha} \right) : \boldsymbol{n} \right]$$

$$\phi_{pk} - \phi_{cv} = -0.8 \sqrt{\frac{1}{2}} A_{do} \left[\left(\frac{M^d}{\sqrt{2}} \boldsymbol{n} - \frac{M^b}{\sqrt{2}} \boldsymbol{n} \right) : \boldsymbol{n} \right] \tag{46}$$

The term **n**:**n** is equal to unity, and the values of ϕ_{pk} and ϕ_{cv} (again in radians) can be replaced with expressions in terms of M^b and M as,

$$\sin^{-1}\left(\frac{M^b}{2} \right) - \sin^{-1}\left(\frac{M}{2} \right) = 0.4 A_{do} \left[M^b - M^d \right] \tag{47}$$

This expression can then be rearranged to solve for A_{do} as,

$$A_{do} = \frac{1}{0.4} \frac{\sin^{-1}\left(\frac{M^b}{2} \right) - \sin^{-1}\left(\frac{M}{2} \right)}{M^b - M^d} \tag{48}$$

where the angles returned by the $\sin^{-1}$ functions are in radians.

The parameter A_{do} should thus be chosen to be consistent with the relationships that control M^b and M^d. For sands, the value for A_{do} ranged from 1.26 to 1.45 for a range of relative states and the functions used in the PM4Sand model (Boulanger and Ziotopoulou 2020). If these stress-dilatancy relationships are considered applicable for low plasticity silts and clays, then the above expression produces A_{do} values ranging from 0.8 to 1.2 for the M^b and M^d functions described herein with a wide range of values for $n^{b,dry}$, n^d, ξ, and λ. A default value for A_{do} of 0.8 is adopted in the PM4Silt model based on the other default parameters summarized in a later section, although an alternative value for A_{do} can be specified by the user.

Plastic volumetric strains – Contraction

Plastic volumetric strains during contraction (i.e., whenever ($\boldsymbol{\alpha}^{\mathbf{d}}$ - $\boldsymbol{\alpha}$):**n** is greater than zero) are computed in the Dafalias and Manzari (2004) model using the same expression as used for dilatancy,

$$D = A_{do}\left[\left(\boldsymbol{\alpha}^{d} - \boldsymbol{\alpha}\right) : \boldsymbol{n}\right] \tag{49}$$

The use of this expression was found to limit the ability of the model to approximate a number of important loading responses; e.g., it overestimated the slope of the cyclic resistance ratio (CRR) versus number of equivalent uniform loading cycles for undrained cyclic element tests (e.g., Ziotopoulou and Boulanger 2012).

Plastic volumetric strains during contraction for the model presented herein are computed using the following expression,

$$D = A_{dc}\left[\left(\boldsymbol{\alpha} - \boldsymbol{\alpha}_{in}^{app}\right) : \boldsymbol{n} + C_{in}\right]^{2} \frac{\left(\boldsymbol{\alpha}^{d} - \boldsymbol{\alpha}\right) : \boldsymbol{n}}{\left(\boldsymbol{\alpha}^{d} - \boldsymbol{\alpha}\right) : \boldsymbol{n} + C_{D}} \tag{50}$$

$$A_{dc} = \frac{A_{do}}{h_{p}} \tag{51}$$

The various forms in the above relationships were initially developed to improve different aspects of the calibrated model's performance for sands. The value of D was set proportional to the square of $((\boldsymbol{\alpha} - \boldsymbol{\alpha}^{in}):\mathbf{n} + C_{in})$ to improve the slope of the relationship between CRR and number of uniform loading cycles. The C_{in} term depends on fabric and is described in a later section along with other modifications to the above expression for the effects of fabric and fabric history. The inclusion of the term C_{in} improves the stress paths for undrained cyclic loading and the volumetric strain response during drained cyclic loading of sand. Inclusion of this constant enables some volumetric strain to develop early in the unloading from a point outside the dilatancy surface (as described later). The remaining terms on the right-hand side of the equation were chosen to be close to unity over most of the loading range, while ensuring that D smoothly goes to zero as $\boldsymbol{\alpha}$ approaches $\boldsymbol{\alpha}^{d}$; reasonable results were obtained using a C_D value of 0.10.

The parameter A_{dc} for contraction was related to the value of A_{do} for dilation by dividing it by a parameter h_p that can be varied during the calibration process to obtain desired cyclic resistance ratios. The effect of varying states on cyclic loading behavior was then conveniently incorporated by making h_p depend on ξ/λ as follows.

$$h_{p} = h_{po}\exp\left(-0.7 + 0.2\left\langle 3 - \frac{\xi}{\lambda}\right\rangle^{2}\right) \tag{52}$$

Thus, the scalar constant h_{po} provides a linear scaling of contraction rates while the functional form of the remaining portion of this expression provides for stronger variations with state (which helps with calibration of the h_{po} values). The variation of h_p with ξ/λ for different values of h_{po} is plotted in Figure 2.8. Once the other input parameters have been selected, the constant h_{po} can be calibrated to arrive at a desired cyclic resistance ratio.

An upper limit was imposed on the contraction rate, with the limiting value computed as,

$$D \le A_{do} \frac{\left(\boldsymbol{\alpha}^d - \boldsymbol{\alpha}\right):\boldsymbol{n}}{\left(\boldsymbol{\alpha}^d - \boldsymbol{\alpha}\right):\boldsymbol{n} + C_D} \tag{53}$$

A similar limit was used in PM4Sand to prevent numerical issues that can be encountered with excessively large contraction rates with some combinations of input parameters. For most calibrations of PM4Silt, this limit does not appear to control contraction rates.

2.8 Fabric effects

Dafalias and Manzari (2004) introduced a fabric-dilatancy tensor (**z**) that could be used to account for the effects of prior straining in sand. Their fabric tensor (**z**) evolved in response to plastic volumetric dilation strains, according to,

$$d\boldsymbol{z} = -c_z \left\langle -d\varepsilon_v^{pl} \right\rangle \left(z_{max}\boldsymbol{n} + \boldsymbol{z}\right) \tag{54}$$

where the parameter c_z controls the rate of evolution and z_{max} is the maximum value that **z** can attain.

The fabric-dilatancy tensor was modified for the present model as,

$$d\boldsymbol{z} = -\frac{c_z}{1 + \left\langle \frac{z_{cum}}{2z_{max}} - 1 \right\rangle} \frac{\left\langle -d\varepsilon_v^{pl} \right\rangle}{D} \left(z_{max}\boldsymbol{n} + \boldsymbol{z}\right) \tag{55}$$

In this expression, the tensor **z** evolves in response to plastic deviatoric strains that occur during dilation only (i.e., dividing the plastic volumetric strain by the dilatancy gives plastic shear strain). In addition, the evolution of fabric is restricted to only occur when $(\boldsymbol{\alpha}^{\mathbf{d}} - \boldsymbol{\alpha}):\mathbf{n} < 0$; this additional constraint precludes fabric evolution during dilation above the rotated dilatancy surface (introduced later) but below the non-rotated dilatancy surface. The parameter z_{cum} is the cumulative value of absolute changes in **z** computed according to,

$$dz_{cum} = \left|d\boldsymbol{z}\right| \tag{56}$$

The rate of evolution for **z** therefore decreases with increasing values of z_{cum}, which enables the undrained cyclic stress-strain response to progressively accumulate shear strains rather than lock-up into a repeating stress-strain loop. In addition, the greatest past peak value (scalar amplitude) for **z** during its loading history is also tracked,

$$z_{peak} = \max\left(\sqrt{\frac{\mathbf{z}:\mathbf{z}}{2}}, z_{peak}\right) \tag{57}$$

The values of **z**, z_{peak}, and z_{cum} are later used to facilitate the accumulation of shear strains under symmetric loading through their effects on the plastic modulus and dilatancy relationships.

The evolution of the fabric tensor terms is illustrated in Figures 2.9, 2.10 and 2.11 showing the response of three different specimens to undrained cyclic DSS loading. The results for $s_{u,cs}/\sigma'_{vc} = 0.25$ without any sustained horizontal shear stress (Figure 2.9) show the fabric terms do not grow until the soil reaches the dilatancy surface, which only occurs when the effective stress has reduced enough that the soil becomes dense of critical. Note that the cyclic loading on this specimen is low enough that the specimen never reaches the bounding surface while it is loose-of-critical and it also never reaches critical state. The fabric oscillates between positive and negative values as the specimen reaches the dilatancy surface in opposing directions during this symmetric cyclic loading. The results for $s_{u,cs}/\sigma'_{vc} = 0.25$ with a sustained horizontal shear stress ratio of 0.10 (Figure 2.10) show the specimen rapidly developing large shear strains without ever growing any fabric; this occurs because the soil reaches the bounding surface while still loose-of-critical, after which it moves toward critical state without ever reaching a dilatancy surface. The results for $s_{u,cs}/\sigma'_{vc} = 0.50$ with a sustained horizontal shear stress ratio of 0.20 (Figure 2.11) show fabric only developing in one direction because the specimen only reaches the dilatancy surface on one side (i.e., per the stress path); this specimen also never reaches critical state.

Additional memory of fabric formation history

Memory of the fabric formation history was included in the model presented herein to improve the ability of the model to account for the effects of sustained static shear stresses and account for differences in fabric effects for various drained versus undrained loading conditions.

The initial fabric tensor ($\mathbf{z}_{in}$) at the start of the current loading path is determined whenever a stress ratio reversal occurs. The $\mathbf{z}_{in}$ tracks the immediate history terms without any consideration of whether an earlier loading cycle had produced greater degrees of fabric (i.e., the logic is different from that adopted for the updating of back-stress ratio history terms). This history term is used for describing the degree of stress rotation and its effects on plastic modulus, as described later.

Another aspect of the fabric history that is tracked is the mean stress at which the fabric is formed. This aspect of fabric history is tracked by tracking the product of **z** and p, and defining p_{zp} as the mean stress at the time that this product achieves its greatest peak value. The p_{zp} is used in addressing a couple of issues, including the issue of how fabric that is formed during cyclic loading may be erased during reconsolidation. For example, a saturated soil that develops cyclic mobility behavior during undrained cyclic loading clearly remembers its history of plastic deviatoric strains and then subsequently forgets (to a large extent) this prior strain history when it reconsolidates back to its pre-earthquake confining stress. As another example, the memory of prior strains during undrained cyclic loading is very different than the memory of prior strains during drained cyclic loading. This memory conceptually could be related to the history of plastic and total volumetric strains, but a simpler method to account for this effect is to consider how the mean stress p relates to the value of p_{zp}. Conceptually, it appears that prior

strain history (or fabric) is most strongly remembered when the soil is operating under mean stresses that are smaller than those that existed when the fabric was formed (i.e., $p << p_{zp}$) and then largely forgotten when they are of the same order (i.e., $p \approx p_{zp}$). This attribute will be used in the relationships described later for describing the effects of fabric on dilatancy.

Effect of fabric on plastic modulus

An effect of fabric on the plastic modulus was added to the model presented herein by reducing the plastic modulus as the fabric tensor increased in peak amplitude, as follows,

$$K_p = G\, h_o \frac{\left[\left(\boldsymbol{\alpha}^b - \boldsymbol{\alpha}\right):\boldsymbol{n}\right]^{0.5}}{\left[\exp\left(\left(\boldsymbol{\alpha} - \boldsymbol{\alpha}_{in}^{app}\right):\boldsymbol{n}\right) - 1\right] + C_{\gamma 1}} C_{rev} \cdot \frac{C_{k\alpha}}{1 + C_{K_p}\left(\frac{z_{peak}}{z_{max}}\right)\left\langle\left(\boldsymbol{\alpha}^b - \boldsymbol{\alpha}\right):\boldsymbol{n}\right\rangle\sqrt{1 - C_{zpk2}}} \tag{58}$$

where,

$$C_{K\alpha} = 1 + \frac{C_{K\alpha f}}{1 + \left(2.5\left\langle\left(\boldsymbol{\alpha} - \boldsymbol{\alpha}_{in}^{true}\right):\boldsymbol{n}\right\rangle\right)^2} C_{pzp2}\, C_{zpk1} \tag{59}$$

$$C_{zpk1} = \frac{z_{peak}}{z_{cum} + \frac{z_{max}}{5}} \tag{60}$$

$$C_{zpk2} = \frac{z_{peak}}{z_{cum} + \frac{z_{max}}{100}} \tag{61}$$

$$C_{pzp2} = \frac{-\left\langle-\left(p_{zp} - p\right)\right\rangle}{-\left\langle-\left(p_{zp} - p\right)\right\rangle + p_{\min}} \tag{62}$$

The above expressions produce a reduction in plastic modulus when fabric is favorable ($\mathbf{z}:\mathbf{n} \geq 0$) and with increasing plastic shear strains (which conceptually would break down any cementation). This reduces both the plastic modulus and the hysteretic damping at larger shear strains (note that $z_{peak} = 0$ unless the soil has been loaded strongly enough to pass outside the dilatancy surface), improves the volumetric strains that develop in drained cyclic loading, and improves the path in undrained cyclic loading.

The $C_{K\alpha}$ and $\sqrt{1-C_{zpk2}}$ terms both serve to increase K_p during non-reversal loading by amounts that depend on the fabric and stress history. During reversal loading, the $\sqrt{1-C_{zpk2}}$ term approaches unity and K_p evolves as it previously had. The roles of each of the other terms are discussed below.

C_{zpk1} and C_{zpk2} are terms that start from zero and grow to be unity for uni-directional growth of fabric which is the case during non-reversing loading conditions. These two terms differ by the rate under which they approach unity by the use of the constant z_{max} /5 or z_{max} /100 with these respective values chosen for their ability to better approximate the engineering behaviors of interest. For full reversal loading where the fabric alternates between positive and negative values, these terms will both go to zero.

C_{pzp2} starts initially at zero and stays equal to zero until fabric is formed. After fabric is formed, this term quickly transitions to unity for values of mean effective stress p that are less than the value that p had when the maximum fabric was formed (p_{zp}). If p increases beyond the value of p_{zp} the term will return to zero according to the Macaulay brackets.

The values for the calibration parameters C_{Kp} and $C_{K\alpha f}$ were chosen for their ability to reasonably approximate the targeted behaviors, as discussed later. Setting C_{Kp} to a default value of 2.0 was found to produce reasonable responses for sand with particular emphasis on improving (reducing) the equivalent damping ratios at shear strains of 1 to 3% in drained cyclic loading; the same default value for C_{Kp} was retained for PM4Silt. The parameter $C_{K\alpha f}$ was useful for adjusting the undrained cyclic loading response with sustained static shear stresses for sands. For PM4Silt, the $C_{K\alpha f}$ term has little effect on cyclic strengths for soils that are loose-of-critical, but does become more influential for dense-of-critical soils. For the present implementation of PM4Silt, a default value of 4.0 was adopted regardless of initial state.

The cumulative effect of the above parameters can be understood as follows. If a soil is strongly loaded in uni-directional loading and forms significant amount of fabric and is then unloaded, then upon subsequent reloading the terms C_{pzp2} and C_{zpk1} will be unity and $C_{K\alpha}$ will become large. If the loads are increased to where the soil is being sheared and forming fabric at even higher stresses (higher values of p than fabric was previously formed at) then $C_{K\alpha}$ will be unity (C_{pzp2} = 0). In this way, an element that has developed strong fabric under monotonic or cyclic loading without reversal of the total shear stress direction (e.g., an element within a steep slope where the static shear stresses are greater than the cyclic shear stresses) will, when unloaded and reloaded, be initially much stiffer (increased K_p) followed by a softening (smaller K_p) if the soil is loaded into virgin territory.

Effect of fabric on plastic volumetric dilation

A rotated dilatancy surface with slope M^{dR} which evolves with the history of the fabric tensor **z** was added to the framework of the model to facilitate earlier dilation at low stress ratios under certain loading paths for sands (Ziotopoulou and Boulanger 2016). The rotated surface, schematically illustrated in Figure 2.12 as a line in q-p space and Figure 2.13 as a circular surface on a stress ratio graph of r_{yy} versus r_{xy}, is equal to the original dilatancy surface scaled-down by a factor C_{rot1}:

$$M^{dR} = \frac{M^d}{C_{rot1}} \tag{63}$$

$$C_{rot1} = 1 + \frac{2 \cdot \langle -\boldsymbol{z} : \boldsymbol{n} \rangle}{\sqrt{2} z_{max}} \left(1 - C_{zin1}\right) \geq 1 \tag{64}$$

where M^d is the slope of the unrotated dilatancy surface. Experimental results (Ziotopoulou 2014, Ziotopoulou and Boulanger 2016) indicate that the loading history, the loading direction and the loading pattern play important roles in the response of sand to irregular cyclic loading. Thus the scaling factor that defines the rotated dilatancy surface was made dependent on whether fabric is favorable ($\mathbf{z} : \mathbf{n} > 0$) or unfavorable ($\mathbf{z} : \mathbf{n} < 0$) and on the factor C_{zin1} which is an indirect measure of whether there are reversals or not,

$$C_{zin1} = \left\langle 1 - \exp\left(-2.0 \left| \frac{\boldsymbol{z}_{in} : \boldsymbol{n} - \boldsymbol{z} : \boldsymbol{n}}{z_{max}} \right| \right) \right\rangle \tag{65}$$

where $\mathbf{z_{in}}$ is the fabric tensor at the beginning of the current loading branch. C_{zin1} can take values ranging from 0, when there are no reversals, to 1, when there are reversals. The rotated dilatancy surface is operating only for loading with an unfavorable fabric since the factor C_{rot1} becomes 1 when the fabric is favorable (i.e., $\langle -\mathbf{z} : \mathbf{n} \rangle = 0$). In the present model, rotation of the dilatancy surface was also restricted to the case where the soil is dense-of-critical (i.e., $C_{rot1} = 1$ for $\xi > 0$).

A back-stress ratio tensor for the rotated dilatancy surface (α^{dR}) was introduced as,

$$\alpha^{dR} = \frac{1}{\sqrt{2}} \left(M^{dR} - m \right) \boldsymbol{n} \tag{66}$$

Dilation occurs whenever the term $(\boldsymbol{\alpha}^{dR} - \boldsymbol{\alpha}) : \mathbf{n}$ is negative whereas contraction occurs when it is positive. The calculation of D is still treated separately during dilation and contraction.

D during dilation is now computed according to the following expressions. First, a value for D is computed from the rotated dilatancy surface,

$$D_{rot} = A_d \frac{\langle -\boldsymbol{z} : \boldsymbol{n} \rangle}{\sqrt{2} z_{max}} \frac{(\alpha^{dR} - \alpha) : \boldsymbol{n}}{C_{DR}} \tag{67}$$

where the C_{DR} factor is applied to reduce the rate under which dilatancy is increasing and is discussed further below. Second, another value for D is computed that would be obtained from the non-rotated dilatancy surface,

$$D_{non-rot} = A_d \left(- \left\langle -(\alpha^d - \alpha) : \boldsymbol{n} \right\rangle \right) \tag{68}$$

The Macaulay brackets in the above expression ensure that $D_{non\text{-}rot}$ is equal to zero whenever $(\boldsymbol{\alpha}^d - \boldsymbol{\alpha}) : \mathbf{n} > 0$ while $(\boldsymbol{\alpha}^{dR} - \boldsymbol{\alpha}) : \mathbf{n} < 0$. Lastly, the operating value of D is selected from the above two values based on:

$$if \;\; D_{non-rot} < D_{rot} \;\; \Rightarrow \;\; D = D_{non-rot}$$
$$else \;\; D = D_{non-rot} + \left(D_{rot} - D_{non-rot}\right) \frac{\left\langle M^b - M^{cur} \right\rangle}{\left\langle M^b - M^{cur} + 0.01 \right\rangle} \tag{69}$$

The above logic is illustrated in Figure 2.14 where D is plotted for a half-cycle of loading that goes from contraction to dilation. This figure shows that $D_{non\text{-}rot}$ is used whenever it is smaller (more negative) than D_{rot}. For cases where D_{rot} is smaller than $D_{non\text{-}rot}$, the value of D is interpolated based on the additional term on the right that multiplies the difference between D_{rot} and $D_{non\text{-}rot}$. This interpolation term is close to unity for stress ratios away from the bounding surface ($M^{cur} < M^b$), such that D will be equal to D_{rot} as illustrated in the figure. However, this term will also go smoothly to zero as the stress ratio gets close to the bounding surface, so that dilatancy smoothly goes to zero as a soil approaches the critical state where $M = M^d = M^b$. The constant of 0.01 in the denominator controls the rate under which D goes to zero as the stress ratio nears the bounding surface and was found to provide reasonable results in trial simulations.

The factor C_{DR} in the denominator of the expression for D_{rot} is applied so that the D computed based on the rotated dilatancy surface is consistent with experimental observations. A value of 3.0 was used for the default calibration described later and found to provide reasonable results in trial simulations.

Lastly, the parameter A_d in the expressions for both D_{rot} and $D_{non\text{-}rot}$ is expressed as,

$$A_d = \frac{A_{do}\left(C_{zin2}\right)}{\left(\frac{z_{cum}^2}{z_{max}}\right)\left(1 - \frac{\left\langle -\boldsymbol{z} : \boldsymbol{n} \right\rangle}{\sqrt{2} \cdot z_{peak}}\right)^3 \left(C_\varepsilon\right)^2 \left(C_{pzp}\right)\left(C_{zin1}\right) + 1} \tag{70}$$

$$C_{pzp} = \frac{1}{1 + \left(2.5 p \,/\, p_{zp}\right)^5} \tag{71}$$

$$C_{zin1} = 1.0 - \exp\left(-2.0 \left| \frac{\boldsymbol{z}_{in} : \boldsymbol{n} - \boldsymbol{z} : \boldsymbol{n}}{z_{max}} \right| \right) \tag{72}$$

$$C_{zin2} = \frac{1 + C_{zin1} \dfrac{z_{cum} - z_{peak}}{3 z_{max}}}{1 + 3 C_{zin1} \dfrac{z_{cum} - z_{peak}}{3 z_{max}}} \tag{73}$$

Consider the five terms added to the denominator of the expression for A_d. The first term $[z_{cum}^2/z_{max}]$ facilitates the progressive growth of strains under symmetric loading by reducing the dilatancy that occurs when a liquefied soil has been sheared through many cycles of loading; note that this term progressively increases with subsequent cycles of loading. The second term facilitates strain-hardening

when the plastic shear strain reaches the prior peak value, wherein the term approaches zero (i.e., when $\mathbf{z}:\mathbf{n}$ approaches $z_{peak}\sqrt{2}$) and the dilation rate consequently rapidly approaches the virgin loading value of A_{do}. The third term C_ε is a calibration constant that can be used to modify the rate of plastic shear strain accumulation. The fourth term C_{pzp} causes the effects of fabric on dilation to be diminished (erased) whenever the current value of p is near the value of p_{zp}; this term enables the model to provide reasonable predictions of responses to large numbers of either drained or undrained loading cycles. The fifth term C_{zin1} facilitates strain-hardening when stress reversals are not causing fabric changes; i.e., when the initial and current fabric terms are close to equal, the term C_{zin1} goes to zero. Lastly, the second term in the numerator, C_{zin2}, causes the dilatancy to be decreased by up to a factor of 3 under conditions of large strains and full stress (and fabric) reversals, which improves the prediction of cyclic strain accumulation during undrained cyclic loading.

An additional constraint is placed on D during dilation at very low effective stresses. For $p < 2p_{min}$, the value of D cannot be smaller in magnitude than computed by the following expression,

$$D = -3.5 A_{do} \left\langle M^b - M^d \right\rangle \frac{2p_{\min} - p}{p_{\min}} \quad for \quad p_{\min} \le p \le 2p_{\min} \tag{74}$$

This expression ensures that the model will, for dense-of-critical soils (i.e., $M^b > M^d$), be dilative when p falls below $2p_{min}$.

The parameter p_{min} is set one of two ways. If the input parameter $r_{up,max}$ is specified, then p_{min} is computed from the value of p at the time of "consolidation" (i.e., the p value when the flag FirstCall – see Section 3 – was last set equal to 0) as,

$$p_{\min} = \left(1 - r_{up,\max}\right)\frac{p}{2} \tag{75}$$

The parameter $r_{up,max}$ is limited to a maximum value of 0.99 and a minimum value of zero. For example, setting $r_{up,max}$ equal to 0.95 results in p_{min} being 2.5% of the value of p at consolidation. If $r_{up,max}$ is not specified, p_{min} is set equal to $p_{cs}/8$, where p_{cs} is the value of p at critical state for the specified s_u. This default relation can be expressed as,

$$p_{\min} = \frac{p_{cs}}{8} = \frac{2s_u}{8M} \tag{76}$$

The p_{min} value obtained using this latter expression is limited to be no greater than the p_{min} computed using $r_{up,max} = 0$. For either case, p_{min} is further limited to be no smaller than 0.5 kPa.

Effect of fabric on plastic volumetric contraction

Dafalias and Manzari (2004) used the fabric tensor to modify the dilatancy during contraction ($D > 0$) as follows,

$$D = A_d \left[\left(\boldsymbol{\alpha}^d - \boldsymbol{\alpha} \right) : \boldsymbol{n} \right] \left(1 + \left\langle \boldsymbol{z} : \boldsymbol{n} \right\rangle \right) \tag{77}$$

This relationship enhances the volumetric contraction whenever the fabric is favorable (**z**:**n** ≥ 0), based on the term 1+<**z**:**n**> as recommended by Dafalias and Manzari (2004).

The effect of fabric on dilatancy during contraction was modified for the present model as,

$$D = A_{dc}\left[\left(\boldsymbol{\alpha}-\boldsymbol{\alpha}_{in}^{app}\right):\boldsymbol{n}+C_{in}\right]^2\frac{\left(\boldsymbol{\alpha}^d-\boldsymbol{\alpha}\right):\boldsymbol{n}}{\left(\boldsymbol{\alpha}^d-\boldsymbol{\alpha}\right):\boldsymbol{n}+C_D}C_{p\min} \tag{78}$$

$$A_{dc} = \frac{A_{do}\left(1+\langle \boldsymbol{z}:\boldsymbol{n}\rangle\right)}{h_p C_{dz} C_{wet}} \tag{79}$$

$$C_D = 0.1 \tag{80}$$

$$C_{in} = \frac{2\cdot\langle \boldsymbol{z}:\boldsymbol{n}\rangle}{\sqrt{2}z_{\max}} \tag{81}$$

$$C_{dz} = \left(1-C_{rot2}\cdot\frac{\sqrt{2}z_{peak}}{z_{\max}}\right)\left(\frac{z_{\max}}{z_{\max}+C_{rot2}\cdot z_{cum}}\right) \tag{82}$$

$$C_{rot2} = 1-\frac{z_{peak}}{z_{cum}+\frac{z_{max}}{100}}\left(=1-C_{zpk2}\right) \tag{83}$$

$$C_{wet} = \frac{1}{\frac{1}{1+\left(\frac{C_{w1}}{\left(\alpha^b-\alpha\right):\mathrm{n}}\right)^4}+\frac{1}{1+\left(\frac{\xi/\lambda}{C_{w2}}\right)^2}} \le 1 \tag{84}$$

$$C_{w1} = 0.02 \tag{85}$$

$$C_{w2} = 0.1 \tag{86}$$

$$\begin{aligned} C_{p\min} &= 0 \quad for \quad p < 2p_{\min} \\ &= 1 \quad for \quad p > 8p_{\min} \\ &= \frac{p-2p_{\min}}{6p_{\min}} \quad otherwise \end{aligned} \tag{87}$$

The factor C_{in} in the expression for D has been modified so it now depends on fabric; C_{in} is zero for unfavorable fabric, and increases with increasing **z**:**n** for favorable fabric to enhance the contraction rate at the start of an unloading cycle (note that D would be zero at the start of an unloading cycle if C_{in} was zero).

The term C_{dz} in the denominator of the expression for A_{dc} serves to increase the rate of contraction as z_{peak} nears z_{max} or as a large amount of cumulative fabric formation/destruction has taken place. This

term was developed for improved modeling of the cyclic strength of denser sands, for which the value of h_p can be on the order of 100 (Boulanger and Ziotopoulou 2020). The degrading of the denominator as z_{peak} or z_{cum} increases enables the generation of high excess pore pressures at higher loading levels on stronger soils, and influences the slope of the CRR versus number of uniform loading cycles relationship obtained for undrained element loading. Note that the denominator degrades whether fabric is favorable or not, but that the overall rate of contraction is more enhanced if the fabric is favorable ($\mathbf{z}$:$\mathbf{n} \geq 0$). The factor C_{rot2} was introduced into the factor C_{dz} to provide better control over the rate of contraction as z_{peak} nears z_{max} or as a large amount of cumulative fabric formation/destruction has taken place. The factor C_{rot2} takes values that range from 1 for loading with zero fabric or cyclic loading that causes reversals of fabric (since z_{cum} will become much larger than z_{peak}), to 0 for loading that causes fabric to grow monotonically in one direction such as in non-reversal cyclic loading (since z_{cum} will equal z_{peak}).

The term C_{wet} in the denominator of the expression for A_{dc} serves to increase the rate of contraction when the stress state reaches the bounding surface for loose-of-critical state conditions. This term approaches zero for soils that are loose of critical and on the bounding surface, but increases to unity for soils that are sufficiently close to critical state (controlled by the constant C_{w1}) or sufficiently away from the bounding surface (controlled by the constant C_{w2}). The constants C_{w1} and C_{w2} were set to 0.02 and 0.1 because they produced reasonable responses for a range of calibrations.

The last parameter C_{pmin} varies linearly with p between values of $C_{pmin} = 0.0$ for $p \leq 2p_{min}$ and $C_{pmin} = 1.0$ for $p \geq 8p_{min}$. This parameter provides the mechanism for limiting the maximum excess pore water pressure ratio (or minimum effective stress) that develops during cyclic loading. When p reaches $2p_{min}$, the contraction rate goes to zero such that further reductions in p will not occur during undrained loading.

Effect of fabric on the elastic modulus

The elastic shear modulus and elastic bulk modulus may degrade with increasing values of cumulative plastic deviator strain term, z_{cum}. This component of the model was added to account for the progressive destruction, with increasing plastic shear strains, of any minor cementation bonds or other ageing- or strain history-related phenomena that produced an increase in small-strain shear modulus. The destruction of minor cementation by plastic shear strains is evidenced in the field by measurements of shear wave velocities in sand that are lower after earthquake shaking than before earthquake shaking (e.g., Arai 2006). The degradation of the elastic shear modulus is computed as,

$$G = G_o p_A \left(\frac{p}{p_A} \right)^{n_G} C_{SR} \left(\frac{1 + \frac{z_{cum}}{z_{max}}}{1 + \frac{z_{cum}}{z_{max}} C_{GD}} \right) \tag{88}$$

where C_{GD} is the factor by which the shear modulus is degraded (divided) at very large values of z_{cum}. This change in the elastic shear modulus G causes the bulk modulus K to progressively decrease with increasing z_{cum}. The change in K improves the model's ability to track the stress-strain response of liquefying soils. In particular, decreasing K with increasing z_{cum} reduces the rate of strain-hardening

after phase transformation at larger shear strain levels, and improves the ability to approximate the hysteretic stress-strain response of a soil as it liquefies or cyclically softens.

2.9 Post-shaking undrained shear strength

The value of s_u that should be used for evaluating static stability after strong shaking is often smaller than used for evaluating dynamic responses for two primary reasons. First, the s_u of low plasticity silts and clays generally exhibit strain rate dependence, such that the value for post-shaking stability should correspond to the slower strain rate associated with static stability (i.e., $s_{u,static}$). Secondly, the s_u can be reduced by cyclic degradation or remolding that occurs during strong shaking.

The ability to reduce s_u at a specific time during an analysis (e.g., after the end of strong shaking) was incorporated into PM4Silt as a pragmatic means for evaluating post-shaking static stability. After strong shaking has ended, the input parameter F_{su} can be used to shift the critical state line leftward relative to its initial position by a factor of F_{su}, thereby reducing the undrained shear strength at critical state ($s_{u,cs}$) by the same factor for the post-strong-shaking portion of the analysis. This shift in the critical state line can be expressed in the calculation of the state parameter as follows.

$$\xi = e - \left[e_{1kPa} - \lambda \ln\left(\frac{p}{F_{su}\ 1kPa} \right) \right] \tag{89}$$

The default value for F_{su} is 1.0 (no shift in the critical state line), and the code does not require that a value for F_{su} be specified during the analysis. The use of F_{su} is discussed further in Section 4.

2.10 Post-shaking reconsolidation

Volumetric strains that develop during reconsolidation of liquefied sands or cyclically-softened silts and clays are difficult to numerically model using the conventional constitutive separation of strains into elastic and plastic components, plus the present model is not formulated to model yielding along reconsolidation paths (e.g., constant K_o loading). The PM4Silt model retains the form of the PM4Sand model for better estimating reconsolidation strains during the post-shaking portion of a numerical simulation. The modification involved the pragmatic approach of reducing the post-shaking elastic shear modulus G (and hence elastic bulk modulus K) which increases reconsolidation strains, thereby compensating for limitations in the model formulation. The user may activate this feature after the end of strong shaking, such that post-liquefaction reconsolidation strains are better approximated in the remainder of the simulation. This feature should not be activated for the strong shaking portion of a simulation.

The post-shaking elastic moduli are determined by multiplying the conventional elastic moduli (computed using the expressions described earlier) by a reduction factor F_{consol} as,

$$G_{post-shaking} = F_{consol} G \tag{90}$$

$$K_{post-shaking} = F_{consol} K \tag{91}$$

The F_{consol} value is computed as,

$$G_{c,\min} = \left(\frac{8p}{\lambda}\right)\left(\frac{1}{1+\left(C_{GC}-1\right)\left(\frac{z_{cum}}{z_{cum}+z_{\max}}\right)}\right) \tag{92}$$

$$F_{consol} = 1-\left(1-\frac{G_{c,\min}}{G}\right)\left\langle 1-\frac{M^{cur}}{M^{d}}\right\rangle^{0.25} \tag{93}$$

where the parameter C_{GC} determines how much the elastic moduli will be degraded by if z_{cum} becomes large. If z_{cum} is small, the value of $G_{c,min}$ corresponds to an elastic modulus consistent with the one dimensional recompression stiffness estimated based on p and λ. Lastly, the expression for F_{consol} will return values close to $G_{c,min}$ if the loading is well within the dilatancy surface ($M^{cur} << M^{d}$) and close to G if the loading is near the dilatancy surface ($M^{cur} \approx M^{d}$).

2.11 Summary of constitutive equations

The constitutive equations for the model presented herein are summarized in Table 2.1.

Table 2.1. Comparison of constitutive equations

PM4Silt model
Critical state line $\xi = e - e_{1kPa} + \lambda \ln\left(\frac{p}{F_{su} \cdot 1kPa}\right)$ $F_{su} = 1.0$ *at initialization*
Elastic deviatoric strain increment $d\boldsymbol{e}^{el} = \frac{d\boldsymbol{s}}{2G}$ $G = G_o p_A \left(\frac{p}{p_A}\right)^{n_G} C_{SR} \left(\frac{1 + \frac{z_{cum}}{z_{max}}}{1 + \frac{z_{cum}}{z_{max}} C_{GD}}\right)$ $C_{SR} = \frac{1 - C_{SR,o}\left(\frac{M}{M^b}\right)^{m_{SR}}}{\left[1 - C_{SR,o}\left(\frac{M}{M^b}\right)^{m_{SR}}\right]_{initial}} \le 1.0$ $C_{SR,o} = 0.5$ $m_{SR} = 4$
Elastic volumetric strain increment $d\varepsilon_v^{el} = \frac{dp}{K}$ $K = \frac{2(1+v)}{3(1-2v)} G$
Yield surface $f = \left[(\boldsymbol{s} - p\boldsymbol{\alpha}) : (\boldsymbol{s} - p\boldsymbol{\alpha})\right]^{1/2} - \sqrt{1/2}\, pm = 0$ $m = 0.01$
Plastic deviatoric strain increment $d\boldsymbol{e}^{pl} = \langle L \rangle \boldsymbol{R}'$ $\boldsymbol{R} = \boldsymbol{R}' + \frac{1}{3} D\boldsymbol{I} = \boldsymbol{n} + \frac{1}{3} D\boldsymbol{I}$

$$M^b = M\ \exp\left(-n^{b,wet}\frac{\xi}{\lambda}\right) \quad for \quad \xi \geq 0$$

$$= M\left(\frac{1+C_{Mb}}{\frac{p}{p_{cs}}+C_{Mb}}\right)^{n^{b,dry}} \qquad for \quad \xi < 0$$

$$M = 2\cdot\sin\left(\phi_{cv}\right)$$

$$C_{Mb} = \frac{1}{\left(\frac{M^{b,\max}}{M}\right)^{1/n^{b,dry}} - 1}$$

$$M^{b,\max} = 2\cdot\sin\left(\phi_{\max}\right)$$

$$\boldsymbol{\alpha}^b = \sqrt{1/2}\left[M^b - m\right]\boldsymbol{n}$$

$$K_p = G\cdot h_o \frac{\left[\left(\boldsymbol{\alpha}^b - \boldsymbol{a}\right):\boldsymbol{n}\right]^{0.5}}{\left[\exp\left(\left(\boldsymbol{\alpha} - \boldsymbol{\alpha}_{in}^{app}\right):\boldsymbol{n}\right) - 1\right] + C_{\gamma 1}} C_{rev} \cdot \frac{C_{k\alpha}}{1 + C_{K_p}\left(\frac{z_{peak}}{z_{\max}}\right)\left\langle\left(\boldsymbol{\alpha}^b - \boldsymbol{a}\right):\boldsymbol{n}\right\rangle\sqrt{1 - C_{zpk2}}}$$

$$C_{rev} = \frac{\left(\boldsymbol{\alpha} - \boldsymbol{\alpha}_{in}^{app}\right):\boldsymbol{n}}{\left(\boldsymbol{\alpha} - \boldsymbol{\alpha}_{in}^{true}\right):\boldsymbol{n}} \quad for \quad \left(\boldsymbol{\alpha} - \boldsymbol{\alpha}_{in}^{p}\right):\boldsymbol{n} \leq \boldsymbol{0}$$

$$= 1 \quad otherwise$$

$$C_{K\alpha} = 1 + \frac{C_{K\alpha f}}{1 + \left(2.5\left\langle\left(\boldsymbol{\alpha} - \boldsymbol{\alpha}_{in}^{true}\right):\boldsymbol{n}\right\rangle\right)^2} C_{pzp2}\ C_{zpk1}$$

$$C_{zpk1} = \frac{z_{peak}}{z_{cum} + \frac{z_{max}}{5}}$$

$$C_{zpk2} = \frac{z_{peak}}{z_{cum} + \frac{z_{max}}{100}}$$

$$C_{pzp2} = \frac{-\left\langle-\left(p_{zp} - p\right)\right\rangle}{-\left\langle-\left(p_{zp} - p\right)\right\rangle + p_{\min}}$$

$$C_{\gamma 1} = \frac{h_o}{200}$$

$$C_{Kp} = 2$$

Plastic volumetric strain increment

$$d\varepsilon_v^{pl} = \langle L \rangle D$$

$$M^d = M \exp\left(n^d \frac{\xi}{\lambda} \right)$$

$$M^{dR} = \frac{M^d}{C_{rot1}}$$

$$C_{rot1} = 1 + \frac{2\langle -\boldsymbol{z} : \boldsymbol{n} \rangle}{\sqrt{2} z_{\max}} \left(1 - C_{zin1}\right) \geq 1$$

$$C_{zin1} = \left\langle 1 - \exp\left(-2.0 \left| \frac{\boldsymbol{z}_{in} : \boldsymbol{n} - \boldsymbol{z} : \boldsymbol{n}}{z_{\max}} \right| \right) \right\rangle$$

$$\alpha^d = \frac{1}{\sqrt{2}} \left(M^d - m \right) \boldsymbol{n}$$

$$\alpha^{dR} = \frac{1}{\sqrt{2}} \left(M^{dR} - m \right) \boldsymbol{n}$$

If dilating (D<0):

$$D_{non-rot} = A_d \left[\left(\boldsymbol{\alpha}^d - \boldsymbol{\alpha} \right) : \boldsymbol{n} \right]$$

$$D_{rot} = A_d \frac{\langle -\boldsymbol{z} : \boldsymbol{n} \rangle}{\sqrt{2} z_{\max}} \frac{(\alpha^{dR} - \alpha) : \boldsymbol{n}}{C_{DR}}$$

$$\text{if } \; D_{non-rot} < D_{rot} \;\; \Rightarrow \;\; D = D_{non-rot}$$

$$\text{else } \; D = D_{non-rot} + \left(D_{rot} - D_{non-rot} \right) \frac{\left\langle M^b - M^{cur} \right\rangle}{\left\langle M^b - M^{cur} + 0.01 \right\rangle}$$

$$A_d = \frac{A_{do}\left(C_{zin2}\right)}{\left(\frac{z_{cum}^2}{z_{\max}} \right) \left(1 - \frac{\langle -\boldsymbol{z} : \boldsymbol{n} \rangle}{\sqrt{2} \cdot z_{peak}} \right)^3 \left(C_{\varepsilon}\right)^2 \left(C_{pzp}\right) \left(C_{p\min}\right) \left(C_{zin1}\right) + 1}$$

$$A_{do} = \frac{1}{0.4} \frac{\left[\sin^{-1}\left(\frac{M^b}{2} \right) - \sin^{-1}\left(\frac{M}{2} \right) \right]}{M^b - M^d}$$

$$C_{pzp} = \frac{1}{1+\left(2.5p/p_{zp}\right)^5}$$

$$C_{p\min} = \frac{1}{1+\left(p_{\min}/p\right)^2}$$

$$C_{zin1} = 1.0 - \exp\left(-2.0\left|\frac{\boldsymbol{z}_{in}:\boldsymbol{n} - \boldsymbol{z}:\boldsymbol{n}}{z_{max}}\right|\right)$$

$$C_{zin2} = \frac{1 + C_{zin1}\dfrac{z_{cum} - z_{peak}}{3z_{max}}}{1 + 3C_{zin1}\dfrac{z_{cum} - z_{peak}}{3z_{max}}}$$

$$C_{DR} = 3.0$$

If contracting (D≥ 0)

$$D = A_{dc}\left[\left(\boldsymbol{\alpha} - \boldsymbol{\alpha}_{in}^{app}\right):\boldsymbol{n} + C_{in}\right]^2 \frac{\left(\boldsymbol{\alpha}^d - \boldsymbol{\alpha}\right):\boldsymbol{n}}{\left(\boldsymbol{\alpha}^d - \boldsymbol{\alpha}\right):\boldsymbol{n} + C_D} C_{p\min} \le A_{do}\frac{\left(\boldsymbol{\alpha}^d - \boldsymbol{\alpha}\right):\boldsymbol{n}}{\left(\boldsymbol{\alpha}^d - \boldsymbol{\alpha}\right):\boldsymbol{n} + C_D} C_{p\min}$$

$$A_{dc} = \frac{A_{do}\left(1 + \left\langle \boldsymbol{z}:\boldsymbol{n}\right\rangle\right)}{h_p C_{dz} C_{wet}}$$

$$C_{in} = \frac{2\left\langle \boldsymbol{z}:\boldsymbol{n}\right\rangle}{\sqrt{2}z_{max}}$$

$$C_{dz} = \left(1 - C_{rot2}\cdot\frac{\sqrt{2}z_{peak}}{z_{max}}\right)\left(\frac{z_{max}}{z_{max} + C_{rot2}z_{cum}}\right)$$

$$C_{rot2} = 1 - \frac{z_{peak}}{z_{cum} + \dfrac{z_{max}}{100}}\left(= 1 - C_{zpk2}\right)$$

$$C_D = 0.1$$

$$C_{wet} = \frac{1}{\dfrac{1}{1+\left(\dfrac{C_{w1}}{\left(\alpha^b - \alpha\right):\mathrm{n}}\right)^4} + \dfrac{1}{1+\left(\dfrac{\xi/\lambda}{C_{w2}}\right)^2}} \le 1$$

$$C_{w1} = 0.02$$

$$C_{w2} = 0.1$$

$$h_p = h_{po}\,\exp\left(-0.7 + 0.2\left(3 - \frac{\xi}{\lambda}\right)^2\right) \quad for \quad \frac{\xi}{\lambda} \le 3$$

$$h_p = h_{po}\,\exp(-0.7) \quad for \quad \frac{\xi}{\lambda} > 3$$

If $p < 2\,p_{min}$

$$D = -3.5 A_{do} \left\langle M^b - M^d \right\rangle \frac{2p_{\min} - p}{p_{\min}}$$

Fabric-dilatancy tensor update if $\left(\boldsymbol{\alpha}^d - \boldsymbol{\alpha}\right) : \mathbf{n} < 0$

$$d\mathbf{z} = -\frac{c_z}{1 + \left\langle \frac{z_{cum}}{2z_{max}} - 1 \right\rangle} \frac{\left\langle -d\varepsilon_v^{pl} \right\rangle}{D} \left(z_{max}\mathbf{n} + \mathbf{z}\right)$$

$$dz_{cum} = |d\mathbf{z}|$$

Stress increment

$$L = \frac{2G\mathbf{n} : d\mathbf{e} - \mathbf{n} : \mathbf{r} K d\varepsilon_v}{K_p + 2G - KD\mathbf{n} : \mathbf{r}}$$

$$d\boldsymbol{\sigma} = 2Gd\mathbf{e} + Kd\varepsilon_v \mathbf{I} - \langle L \rangle \left(2G\mathbf{n} + KD\mathbf{I}\right)$$

Post-shaking reconsolidation

$$G_{post-shaking} = F_{sed} G$$

$$K_{post-shaking} = F_{sed} K$$

$$G_{c,\min} = \left(\frac{8p}{\lambda}\right)\left(\frac{1}{1 + \left(C_{GC} - 1\right)\left(\frac{z_{cum}}{z_{cum} + z_{\max}}\right)}\right)$$

$$F_{consol} = 1 - \left(1 - \frac{G_{c,\min}}{G}\right)\left\langle 1 - \frac{M^{cur}}{M^d} \right\rangle^{0.25}$$

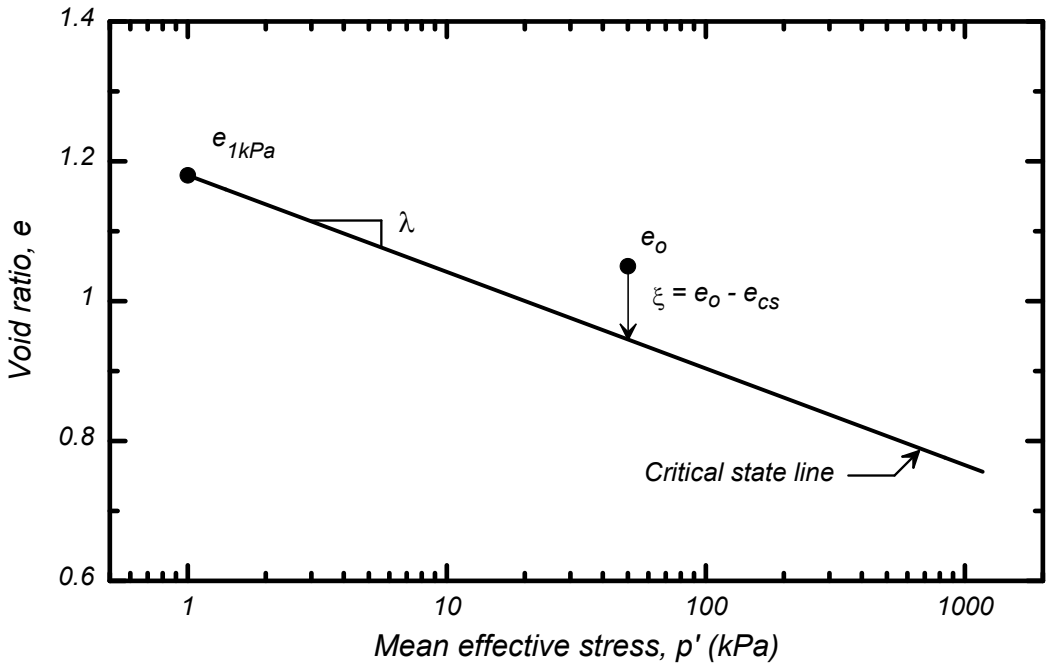

Figure 2.1. Schematic of the critical state line and state parameter ξ.

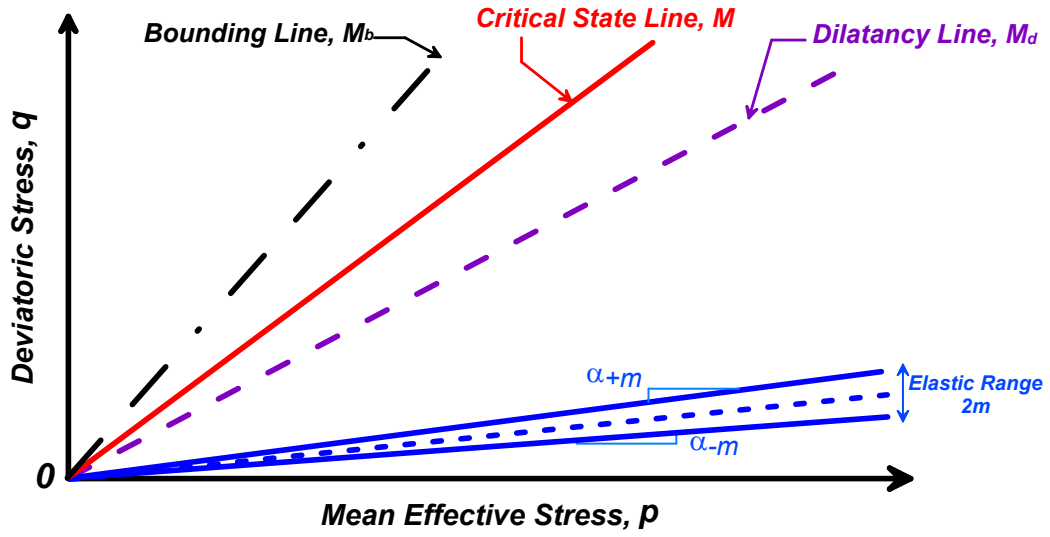

Figure 2.2. Schematic of yield, critical, dilatancy, and bounding lines in q-p space for a fixed value of state parameter (after Dafalias & Manzari 2004). Relative location of dilatancy and bounding lines corresponds to dense-of-critical states of stress.

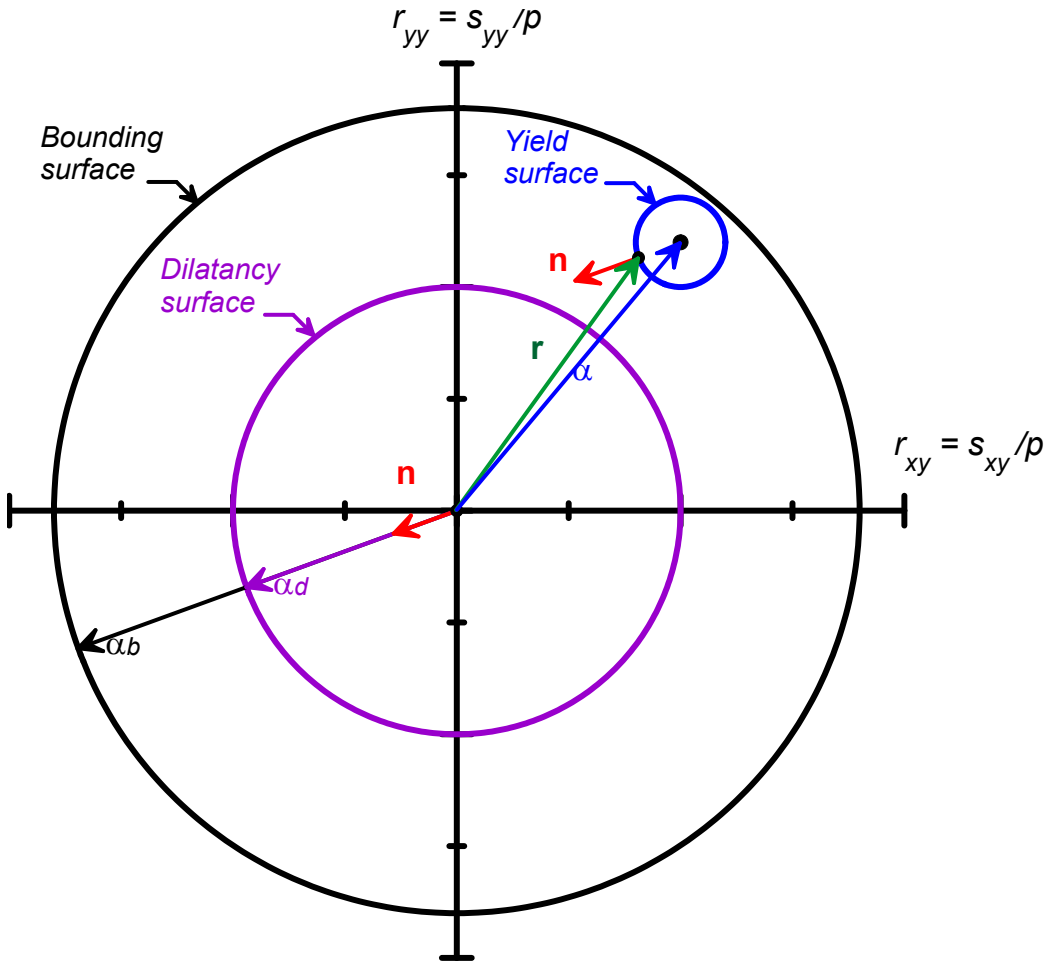

Figure 2.3. Schematic of the bounding, dilatancy, and yield surfaces on the r_{yy}-r_{xy} stress ratio plane with the yield surface, normal tensor, dilatancy back-stress ratio, and bounding back-stress ratio. Relative locations of the surfaces differ from those of Figure 2.2.

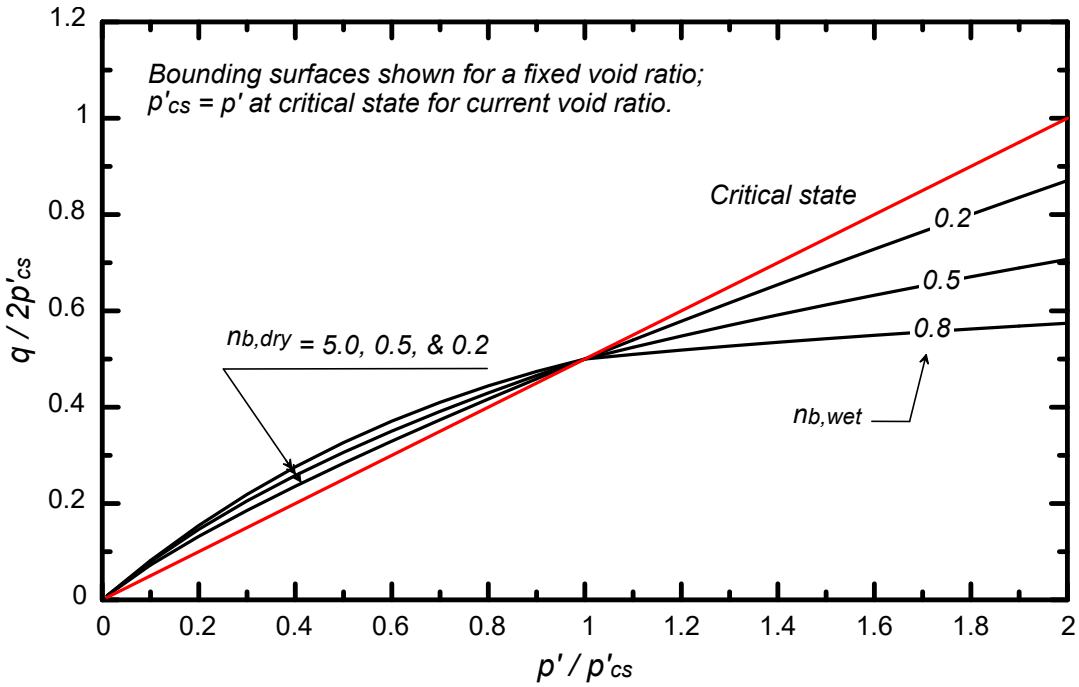

Figure 2.4. Schematic of the bounding lines and critical state line in q-p space for a fixed value of void ratio and a range of $n^{b,dry}$ values (for dense of critical state conditions) and $n^{b,wet}$ values (for loose of critical state conditions).

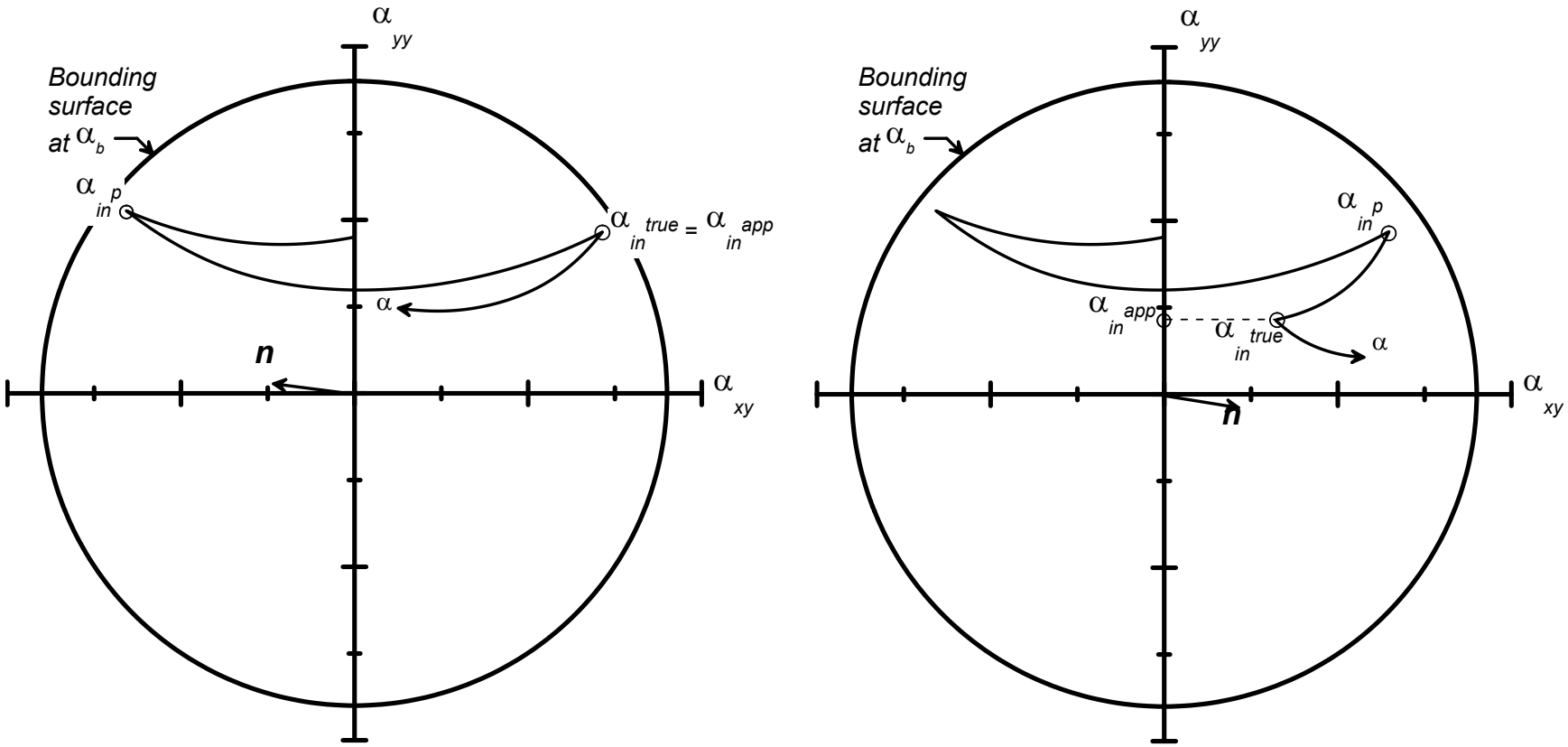

Figure 2.5. Schematic showing definitions of back-stress ratio tensors on the α_{yy}-α_{xy} plane for: (a) a loading history with reversals in the sign of the shear stress ratios, and (b) a loading history with a recent loading reversal that does not involve reversal of the sign of the shear stress ratios.

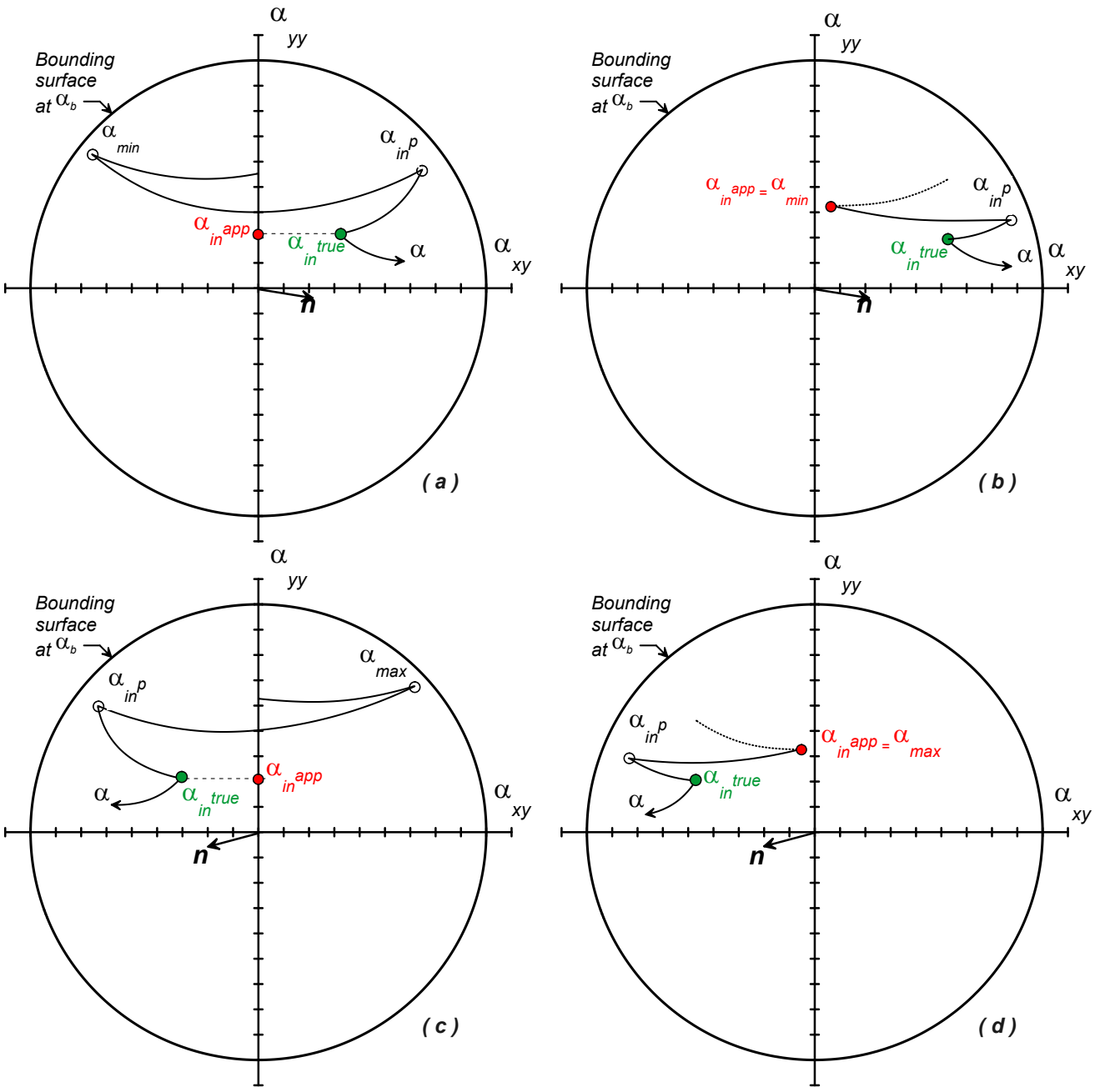

Figure 2.6. Example scenarios of back-stress ratio tracking: (a) positive loading direction with minimum value of back-stress ratio ($\boldsymbol{\alpha}_{\min}$) being less than zero such that $\boldsymbol{\alpha}_{in}^{app} = \boldsymbol{\alpha}_{in}^{true}$, (b) positive loading direction with minimum value of back-stress ratio ($\boldsymbol{\alpha}_{\min}$) being greater than zero such that $\boldsymbol{\alpha}_{in}^{app} = \boldsymbol{\alpha}_{min}$, (c) negative loading direction with maximum value of back-stress ratio ($\boldsymbol{\alpha}_{\max}$) being greater than zero such that $\boldsymbol{\alpha}_{in}^{app} = \boldsymbol{\alpha}_{in}^{true}$, (d) negative loading direction with minimum value of back-stress ratio ($\boldsymbol{\alpha}_{\max}$) being less than zero such that $\boldsymbol{\alpha}_{in}^{app} = \boldsymbol{\alpha}_{max}$.

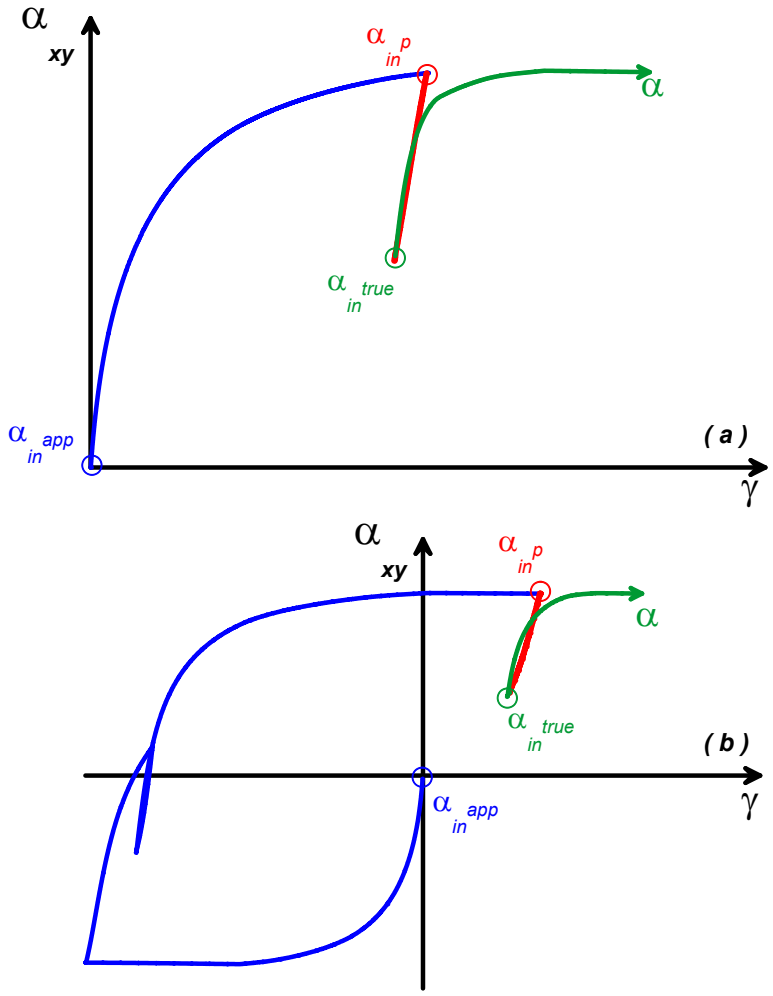

Figure 2.7. Drained DSS simulations showing α_{xy} versus γ with the points corresponding to the current back-stress ratio $\boldsymbol{\alpha}$, the apparent initial back-stress ratio $\boldsymbol{\alpha}_{in}^{app}$, the true initial back-stress ratio $\boldsymbol{\alpha}_{in}^{true}$, and the previous initial back-stress ratio $\boldsymbol{\alpha}_{in}^{p}$ for: (a) monotonic shearing with one intermediate unload-reload cycle, and (b) a more general sequence of cyclic loading.

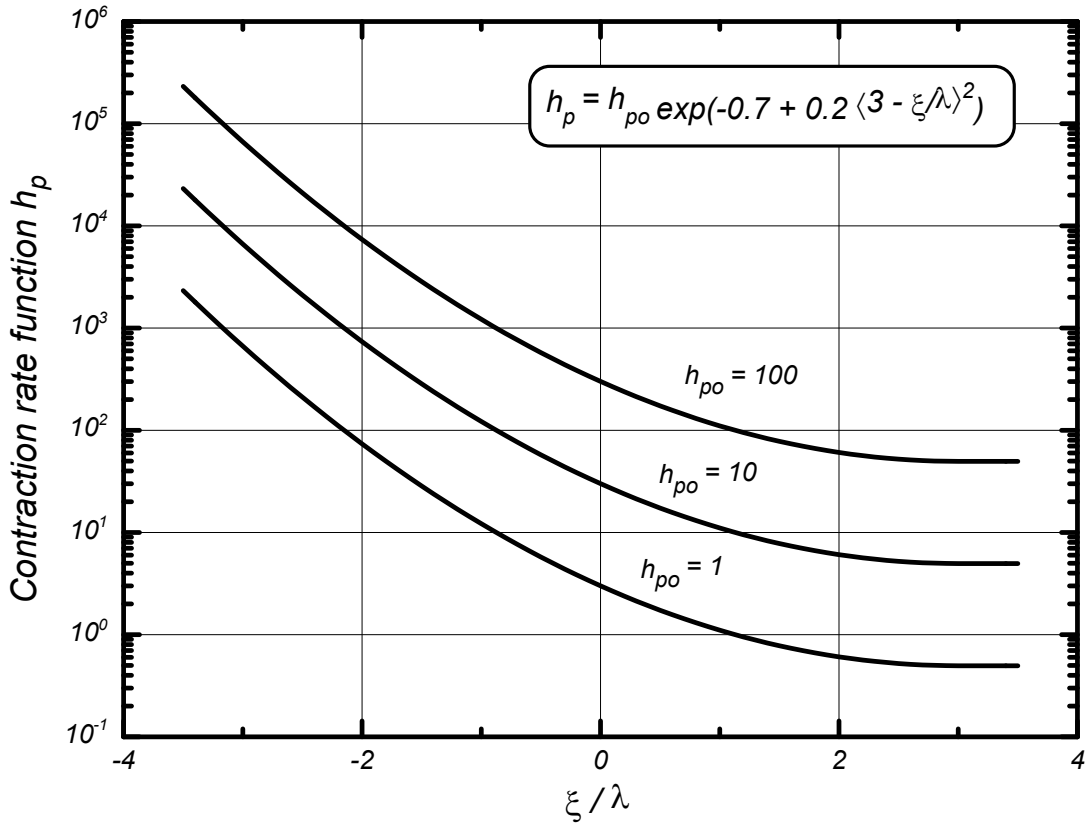

Figure 2.8. Variation of contraction rate function h_p with ξ/λ and contraction rate parameter h_{po}.

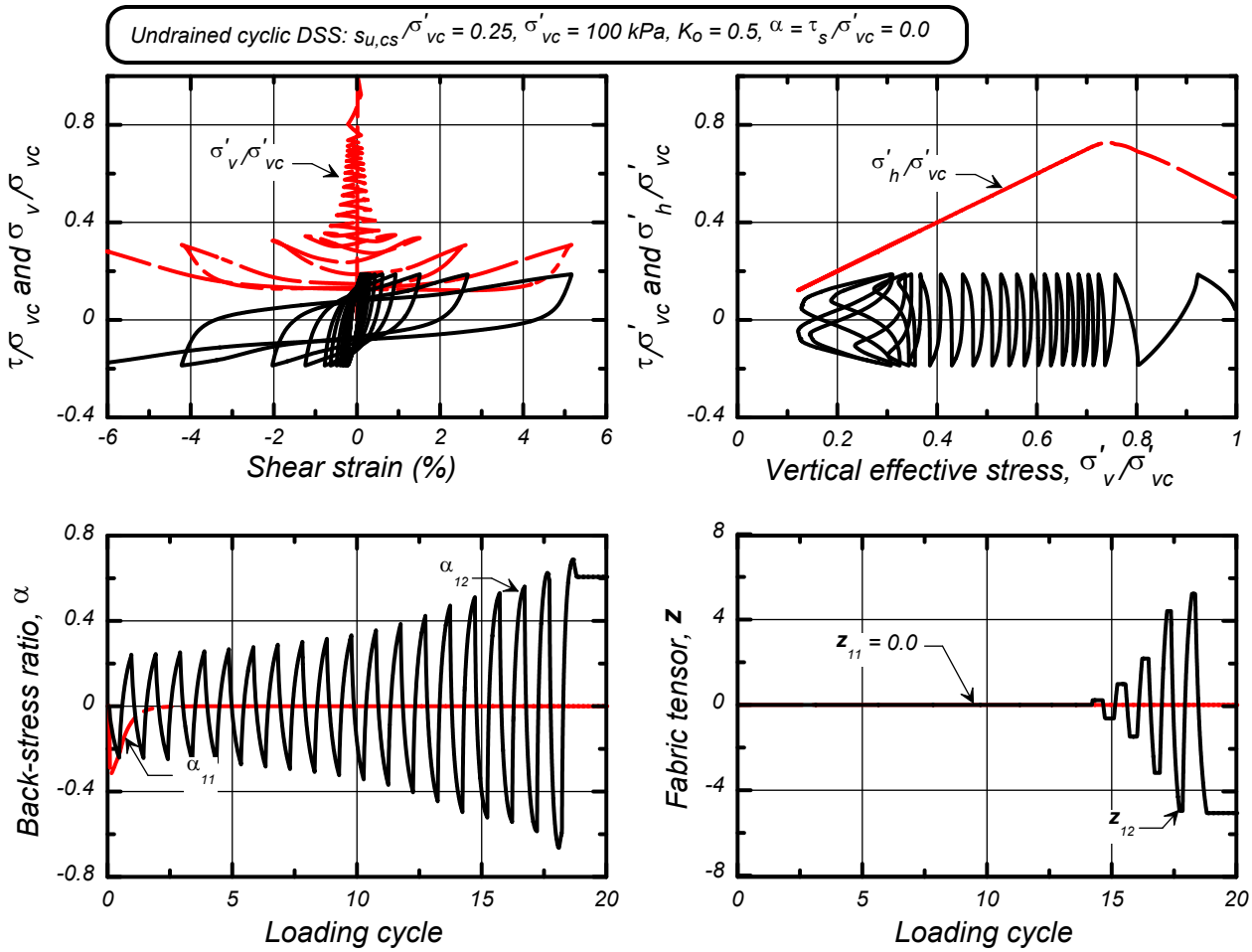

Figure 2.9. Undrained cyclic DSS loading response for $s_{u,cs}/\sigma'_{vc}$ = 0.25 with an initial static shear stress ratio of α=0.0, showing the variation in stresses, stress ratios, and fabric tensor terms.

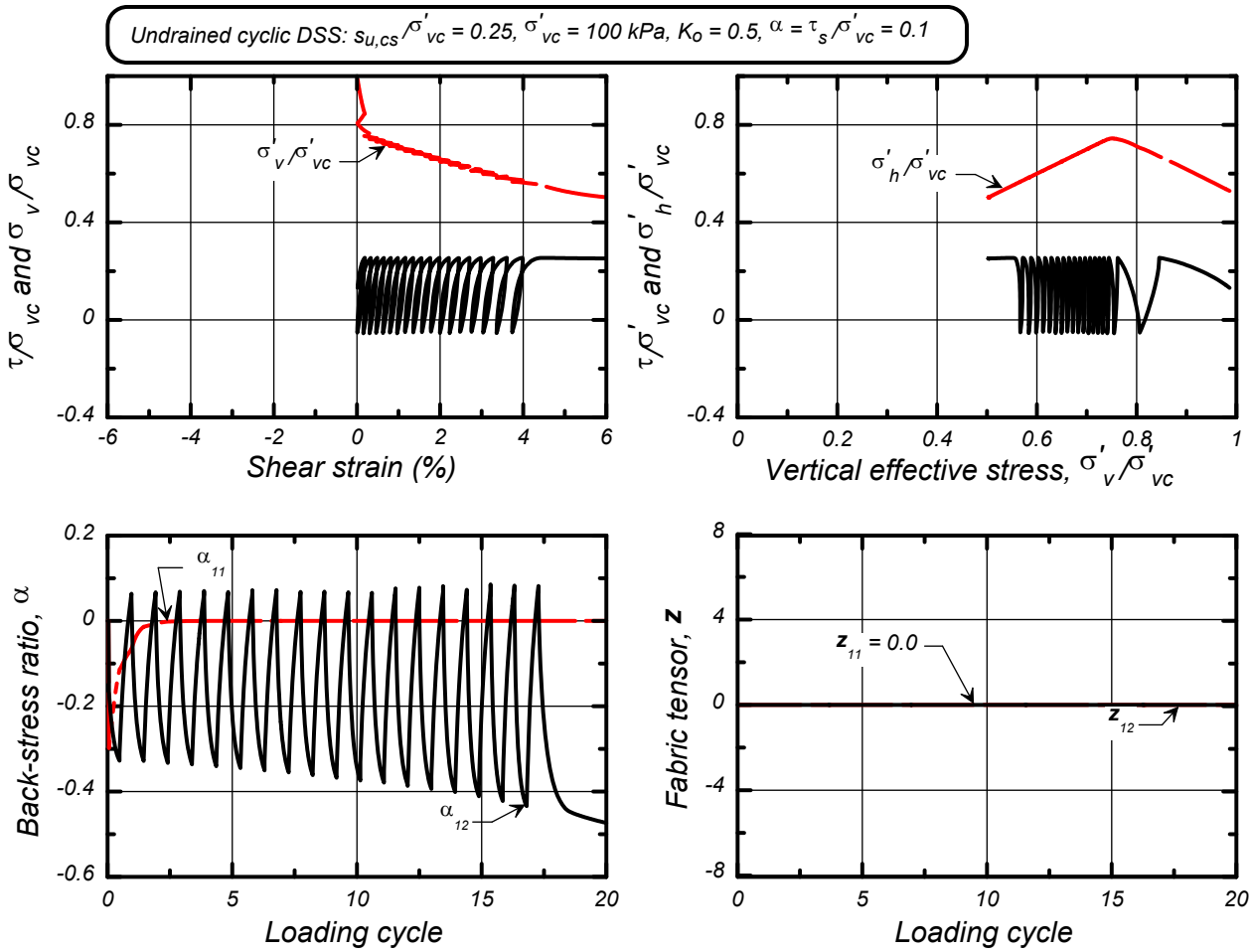

Figure 2.10. Undrained cyclic DSS loading response for $s_{u,cs}/\sigma'_{vc}$ = 0.25 with an initial static shear stress ratio of α=0.1, showing the variation in stresses, stress ratios, and fabric tensor terms.

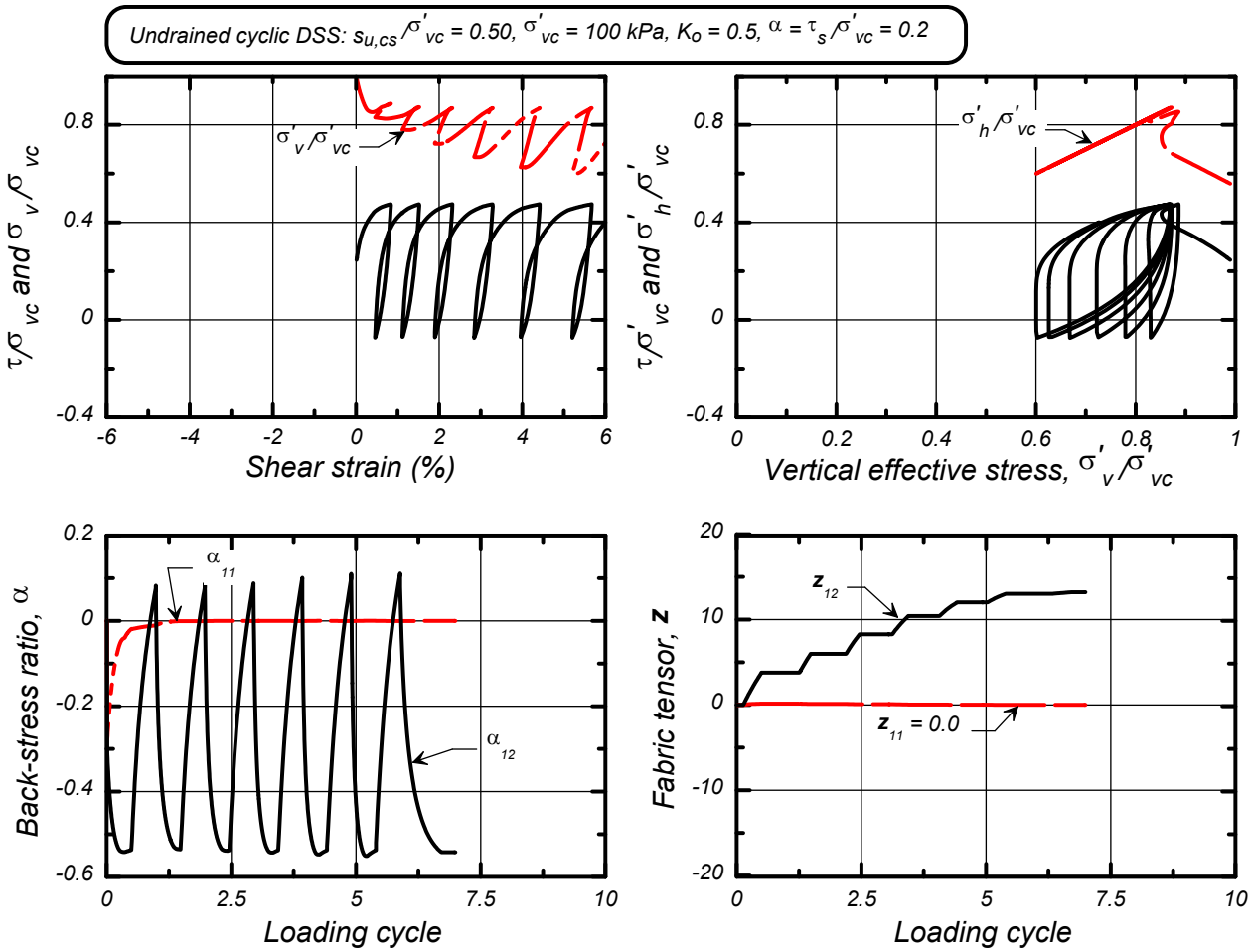

Figure 2.11. Undrained cyclic DSS loading response for $s_{u,cs}/\sigma'_{vc}$ = 0.5 with an initial static shear stress ratio of α=0.1, showing the variation in stresses, stress ratios, and fabric tensor terms.

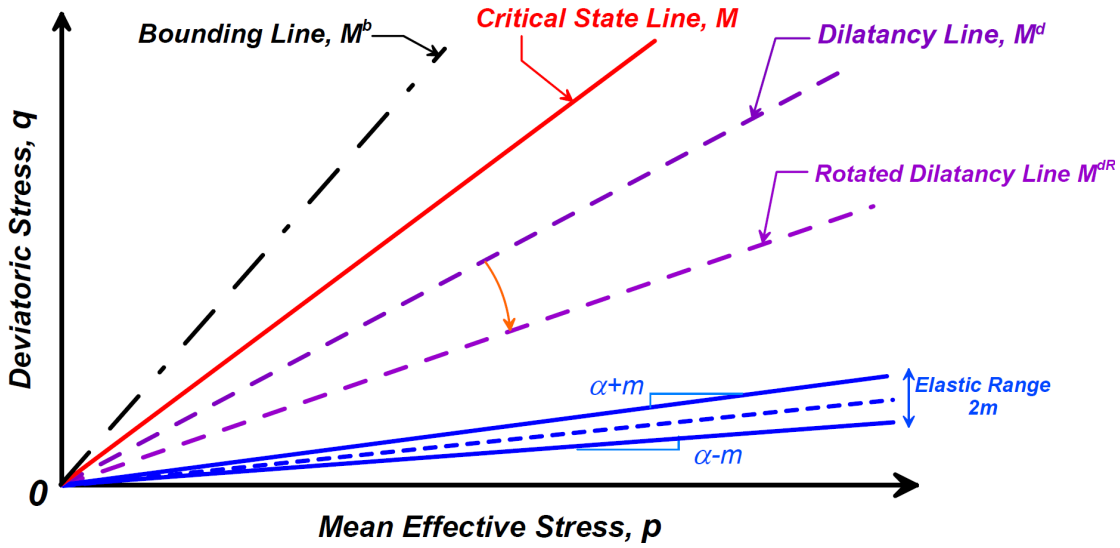

Figure 2.12. Schematic of the rotated dilatancy line, along with the yield, critical, dilatancy, and bounding lines in q-p space for a fixed value of state parameter. Relative location of dilatancy and bounding lines corresponds to dense-of-critical states of stress.

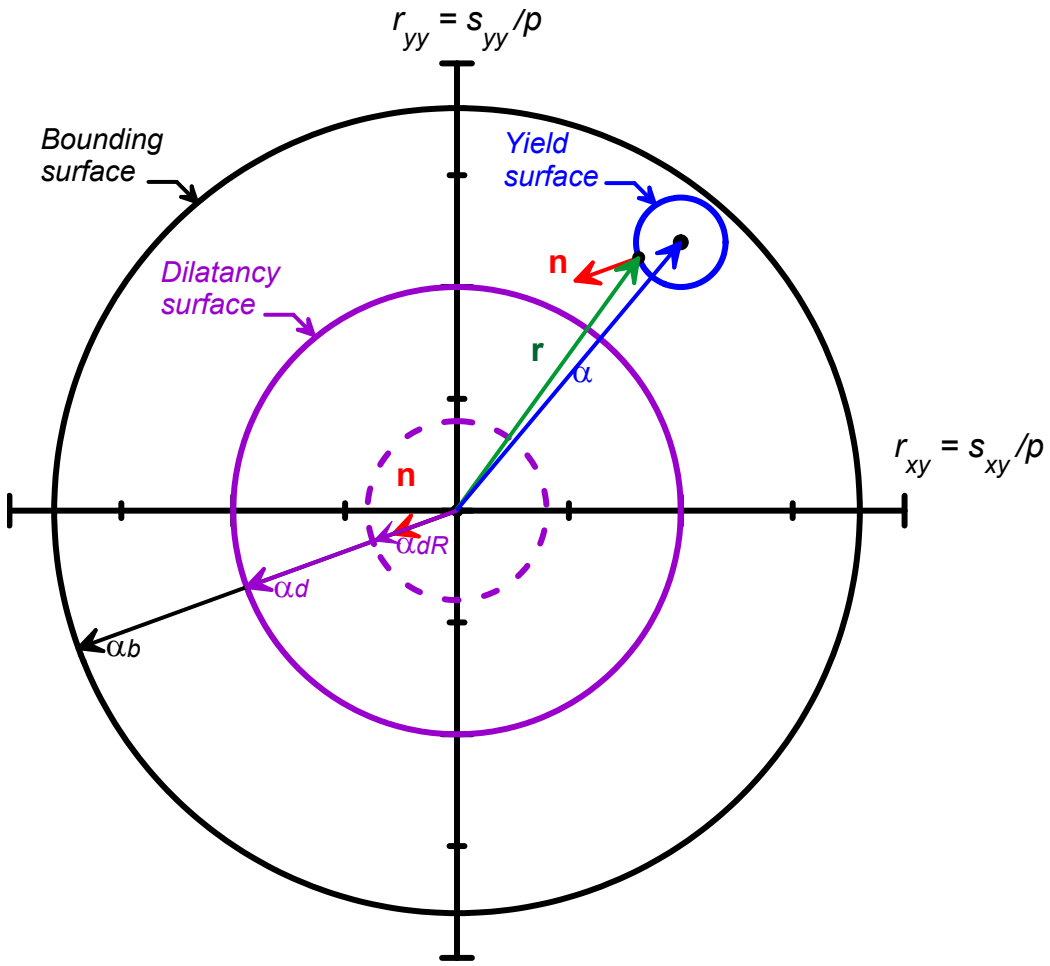

Figure 2.13. Schematic of rotated dilatancy line with the bounding, dilatancy, and yield surfaces on the r_{yy}-r_{xy} stress ratio plane with the yield surface, normal tensor, dilatancy back-stress ratio, and bounding back-stress ratio. Locations of the surfaces differ from those of Figure 2.9.

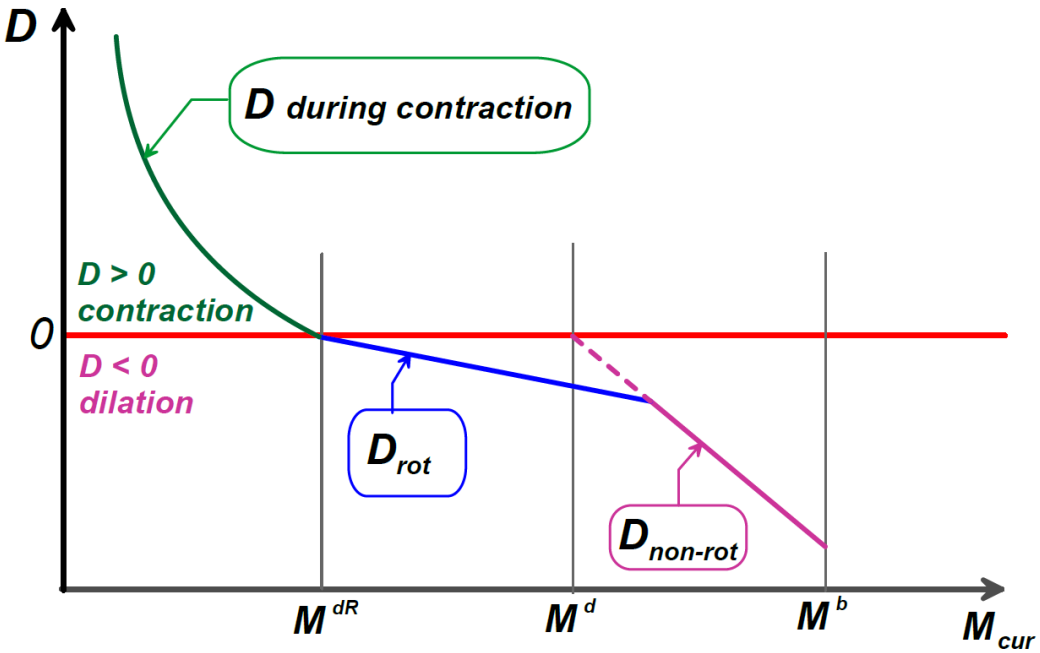

Figure 2.14. Schematic of dilatancy D calculation based on the stress state with regards to the rotated dilatancy (M^{dR}), dilatancy (M^{d}) and bounding (M^{b}) surfaces during a half-cycle of loading that goes from contraction to dilation.

3. MODEL IMPLEMENTATION

The PM4Silt model has been implemented as a user defined material (UDM) for use with the commercial finite difference program, FLAC 8.1 (Itasca 2019). This section includes a brief description of the numerical implementation scheme and information regarding the dynamic link library (DLL) and its use in boundary value problem simulations.

3.1 Numerical implementation

FLAC is an explicit finite difference program which uses time steps equal to or smaller than the minimum time required for waves to travel between any pair of nodes. This approach ensures that physical information does not propagate faster than numerical information. FLAC computes a default time step based on the properties of the model (e.g., element size, material stiffness, permeability, and damping). Users may specify a time step that is smaller than the default value.

Obtaining numerically convergent solutions to nonlinear problems using FLAC requires that integration of the constitutive models is convergent and the explicit global solution is convergent. The default time step computed by FLAC does not necessarily ensure a numerically convergent solution, especially for FLAC models that are subjected to very high loading rates. Convergence of the constitutive model's integration depends more strongly on the strain increment size, which is dependent on both the loading rate and time step size. Convergence of the explicit global solution depends more strongly on the sizes of the stress increments generated in the materials, which again are only indirectly controlled by the default time step size. For this reason, the user needs to evaluate the sensitivity of the solution to the time step size and not automatically assume that the default time step size ensures a convergent solution.

The numerical implementation of PM4Silt is identical to that used for PM4Sand, and thus the user is referred to the PM4Sand manual (Boulanger and Ziotopoulou 2022) for detailed descriptions of the code implementation, how it relates to FLAC's mixed discretization scheme, and examples of its performance across a range of time steps (or strain rates). The implementation scheme is described by the schematic in Figure 3.1, the pseudo-code listed in Table 3.1, and the initialization steps listed in Table 3.2. At the end of each time step, the stress and internal variables are averaged over the four subzones. A drift correction is applied to ensure that the averaged stresses and internal variables satisfy the consistency condition; the correction involves projecting the back-stress ratio in the direction of the zone-averaged stress ratio. Another correction is applied if the zone-averaged stress ratio lies outside the bounding surface; the correction involves projecting the zone averaged stress ratio back along a normal to the bounding surface. The zone-averaged stresses are then used to compute a new dilatancy D and plastic modulus K_p that are consistent with the average response of the zone over this step. These values for D and K_p are then used by all four subzones in the next time step (i.e., the values of D and K_p lag one step behind the time step for which they were determined); note that this approach is used by other elasto-plastic models available in FLAC. Consequently, the four subzones will use a common D and K_p during each time step. Most other internal parameters are also computed and retained at the zone level, as described by the pseudo-code in Table 3.1.

The implementation includes a scheme to reduce hour-glassing modes which can develop in liquefied zones with essentially zero shear resistance. The four subzones have, in parallel to the PM4Silt constitutive model, an elastic-plastic resistance to shear stresses which acts independently in each of the subzones. The properties of this parallel elastic-plastic model are set at the instance when PM4Silt is initialized; the elastic moduli of the parallel elastic-plastic model are set equal to 0.1 times those for PM4Silt, and its plastic shear strength (c_{hg}) is set as the product of a strength ratio (cr_{hg}) times the mean effective stress in the zone. If the user specifies values for both c_{hg} and cr_{hg}, then c_{hg} is taken as the greater of the specified c_{hg} value and the value computed using the specified cr_{hg}. The default value for cr_{hg} is 0.001. The value for c_{hg} is constrained to be greater than or equal to $p_A/1000$ and less than or equal to $0.1s_{u,cs}$. These default values are smaller than used for PM4Sand because hour-glassing is less of an issue for PM4Silt calibrations that do not produce near-zero effective stresses. The parallel elastic-plastic model only responds to deviatoric strains (producing shear stresses) and not to volumetric strains (producing no mean stress). This nominal amount of independent shearing resistance in the subzones was found to adequately control hour-glassing modes for the range of problems examined to date.

The implementation of PM4Silt uses explicit integration and thus the user should routinely check that the solutions are not sensitive to time step size. The addition of substepping could improve the constitutive model's integration but would not eliminate the need to evaluate the effect of time step size on the global solution. In the developers' experiences, the default time steps of FLAC in dynamic analyses of liquefaction problems have been small enough to ensure that numerical solutions are not significantly affected by time step size, and thus the additional computational cost of including substepping at the constitutive level was not considered necessary. An example of the effects of time step size on cyclic loading response in a single element simulation is given in Figure 3.2. Additional examples of the effects of time step size on element responses and system level responses, using PM4Sand, are presented in Boulanger and Ziotopoulou (2020).

Numerical stability of the implemented model has been evaluated for a wide range of simulations of both element responses and system responses using the default range of parameters which are also summarized in the next section. Numerical stability problems may, however, develop when using input parameters which fall outside the ranges explored during model development, calibration, and implementation. Some initial bounds have therefore been placed on certain parameters whenever parametric analyses identified the potential for such problems; e.g., the minimum value of mean stress is limited to 0.5 kPa or 0.005 times the initial consolidation stress. The user must be aware that other limits may be identified as additional analyses explore a broader range of the possible input parameters.

3.2 DLL module

The PM4Silt model was coded in C++ and compiled as a User Defined Model (UDM) dynamic link library (DLL) in Microsoft Visual Studio 2015 for FLAC 8.1 and in Microsoft Visual Studio 2022 for FLAC2D 9.0. The steps required for using a DLL are described in the respective FLAC/FLAC2D manuals.

3.3 Additional notes on use in boundary value problem simulations

FLAC includes both "static" and "dynamic" solution procedures. PM4Silt has been extensively validated for dynamic applications, but has also been used for static applications. FLAC's static solution procedure uses extremely high damping values which can carry significant shear and normal stresses, which can cause problems with the response of a highly nonlinear, stress-dependent materials. For example, if the user imposes a large strain rate (e.g., high rate of loading on a foundation) in a problem involving drained loading of a contractive soil with the static solution procedure, the drained volumetric contraction of the soil can result in normal stresses being transferred to the damping component which causes an artificial reduction in normal effective stress in the soil. For this reason, the use of PM4Silt with FLAC's static solution procedure requires a higher degree of scrutiny and evaluation to ensure that such problems do not develop.

A nominal amount of Rayleigh damping should be included with PM4Silt zones to control numerical noise during dynamic solutions. A damping ratio of 0.005 has been found sufficient for most applications.

Zones at the ground surface, particularly within slopes and above the water table, are susceptible to developing large deformations at strong shaking levels (i.e., when the frictional shear resistance is exceeded). Excessive distortion of surface zones can lead to premature stoppage of a simulation, particularly for soils that liquefy or cyclically soften. Some analysts will use Mohr Coulomb materials in lieu of complex sand models for surface zones, for which they can then include a nominal amount of cohesion to reduce the potential for surficial shear failures. In the current version of PM4Silt, a similar effect can be achieved by increasing the nominal shear resistance c_{hg} above the default value used to control hour-glassing in liquefied zones.

Loading conditions that cause a progressive increase in the mean effective stresses in PM4Silt, or any other pressure-dependent material, require special consideration during the solution process. The elastic moduli will increase with increasing mean effective stress, such that the time step required for a stable solution will decrease as the loading progresses. FLAC only determines the required time step at certain instances, like when the step or solve commands are executed. For this reason, the loading should be applied in small increments with the solve command periodically repeated so that the required time step is updated as appropriate during the applied loading.

Initial stresses in a boundary value problem are sometimes established using simpler constitutive models, like a Mohr Coulomb or elastic model, prior to switching the materials to a more complex model like PM4Silt. Problems can develop if the initial states of stress fall outside the greater of the bounding and dilatancy surface lines for the PM4Silt model. This can happen in zones where the initial state of stress was computed for a Mohr Coulomb material with a nonzero cohesion or for an elastic material. For this reason, it is helpful to first ensure that the initial states of stress in all zones correspond to a stress ratio that is less than some reasonable limit prior to switching the material model to PM4Silt.

The ability to use the DLL with FLAC's "free-field" lateral boundary conditions option or compliant base option has not been configured at this time. Thus, the user should not have PM4Silt in the outer column of elements against which the free-field lateral boundary condition will be applied. Instead, the outer columns can be replaced with elastic materials having a secant modulus compatible with the adjacent PM4Silt zones.

Table 3.1: Simplified pseudo-code of PM4Silt

Operations within one subzone:

1. Initialize the model parameters; this only happens when the model is first assigned or when FirstCall is set to zero at some point during the analysis. For detailed information on what parameters are initialized (or reset) see Table 3.2.

2. Obtain the strain increment from FLAC $d\boldsymbol{\varepsilon}$.

3. Decompose the strain increment into volumetric and deviatoric components, $d\varepsilon_p$ and $d\varepsilon_s$.

4. Calculate the trial elastic stress increment and trial elastic stress:

$$\boldsymbol{\sigma}_{tr} = \boldsymbol{\sigma}_0 + d\boldsymbol{\sigma}_{tr} = \boldsymbol{\sigma}_0 + 2Gd\boldsymbol{\varepsilon}_s + Kd\varepsilon_p\boldsymbol{I}$$

5. Calculate the trial stress ratio,$\boldsymbol{r_{tr}}$ the distance from the yield surface $dist$, the unit normal to the yield surface $\boldsymbol{n}$ and the inner product of the change in back-stress ratio tensor with unit normal vector *daxn*.

$$\boldsymbol{r}_{tr} = \frac{\boldsymbol{\sigma}_{tr} - p_{tr}\boldsymbol{I}}{p_{tr}}$$

$$dist = \sqrt{(\boldsymbol{r}_{tr} - \boldsymbol{\alpha}_0) : (\boldsymbol{r}_{tr} - \boldsymbol{\alpha}_0)}$$

$$\boldsymbol{n} = \frac{(\boldsymbol{r}_{tr} - \boldsymbol{\alpha}_0)}{dist}$$

$$daxn = (\boldsymbol{\alpha}_0 - \boldsymbol{\alpha}_{in}) : \boldsymbol{n}$$

6. Check for yield:

a. If elastic then commit the trial stresses. Go to step 8.

$$dist < \frac{1}{\sqrt{2}}m$$

$$\boldsymbol{\sigma}_0 = \boldsymbol{\sigma}_{tr}$$

b. If inelastic:

i. Calculate loading index L:

$$L = \frac{2G\boldsymbol{n} : d\boldsymbol{e} - \boldsymbol{n} : \boldsymbol{r}Kd\varepsilon_v}{K_p + 2G - KD\boldsymbol{n} : \boldsymbol{r}}$$

ii. Calculate trial stress increment and trial stress:

$$\boldsymbol{\sigma}_{tr} = \boldsymbol{\sigma}_0 + d\boldsymbol{\sigma}_{tr} = \boldsymbol{\sigma}_0 + 2Gd\boldsymbol{\varepsilon}_s + Kd\varepsilon_p\boldsymbol{I} - L\{2G\boldsymbol{n} + KD\boldsymbol{I}\}$$

iii. Apply penalties to stress ratios and back-stress ratios to meet the consistency condition and to remain within the greater of the bounding and dilatancy surfaces.

iv. Calculate image back-stress ratios and inner products:

$$\boldsymbol{\alpha}^b = \sqrt{1/2}\left[M^b - m\right]\boldsymbol{n}$$

$$\boldsymbol{\alpha}^d = \sqrt{1/2}\left[M^d - m\right]\boldsymbol{n}$$

$$\boldsymbol{\alpha}^{dR} = \sqrt{1/2}\left[M^{dR} - m\right]\boldsymbol{n}$$

v. Commit the trial stresses (back-stress ratios, stress ratio, mean stress, stress)

7. Return all stress tensor components to FLAC (at this point FLAC takes over and will average them according to the mixed discretization scheme)

Operations referring to the whole zone:

8. After the calculation has completed the 4th subzone, the following additional calculations are performed for the overall zone. Recall the following parameters for all 4 subzones and compute area-weighted average values for:

- Volumetric strain $d\bar{\varepsilon}_p$
- Strain increment $\bar{d\boldsymbol{\varepsilon}}$
- Mean stress $\bar{p}$
- Stress tensor (committed one) $\bar{\boldsymbol{\sigma}}_0$
- Back-stress ratio tensor $\bar{\boldsymbol{\alpha}}_0$
- Unit normal to yield surface vector $\bar{\boldsymbol{n}}$

9. Apply penalties to the averaged zone parameters to meet the consistency condition and maintain the yield surface inside the greater of the bounding and dilatancy surfaces.

10. Calculate image back-stress ratios and inner products for the averaged zone parameters.

11. Calculate daxn for the averaged zone parameters and determine whether a loading reversal has occurred.

12. Compute Dilatancy D and Plastic Modulus K_p for the past average step in the zone.

13. Compute plastic volumetric strain for use in fabric terms.

14. If $\left(\boldsymbol{\alpha}^d - \boldsymbol{\alpha}\right) : \boldsymbol{n} < 0$, update the fabric tensor for the zone and if exceeding its former value, update the cumulative fabric term.

$$z = z - \frac{c_z}{max\left(1, \frac{z_{cum}}{2z_{max}}\right)} \frac{d\bar{\varepsilon}_p}{D}\left(z_{max}\bar{\boldsymbol{n}}\right) + z$$

15. Update the relative state parameter, the bounding and dilatancy stress ratios, the elastic shear modulus (depends on fabric) and the elastic bulk modulus for the next step.

16. Update the initial and previous initial back-stress values and the strain increment accumulators.

17. Update initial back-stress ratios upon reversal.

18. Commit zone stress tensor, zone mean stress, zone back-stress ratio tensor, zone stress ratio tensor to memory.

Table 3.2: Initialization function of PM4Silt (called during the first application of the model and whenever FirstCall=0)

1. Obtain stresses from FLAC and create stress tensor (these will be the committed stresses from which the calculation will start):

$$\boldsymbol{\sigma_o^{ij}}$$

2. Check stresses and calculate mean effective stress:

a. If stresses tensile:

$$\sigma_o^{11} > 0 \;\rightarrow\; p_o \;=\; -\frac{P_{atm}}{20}$$

$$\boldsymbol{\sigma_o^{ij}} = p_o \cdot [I]$$

b. If stresses compressive (following FLAC's sign convention that tensile stresses and strains are positive):

$$\sigma_o^{11} < 0 \;\rightarrow\; p_o \;=\; min\left(-0.5kPa, \frac{1}{2}\sigma_o^{ii}\right)$$

$$p_{min} = \frac{p_{cs}}{8} > p_o \text{ or } p_{min} = \left(1 - r_{u,max}\right)\frac{p_o}{2}$$

3. Position the critical state line, calculate state parameter and subsequently calculate the bounding M^b and dilatancy M^d stress ratios:

$$\Gamma = e + \lambda ln\left(101.3\frac{2s_{u,cs}}{MP_A}\right)$$

$$\xi = e - \Gamma + \lambda ln\left(101.3\frac{p}{P_A}\right)$$

4. Check that initial stresses are inside the greater of the bounding and dilatancy surfaces and compute the committed back-stress and stress ratio tensors from the stress tensor:

$$M^{fin} = -\frac{2}{p_0} \cdot \sqrt{\frac{1}{2}\left(\boldsymbol{\sigma_o^{ij}} - p_o[I]\right) : \left(\boldsymbol{\sigma_o^{ij}} - p_o[I]\right)}$$

a. If $M^{fin} > M^{cut}$ *where* M^{cut} *is the greater of* M^b *and* M^d:

$$\boldsymbol{r_o^{ij}} = \left(\frac{\boldsymbol{\sigma_o^{ij}} - p_o[I]}{p_o}\right)\left(\frac{M^{cut}}{M^{fin}}\right)$$

$$\boldsymbol{\sigma_o^{ij}} = p_o[I] + \boldsymbol{r_o^{ij}} p_o$$

$$\boldsymbol{\alpha_o^{ij}} = \boldsymbol{r_o^{ij}} \cdot \frac{M^{cut} - m}{M^{cut}}$$

b. If $M^{cut} > M^{fin}$:

$$\boldsymbol{r_o^{ij}} = \left(\frac{\boldsymbol{\sigma_o^{ij}} - p_o[I]}{p_o}\right)$$

$$\boldsymbol{\alpha_o^{ij}} = \boldsymbol{r_o^{ij}}$$

5. Create/Initialize the initial back-stress ratio, initial previous back-stress ratio, minimum initial back-stress ratio and maximum initial back-stress ratio tensors (see also Section 2.5 on Stress Reversal):

a. If $M^{fin} < 0.9M^b$:

$$\boldsymbol{\alpha_{in}^{ij}} = \boldsymbol{\alpha_o^{ij}}$$

b. If $M^{fin} > 0.9M^b$:

$$\boldsymbol{\alpha_{in}^{ij}} = \boldsymbol{\alpha_o^{ij}}\left(\frac{0.9M^b}{M^{fin}}\right)$$

Note that M^{fin} in the above expression would have been updated if step 4 had required adjusting the stresses. The other back-stress ratio history terms are then set as:

$$\boldsymbol{\alpha_{inP}^{ij}} = \boldsymbol{\alpha_{inMax}^{ij}} = \boldsymbol{\alpha_{inMin}^{ij}} = \boldsymbol{\alpha_{in}^{ij}}$$

6. Calculate initial values of elastic shear modulus, elastic bulk modulus, plastic modulus, dilatancy:

$$G = G_o P_{atm} \sqrt{\frac{-p_o}{P_{atm}}}$$

$$K = G\frac{2(1+v)}{3(1-2v)}$$

$$K_p = 100G$$

$$D = 0$$

7. Initialize fabric related terms (see Section 2.8) – note that these terms will be referring to the whole zone:

$$p_{zp} = \frac{p_o}{100}$$

$$z_{peak} = \frac{z_{max}}{100000}$$

$$zxp = \boldsymbol{z}{:}\,p = 0$$

$$zxpPk = -z_{max}\frac{p_o}{50}$$

$$\boldsymbol{z^{ij}} = \boldsymbol{z_{in}^{ij}} = \boldsymbol{z_{\alpha}^{ij}} = z_{cum} = 0$$

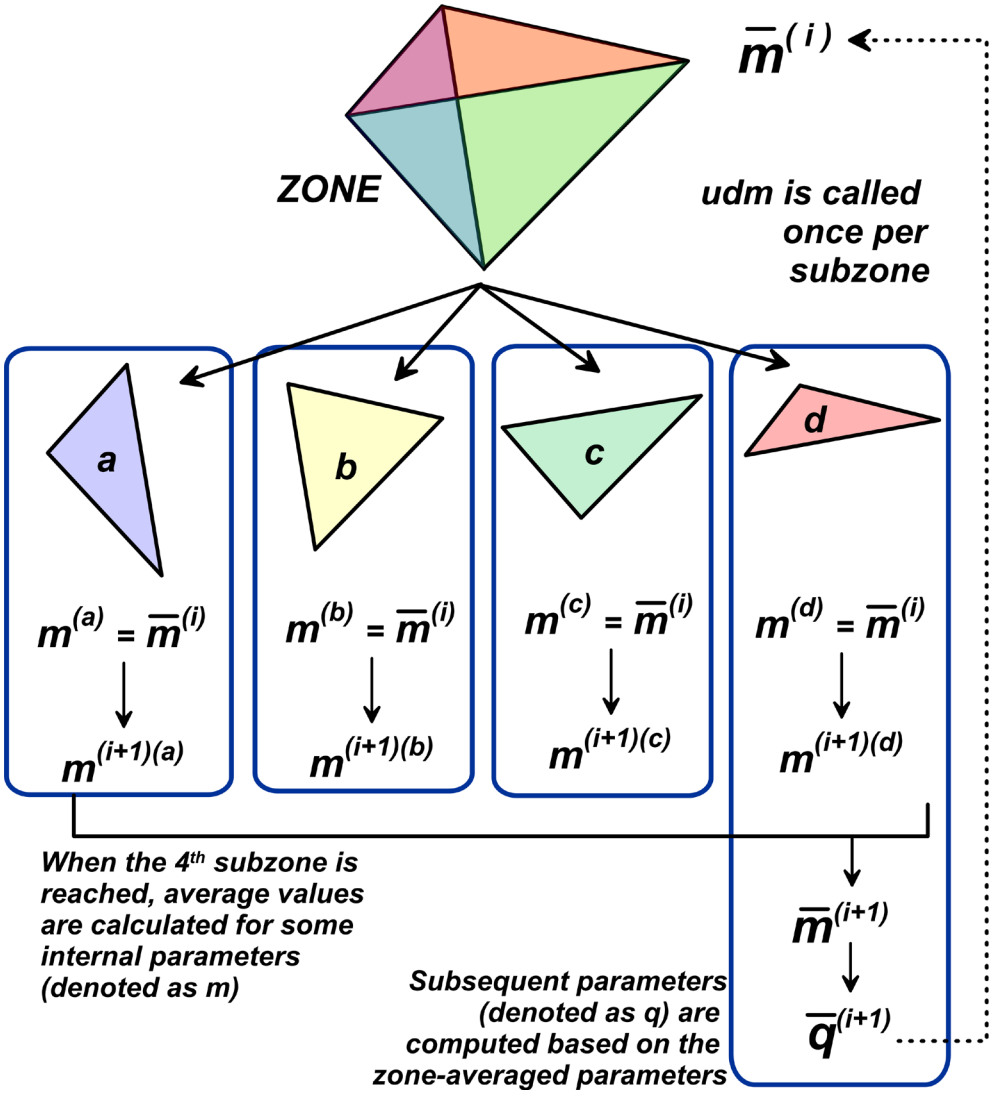

Figure 3.1 Schematic illustration of the averaging procedure followed in the implementation of PM4Silt: zone-averaged values are computed for some internal variables of the model, denoted as “m”, at the end of each step, after which other internal parameters, denoted as “q”, are computed based on the zone-averaged parameters

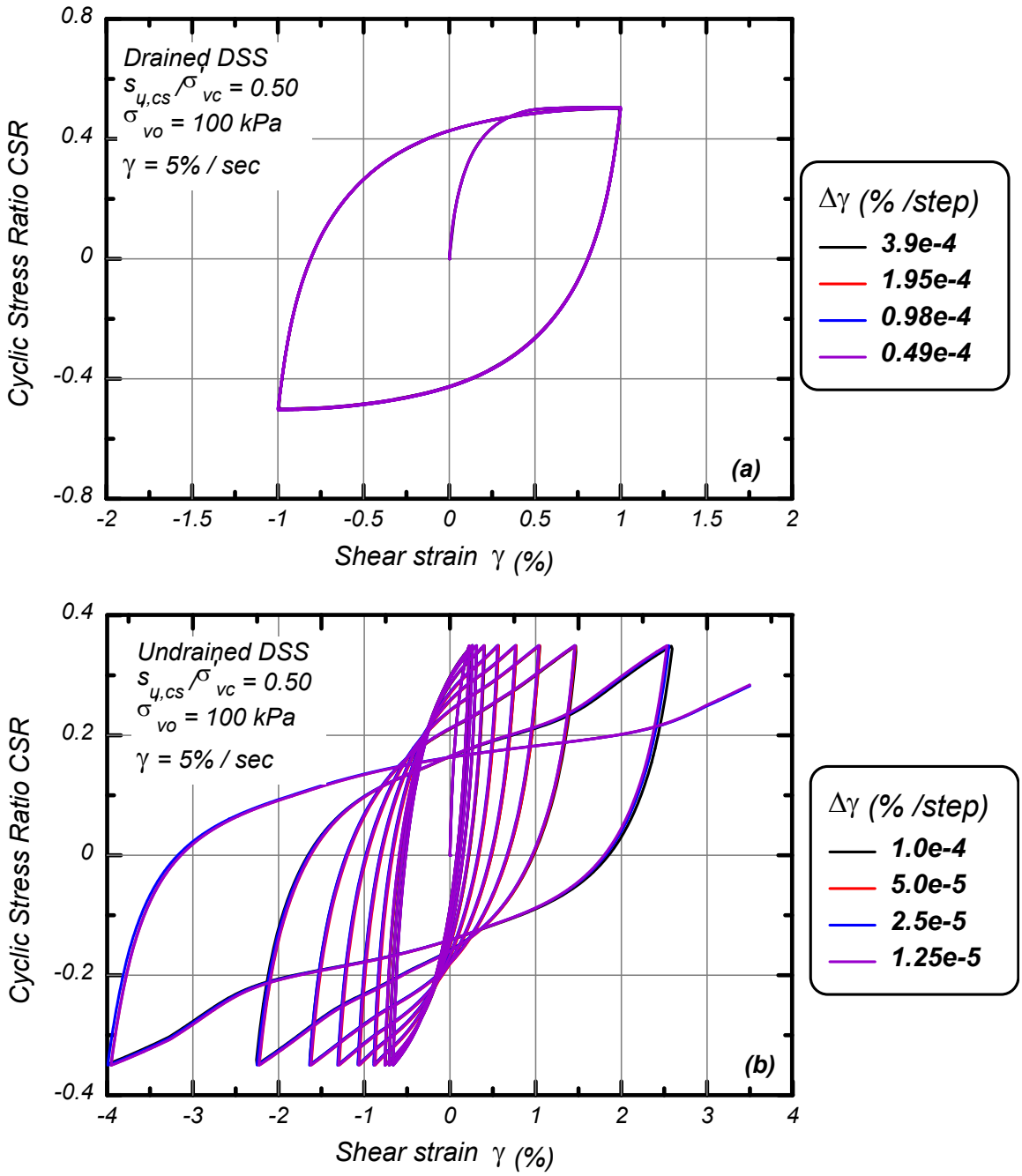

Figure 3.2 Effect of dynamic time step on the results obtained from (a) drained and (b) undrained cyclic DSS element test simulations for baseline properties with s_u/σ'_{vc} =0.5, σ'_{vc} = 1atm, and a shear strain rate of 5%/s. The black line in each case denotes the response obtained with FLAC's default dynamic time step.

4. MODEL INPUT PARAMETERS AND RESPONSES

4.1 Model input parameters

The model parameters are grouped into a set of primary parameters (three required soil parameters, one optional soil parameter, one initialization flag, and a unit set indicator) and a set of 20 secondary parameters. Default values are provided for all but the three required primary parameters, which are the minimum required inputs for model calibration. The secondary parameters may warrant adjustment from their default values if site-specific laboratory test data are available for calibration.

Primary input parameters

The four primary soil parameters are the soil's undrained shear strength at critical state under earthquake loading ratios ($s_{u,cs,eq}$) (or the corresponding undrained shear strength ratio $s_{u,cs,eq}/\sigma'_{vc}$), the shear modulus coefficient G_o, the contraction rate parameter h_{po}, and the post-shaking shear strength reduction factor (F_{su}). The first three are required parameters, whereas the fourth is optional. These parameters are discussed below and summarized in Table 4.1.

The s_u of low-plasticity silts and clays can be estimated in practice by a combination of in situ testing (e.g., cone penetration tests, vane shear tests), laboratory testing of "undisturbed" field samples (e.g., consolidated undrained triaxial or direct simple shear tests), and empirical correlations for undrained shear strength ratio versus overconsolidation ratio (e.g., Figure 1.2). The undrained stress-strain response at strains greater than a few percent can range from strain-hardening for highly overconsolidated soils (i.e., dense-of-critical) to strain-softening for normally consolidated or lightly overconsolidated soils (i.e., loose-of-critical). In addition, the s_u is rate dependent (e.g., Sheehan et al. 1996) such that the shear resistance during earthquake loading can be 20-40% greater than measured in standardized laboratory tests that use far slower loading rates (e.g., Boulanger and Idriss 2007).

The first required soil parameter is the s_u that corresponds to critical state conditions at the strain rate expected during earthquake shaking (i.e., $s_{u,cs,eq}$). The peak s_u produced by PM4Silt can be greater than $s_{u,cs,eq}$ if the other input parameter selections (particularly the combination of $n^{b,wet}$ and h_{po}) produce post-peak strain-softening behavior, as illustrated later.

Alternatively, the s_u values can be initialized by specifying an undrained shear strength ratio ($s_{u,cs,eq}/\sigma'_{vc}$) that is used to compute $s_{u,cs,eq}$ from the σ'_{vc} at "consolidation" (i.e., at the time of model initialization or whenever the parameter FirstCall is set equal to zero). If the user inadvertently specifies values for both $s_{u,cs,eq}$ and $s_{u,cs,eq}/\sigma'_{vc}$, the value of $s_{u,cs,eq}$ is used.

The value specified for $s_{u,cs,eq}$ is used internally to compute e_{1kPa}, conditional on the other input parameters, and thereby position the critical state line at the time of model initialization as illustrated in Figure 4.1. For this reason, the undrained monotonic and cyclic loading responses are generally insensitive to variations in e_o or λ.

The s_u values for post-shaking stability should correspond to critical state conditions at the slower strain rate associated with static stability (i.e., $s_{u,cs,static}$). The input parameter F_{su} is used to reduce the s_u for the post-strong-shaking portion of the analysis by an amount that accounts for the slower strain rates and any expected effects of cyclic degradation or remolding.

$$s_{u,cs,static} = F_{su} \cdot s_{u,cs,eq} \tag{94}$$

The input parameter F_{su} reduces $s_{u,cs}$ by shifting the critical state line leftward relative to its initial position; i.e., re-setting F_{su} at different times will reduce the strength relative to the strength for F_{su} = 1.0, not relative to the prior F_{su} value. The default value for F_{su} is 1.0. A value for F_{su} can be specified at any time, but the intended use is for it to be set at the end of strong earthquake shaking, after which the dynamic analysis should be continued for sufficient time to evaluate post-shaking stability. The code does not require that a value for F_{su} be specified during the analysis, and thus it is the user's responsibility to evaluate whether the selected input parameters provide appropriately conservative strengths for evaluating post-shaking stability.

Another required soil parameter is the constant G_o which controls the elastic (or small-strain) shear modulus. The equation for the elastic shear modulus at the time of model initialization can be simplified to,

$$G = G_o p_A \left(\frac{p}{p_A} \right)^{n_G} \tag{95}$$

The full equation for the elastic shear modulus (Equation 88) includes adjustments for the effects of stress ratio and fabric, but these adjustment terms both are equal to unity at the time of model initialization (Equations 27 and 88). The elastic shear modulus can be calibrated to fit in-situ V_s measurements, according to,

$$G = \rho \cdot \left(V_s \right)^2 \tag{96}$$

or alternatively fit to values of V_s that may be estimated by correlations. The shear modulus exponent n_G has a default value of 0.75, but may be adjusted as warranted. Calibration of G to fit in-situ V_s measurements requires an estimate for the in-situ coefficient of earth pressure at rest (K_o) for computing p (i.e., the mean of the vertical and horizontal stresses for the present 2D implementation; Equation 2). Maintaining consistency between the calibration procedure and the boundary value problem solution requires that the initial K_o conditions in the boundary value problem reasonably match the value assumed during calibration.

The initial K_o conditions in the boundary value problem should also be compatible with the peak undrained shear strength ratio for the soil. For example, the initial K_o value should not be smaller than one minus two times the peak undrained shear strength ratio (e.g., $K_o > 0.6$ if $s_{u,pk,eq}/\sigma'_{vc} = 0.20$), or the model will be initializing at stress states above the bounding surface.

Initializing the model with unreasonably small K_o values can adversely affect the stress-strain responses, including the modulus reduction and damping values at smaller strains.

The third required soil parameter is the constant h_{po} which is used to modify the contractiveness and hence enable calibration of the model to specific values of cyclic resistance ratio (CRR). For the examples presented herein, the target CRR values were based on the cyclic strength correlations by Boulanger and Idriss (2007) and Dahl (2011). These relationships are intended for the range of loading rates expected during earthquakes, recognizing that the cyclic strength for low plasticity silts and clays exhibit a strain-rate dependence comparable to that observed for s_u (e.g., Lefebvre and LeBouef 1987, Zergoun and Vaid 1994, Lefebvre and Pfendler 1996, Boulanger et al 1998). These relationships indicate that the cyclic stress ratio to cause a peak shear strain of 3% in 30 uniform load cycles at earthquake loading rates is about 70-90% of the soil's $s_{u,static}/\sigma'_{vc}$ (e.g., Figure 1.6) or about 55-70% of the soil's $s_{u,eq}/\sigma'_{vc}$ (allowing for $s_{u,eq}$ being greater than $s_{u,static}$ due to rate effects); thus, h_{po} should be calibrated based on the latter range because the $s_{u,eq}$ is generally used for the strong shaking portion of the dynamic analysis.

The flag FirstCall is used to: (1) re-set the back-stress ratio history terms equal to the current stress ratio, (2) erase all fabric terms, and (3) compute $s_{u,cs,eq}$ using the current σ'_v if the option for inputing $s_{u,cs,eq}/\sigma'_{vc}$ was used. The first time the model is called, the flag should be unspecified or have a value of 0. The model will then initiate the back-stress ratios and all pertinent history terms using the current state of stress. The flag is then set equal to 1.0 internally. If FirstCall is later set equal to 0.0 using the property command in FLAC, this will cause the material to re-initiate all internal terms, thereby re-setting the back-stress and stress ratio history terms, erasing all fabric terms, and re-computing $s_{u,cs,eq}$ (if applicable). FirstCall should usually be set to 0.0 just before initiating dynamic earthquake loading. Otherwise, the model will retain memory of the loading during the static initiation of the model, which may or may not be desired.

The value of atmospheric pressure, p_A, should also be specified in the unit set being used for the analysis. If not specified, it will default to 101,300 Pascal.

Table 4.1 – Primary input parameters (parameter names in square brackets correspond to the input name to be used within FLAC)

Parameter [FLAC property name]	Comments
$s_{u,cs,eq}$ [S_u] or $s_{u,cs,eq}/\sigma'_{vc}$ [Su_Rat]	**Undrained shear strength (Required):** Required parameter that is used to position the critical state line (i.e., sets e_{1kPa}) to obtain the specified undrained shear strength at critical state for the current void ratio ($s_{u,cs,eq}$). A value for $s_{u,cs,eq}/\sigma'_{vc}$ is computed internally from the σ'_{vc} at "consolidation" (i.e., at the time of model initialization or whenever the parameter FirstCall is set equal to zero). The user may instead specify an undrained shear strength ratio ($s_{u,cs,eq}/\sigma'_{vc}$) that is used to compute $s_{u,cs,eq}$ from the σ'_{vc} at "consolidation" (i.e., at the time of model initialization or whenever the parameter FirstCall is set equal to zero). If the user inadvertently specifies values for both $s_{u,cs,eq}$ and $s_{u,cs,eq}/\sigma'_{vc}$, the value of $s_{u,cs,eq}$ is used.
G_o [G_o]	**Shear modulus coefficient (Required):** Primary variable controlling the small-strain shear modulus, G_{max}. At model initialization, the equation for G_{max} simplifies to, $G_{max} = G_o p_A \left(\frac{p}{p_A} \right)^{n_G}$ G_o should be chosen to match estimated or measured shear wave velocities according to $G_{max} = \rho V_s^2$. Note that the exponent n_G has a default value of 0.75, but may also be adjusted as warranted.
h_{po} [h_po]	**Contraction rate parameter (Required):** Primary variable that adjusts contraction rates and hence can be adjusted to obtain a target cyclic resistance ratio. Calibration of this parameter should be performed last because its value can depend on the values assigned to other parameters.

F_{su} [Su_factor]	**Undrained shear strength reduction factor (Optional):** Primary variable that can be used to reduce the $s_{u,cs}$ value relative to the value at the time of initialization (i.e., when F_{su} had its default value of 1.0). This parameter can be set at the end of strong shaking, and thus used to evaluate post-strong-shaking static stability using strengths appropriate for the slower loading rates and any estimated effects of cyclic degradation or remolding. $s_{u,cs,static} = F_{su} \cdot s_{u,cs,eq}$
FirstCall [First_Call]	**Flag (Optional)**, that when set to 0.0 sets the back-stress ratio history terms equal to the current stress ratio, erases all fabric terms, and computes $s_{u,cs}$ based on the current effective stress conditions (if the strength ratio option was used). FirstCall defaults to 0.0 at model initialization. FirstCall usually should also be set to 0.0 just before initiating dynamic earthquake loading. Otherwise, the model will retain memory of the loading during the static initiation of the model, which may or may not be desired.
p_A [P_atm]	**Atmospheric pressure** in the unit set being used. Defaults to 101,300 Pascals if not specified.

Secondary input parameters

Secondary input parameters are those parameters for which default values have been developed that will generally produce reasonable behaviors. The secondary input parameters are listed in Table 4.2, along with commentary on the recommended default values. The selected values for these parameters have been embedded within the initialization section of the code and unless specified otherwise by the user, they are applied by default. In addition, the input logic is structured such that secondary parameters will take their default value if the user inputs a value of zero for that parameter.

The secondary parameters that are most likely to warrant adjustment from their default values will depend on the nature of the soil's responses in site-specific laboratory testing. Past experience suggests that the parameters h_o, $n^{b,wet}$, z_{max}, c_e, and c_z, are often the most effective in improving site-specific calibrations, while the parameters $r_{up,max}$, C_{DG}, and $C_{k\alpha}$ can also be effective in certain situations.

The last secondary parameter is the flag PostShake, which can be used during the post-shaking portion of a simulation to improve the modeling of post-liquefaction reconsolidation strains. The flag is set to 0 internally and remains 0 unless the user specifies otherwise. If the flag is set to 1.0, the elastic moduli will be reduced according to the expressions presented previously. PostShake should only be set to 1.0 at the end of strong shaking, as the reductions in elastic moduli were not calibrated for dynamic loading behavior.

Table 4.2 – Secondary input parameters

Parameter [FLAC name]	Comments
n_G [G_exp]	**Shear modulus exponent (Optional):** Primary variable controlling how the small-strain shear modulus (discussed above) varies with confining stress. Default value is 0.75.
h_o [h_o]	Variable that adjusts the ratio of plastic modulus to elastic modulus. The default value of h_o=0.5 was chosen to provide reasonable G/G_{max} and damping relationships for the baseline set of model calibrations. This variable may require adjustment to improve the G/G_{max} and damping behavior for other model calibrations.
e_o [e_o]	The initial void ratio primarily affects how volumetric strains translate into changes in state parameter. Default value is 0.90. Changing e_o does not affect the undrained shear strength, because the code positions the critical state line relative to e_o based on the specified undrained shear strength.
λ [lambda]	The slope of the critical state line in e-ln(p) space. Default value is 0.060. Changing λ influences how ξ varies with changing p, but the influence on model response is not strong because most behaviors depend on ξ/λ.
ϕ'_{cv} [phi_cv]	Default value is 32 degrees.
$n^{b,wet}$ [n_bwet]	Default value is 0.80, with upper and lower limits of 1.0 and 0.01, respectively. The degree to which the peak s_u may exceed the critical state $s_{u,cs}$ increases with decreasing $n^{b,wet}$.
$n^{b,dry}$ [n_bdry]	Default value is 0.5. Controls peak effective friction angles for dense of critical state conditions, and thus influences undrained cyclic loading behaviors.
n^d [n_d]	Default value is 0.30. Controls the stress ratio at which contraction transitions to dilation, which is often referred to as phase transformation.
A_{do} [A_do]	Default value of 0.8 provides approximate consistency with stress-dilatancy relationships.

$r_{up,max}$ [ru_max]	If $r_{up,max}$ is specified, p_{min} is set equal to $(1-r_{up,max})p/2$ at the time of initialization. If $r_{up,max}$ is not specified, the internal parameter p_{min} defaults to $1/8^{th}$ of p_{cs} for the void ratio at initialization, but not smaller than the p_{min} computed using $r_{up,max} = 0.0$. For either case, p_{min} is restricted to be greater than, or equal to, $p_A/200$ (i.e., 0.5 kPa). The $r_{up,max}$ specified here (which is based on p) is different from the form commonly used to interpret DSS tests (which is based on σ'_{vc}); this difference in definitions needs to be accounted for in calibration.
z_{max} [z_max]	Default value is computed at the time of initialization as, $z_{max} = 10 \quad for \quad \frac{s_{u,cs}}{\sigma'_{vc}} \le 0.25$ $z_{max} = 40\left(\frac{s_{u,cs}}{\sigma'_{vc}}\right) \quad for \quad 0.25 < \frac{s_{u,cs}}{\sigma'_{vc}} \le 0.50$ $z_{max} = 20 \quad for \quad \frac{s_{u,cs}}{\sigma'_{vc}} > 0.50$ Can be adjusted to improve approximation of site-specific laboratory test data. Increasing z_{max} increases maximum excess pore pressure, reduces width of hysteresis loops, reduces cyclic strength, steepens the CRR-cycles curve, and increases rate of strain accumulation.
c_z [c_z]	Default value is 100. Controls strain levels at which fabric effects become important. Values between 50 and 250 typical.
c_ε [c_e]	Default value increases from 0.5 to 1.3 as $s_{u,cs,eq}/\sigma'_{vc}$ increases: $c_\varepsilon = 0.5 + 1.2\left\langle \frac{s_{u,cs}}{\sigma'_{vc}} - 0.25 \right\rangle \le 1.3$ Can be used to adjust the rate of strain accumulation in undrained cyclic loading.
C_{GD} [G_degr]	Default value is 3.0. The small-strain elastic modulus degrades with increasing cumulative plastic deviator strains (z_{cum}). The maximum degradation approaches a factor of $1/C_{GD}$.
$C_{k\alpha f}$ [Ckaf]	Default value is 4.0. This variable can adjust the effect that sustained static shear stress has on plastic modulus and hence cyclic strength. Its effects are small for loose-of-critical state conditions, and becomes more significant as state becomes increasingly dense-of-critical.

ν_o [pois]	Default value is 0.30. For 1-D consolidation of an elastic material, the value of K_o would correspond to, $K_o = \frac{\nu}{1-\nu}$ The default value for ν results in a K_o value of 0.43 in 1-D consolidation.
cr_{hg} [MC_ratio]	Default value is 0.001. Nominal plastic shear strength ratio used to compute c_{hg} at the time of initialization or when FirstCall is set equal to 0.
c_{hg} [MC_c]	Nominal plastic shear strength assigned at initialization or when FirstCall is set equal to 0. It is computed as the greater of: (1) cr_{hg} times p, and (2) the user-specified value for c_{hg}. It is also constrained to be no smaller than 0.001 atm and no greater than 0.1 $s_{u,cs,eq}$.
PostShake [Post_Shake]	**Flag (optional)** that can be used during post-shaking portion of a simulation to improve modeling of post-liquefaction reconsolidation strains. Set PostShake = 1.0 to activate this option; note that PostShake should only be activated after the end of strong shaking.
C_{GC} [CG_consol]	Default value is 2.0, and it is restricted to values ≥1. This is the factor by which the estimated elastic modulus for 1D reconsolidation is degraded (divided by) when the value of $z_{cum} >> z_{max}$. Larger values result in greater post-cyclic loading reconsolidation strains.

Tracking variables

Many of the parameters internal to PM4Silt may be tracked for debugging purposes. The table below lists some of the internal parameters that may be of interest. Other internal parameters that can be tracked include: max_G, max_K, pmin, MM, alfa_11, alfa_12, r_11, r_12, aIn_11, aIn_12, aInP_11, aInP_12, z_11, z_12, zcum, zpeak, zxpPk, pzp, zxp, Cka, eqsum, evsum, LoadInd, Dilat, Kp, zabs, evol, eq_11, eq_22, eq_12, epsIncr and daxn. Other internal parameters are visible through the FLAC interface, and can be phonetically mapped to different terms in constitutive equations in this manual.

Table 4.3 – Internal parameters available for tracking

Parameter [FLAC Name]	Comments
M^b [Mb]	Bounding surface stress ratio
M^d [Md]	Dilatancy surface stress ratio
M^{cur} [Mcur]	Current stress ratio
G [shearG]	Elastic shear modulus
K [bulkK]	Elastic bulk modulus
e [e_cur]	Current void ratio
e_{1kPa} [e_1]	Critical state line intercept at p = 1 kPa
ξ [st_param]	State parameter

4.2 Model responses with default calibration for secondary parameters

The response of the model is illustrated by presenting simulation results for an example set of primary input parameters, while all secondary parameters receive their default values. Results are presented for soils having undrained shear strength ratios of 0.25, 0.5, and 0.75 with G_o values of 588, 776, and 913, respectively. These undrained strength ratios were assumed to correspond to overconsolidation ratios (OCR) of 1.0, 2.4, and 3.6, for which K_o was assumed to be 0.50, 0.75, and 1.0. Values for h_{po} were calibrated to produce a reasonable slope for the CRR versus number of uniform loading cycles curve in direct simple shear (DSS) simulations. The default values for all other parameters, as summarized previously in Tables 4.1 and 4.2, were used for all simulations unless otherwise noted. The primary model parameters for the examples presented in this section are listed in Table 4.4.

Table 4.4. Input parameters for example element responses

Model input parameters [(a)]			Implied OCR	Assumed K_o	Implied V_{s1} [(b)] (m/s)
$s_{u,cs,eq}/\sigma'_{vc}$	G_o	h_{po}			
0.25	500	20	1.0	0.5	148
0.5	660	50	2.4	0.75	180
0.75	780	80	3.6	1.0	206

[(a)] All other input parameters were assigned the default values listed in Tables 4.2.
[(b)] Assuming saturated density of 1.87 Mg/m^3.

Undrained monotonic loading

The response in undrained monotonic loading in direct simple shear (DSS) for soils with $s_{u,cs,eq}/\sigma'_{vc}$ = 0.25, 0.50, and 0.75 under vertical consolidation stresses of ¼, 1, 2, 4, and 16 atm are shown in Figure 4.2, with the results normalized by the vertical consolidation stress. Initial K_o values listed in Table 4.4 were used for all simulations. The normalized stress-strain responses were strain-hardening for $s_{u,cs,eq}/\sigma'_{vc}$ = 0.5 and 0.75, but included some post-peak softening for $s_{u,cs,eq}/\sigma'_{vc}$ = 0.25. The normalized stress-strain responses show that slightly greater strains are required to reach different stress levels as the confining stress increases, which is expected because the default n_G = 0.75 is less than unity; if n_G = 1.0, then both strength and stiffness are proportional to confining stress and the normalized stress-strain responses become independent of consolidation stress.

The effect of $n^{b,wet}$ on the undrained monotonic loading response for $s_{u,cs,eq}/\sigma'_{vc}$ = 0.25 and σ'_{vc} = 1.0 atm is shown in Figure 4.3. Reducing $n^{b,wet}$ from the default value of 0.8 results in the peak shear resistance becoming progressively larger, with an associated increase in the amount of post-peak strain-softening since the critical state strength remains the same.

The effect of F_{su} on the undrained monotonic loading response is illustrated in Figure 4.4 for $s_{u,cs,eq}/\sigma'_{vc}$ = 0.25 and σ'_{vc} = 1.0 atm. The soil was sheared to 10% shear strain with F_{su} at its default value of 1.0. Values of F_{su} = 0.8, 0.5, and 0.2 were specified at that point, after which undrained shearing continued to 20% shear strain. The responses show that once F_{su} has been specified, the soil strain-softened toward its new critical state undrained strength.

Undrained cyclic loading

The undrained cyclic loading responses for $s_{u,cs,eq}/\sigma'_{vc}$ of 0.25, 0.50, and 0.75 are shown in Figures 4.5-4.7, respectively. These figures show the stress-strain and stress-path responses for undrained uniform cyclic loading in DSS with a vertical consolidation stress of 1 atm, initial K_o values listed in Table 4.4, and initial static shear stress ratios (α) of 0.0, 0.1, and 0.2.

The stress-strain responses for α = 0.0 illustrate the model's ability to progressively reach larger and larger shear strains with continued cyclic loading, rather than locking up in a repeating loop as many plasticity models do. The ability to simulate the progressive accumulation of shear strains reflects the inclusion of the cumulative fabric terms, as described previously. The limiting excess pore pressure ratios (r_u) were about 88, 75, and 60% for $s_{u,cs,eq}/\sigma'_{vc}$ = 0.25, 0.50, and 0.75, respectively. The rates at which peak shear strains increase after the soil reaches a limiting r_u value decrease with increasing $s_{u,cs,eq}/\sigma'_{vc}$ and are realistic in magnitude.

The stress-strain responses with nonzero initial static shear stresses show a progressive accumulation of shear strains in the direction of the initial static shear stress, with the rate and nature of the stress-strain response also being realistic for the imposed loading.

CRR versus number of loading cycles – Effect of strength ratio and consolidation stress

The cyclic stress ratio (CSR) required to cause single-amplitude shear strains of 3% are plotted versus number of uniform loading cycles in Figure 4.8 for $s_{u,cs,eq}/\sigma'_{vc}$ = 0.25, 0.5, and 0.75 under vertical consolidation stresses of 1, 4, and 8 atm. These results are for DSS loading with the initial K_o values from Table 4.4 and zero initial static shear stress ratio (α=0.0). The cyclic resistance ratios (CRR) for small numbers of loading cycles (close to one cycle) are close to the $s_{u,cs,eq}/\sigma'_{vc}$ values, as expected.

The slopes of these CRR versus number of loading cycle curves are in reasonable agreement with typical values obtained in laboratory testing studies. If the numerical results are fitted with a power law, the exponent b is generally between 0.14 and 0.20 for these simulations, which is reasonably consistent with experimental observations for low-plasticity silts and clays (e.g., Figure 1.6). The slopes of the CRR versus number of loading cycles curves is most strongly affected by the parameters h_{po}, z_{max}, c_ε, and c_z, whereas that the cyclic strength at ½ cycle is essentially controlled by model's undrained strength ratio.

The effect of overburden stress on CRR is negligible for $s_{u,cs,eq}/\sigma'_{vc}$ = 0.25, but become more significant as $s_{u,cs,eq}/\sigma'_{vc}$ increases. The effect of overburden stress on the CRR is relatively small because the effects of overburden stress on soil strength are already accounted for in the specification of $s_{u,cs,eq}/\sigma'_{vc}$.

CRR versus number of loading cycles – Effect of initial static shear stress

The cyclic stress ratio (CSR) required to cause single-amplitude shear strains of 3% are plotted versus number of uniform loading cycles in Figure 4.9 for $s_{u,cs,eq}/\sigma'_{vc}$ = 0.25, 0.5, and 0.75 with initial static shear stress ratios (α) of 0.0, 0.1, and 0.2. These results are for DSS loading with the initial K_o values listed in Table 4.4 and vertical consolidation stress of 1 atm. The cyclic resistance ratios (CRR) decrease with increasing α by amounts that are reasonably consistent with experimental trends (Figures 1.8 and 1.9).

Strain-controlled loading for G/G_{max} and damping values

Undrained strain-controlled cyclic loading in DSS for $s_{u,cs,eq}/\sigma'_{vc}$ = 0.25, 0.50, and 0.75 under vertical consolidation stresses of 1 and 4 atm with K_o=1.0 are shown in Figures 4.10, 4.11, and 4.12, respectively, with results also shown for the equivalent modulus reduction (G/G_{max}) and equivalent damping ratio (ξ) versus cyclic shear strain amplitude (γ). These simulations use K_o = 1.0 for all strength ratios since common empirical correlations for dynamic properties rely on data for isotropically consolidated test conditions. Also shown on these figures are the modulus reduction and equivalent damping ratio curves recommended for clays of low PI by Vucetic and Dobry (1991). The simulated modulus reduction and equivalent damping ratio curves show a modest dependence on effective confining stress, which is consistent with expectations given that n_G is less than unity. Note that setting n_G = 1.0 eliminates any dependence of the G/G_{max} and equivalent damping ratio curves on consolidation stress. The simulated modulus reduction curves for this calibration generally fall between the empirical PI = 0 and PI = 10 curves by Vucetic and Dobry (1991), whereas the simulated damping ratios are slightly greater than the corresponding empirical curves.

The influence of G_o and h_o on the modulus reduction and damping responses are illustrated for $s_{u,cs,eq}/\sigma'_{vc}$ = 0.50 in Figure 4.13. Increasing G_o, while keeping h_o constant, shifts the shear modulus reduction curve to the left and increases the equivalent damping values for a given shear strain amplitude. Increasing h_o, while keeping G_o constant, shifts the shear modulus reduction curve to the right and lowers the equivalent damping values for a given shear strain amplitude. In calibration, the value of G_o should be set first based on the estimated V_s, followed by adjustment of h_o based on the target modulus reduction and damping responses.

Drained monotonic loading

The response for drained monotonic loading in direct simple shear (DSS) for soil with $s_{u,cs,eq}/\sigma'_{vc}$ = 0.25, 0.50, and 0.75 under vertical confining stresses of ¼, 1, 2, 4, and 16 atm is shown in Figure 4.14. The plots show the response up to shear strains of 20%, while the simulations tend to approach critical state conditions at shear strains ranging from 50-70% for $s_{u,cs,eq}/\sigma'_{vc}$ = 0.75 to as large as 150-200% for $s_{u,cs,eq}/\sigma'_{vc}$ = 0.25. The simulated response for $s_{u,cs,eq}/\sigma'_{vc}$ = 0.25 is strain-hardening, as expected for an initially loose-of-critical soil. The simulated response for $s_{u,cs,eq}/\sigma'_{vc}$ = 0.75 is slightly post-peak strain-softening, as expected for an initially dense-of-critical soil The rates of strain-softening and strain-hardening appear slower than often observed in experimental results, which partly reflects the calibration parameters and partly reflects limitations in single element simulations. The strain hardening rate for the $s_{u,cs,eq}/\sigma'_{vc}$ = 0.25 case can be increased by

adjusting the secondary input parameters, if drained strengths are a primary concern for the calibration. The strain softening rate for the $s_{u,cs,eq}/\sigma'_{vc}$ = 0.75 case can also be adjusted, but calibrations for strain softening in dilating soils are complicated strain localizations in laboratory tests, which is something that single element simulations cannot reproduce accurately.

The effects of $n^{b,wet}$ on the drained monotonic loading response for $s_{u,cs,eq}/\sigma'_{vc}$ = 0.25 and σ'_{vc} = ¼, 1, 2, 4, and 16 atm are shown in Figure 4.15. Reducing $n^{b,wet}$ from the default value of 0.8 results in the drained shear resistance increasing more quickly toward critical state values with increasing shear strain.

Post-cyclic-loading reconsolidation strains

Volumetric strains due to post-cyclic-loading reconsolidation, with and without the PostShake option, are plotted in Figure 4.16 versus the maximum shear strain induced during undrained cyclic loading. Results are shown for $s_{u,cs,eq}/\sigma'_{vc}$ = 0.25 loaded in DSS with an initial K_o=0.5, a vertical consolidation stress of 1 atm, zero initial static shear stress ratio, and a cyclic stress ratio of 0.20. After cyclic loading to different maximum shear strains, the shear strain was returned to zero and then the specimen one-dimensionally reconsolidated to its original vertical consolidation stress. The computed volumetric strains were less than about 0.3% with PostShake = 0 (default value) and are smaller than expected based on common experimental data. The computed volumetric strains with PostShake = 1 (imposed at the end of cyclic loading) increased to values ranging from 0.5% to 1.2% as the parameter CGC was increased from 1.0 to 5.0.

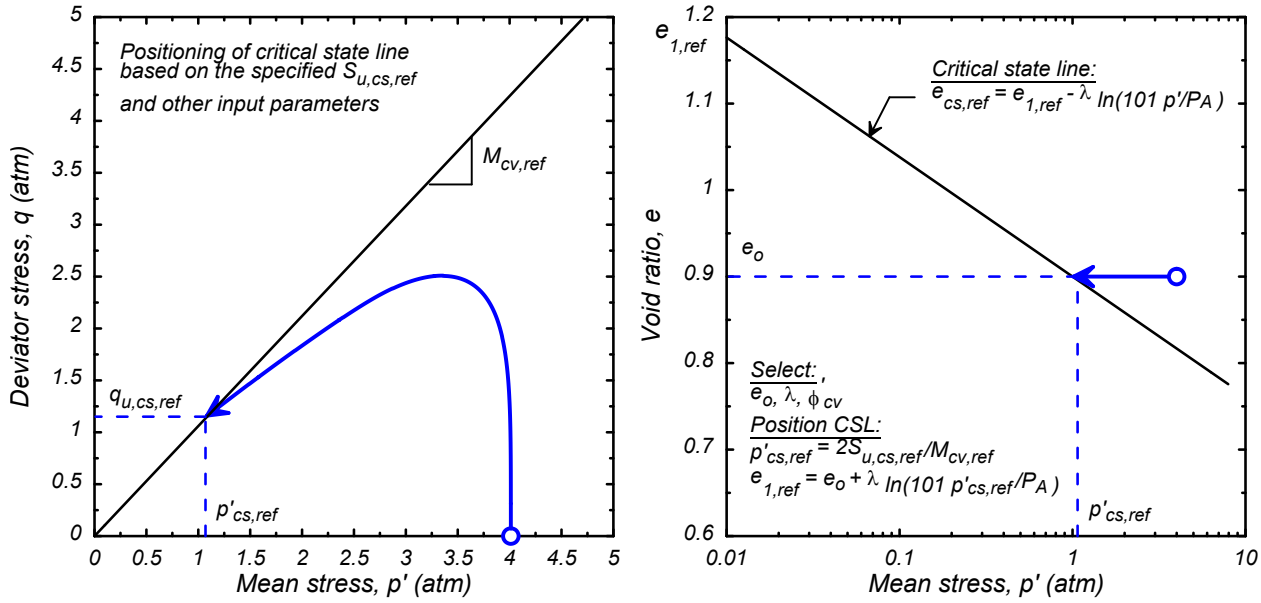

Figure 4.1. Positioning the critical state line based on the specified undrained shear strength and other input parameters.

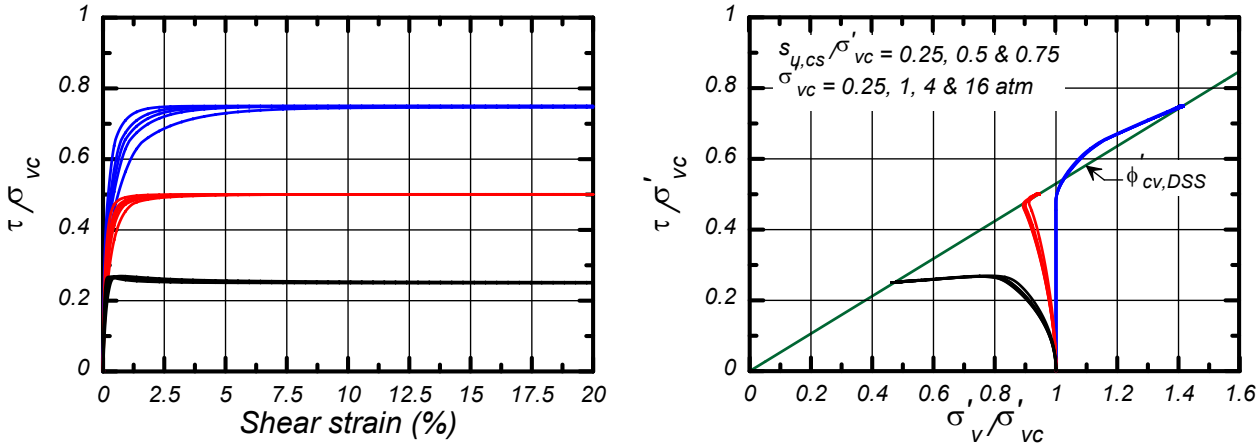

Figure 4.2. Normalized responses in undrained monotonic DSS loading for baseline parameters.

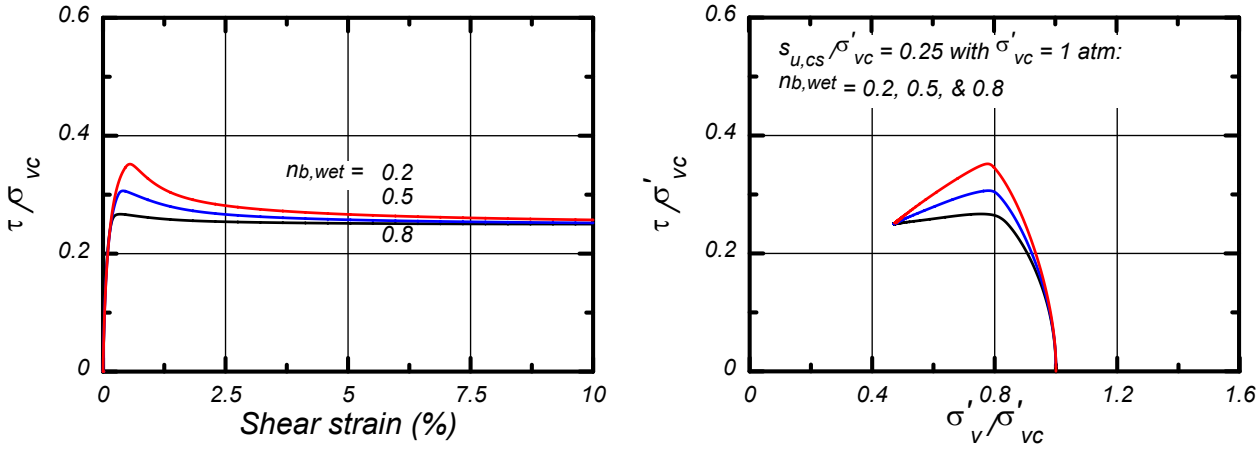

Figure 4.3. Effect of $n^{b,wet}$ on responses to undrained monotonic DSS loading for $s_{u,cs}/\sigma'_{vc} = 0.25$.

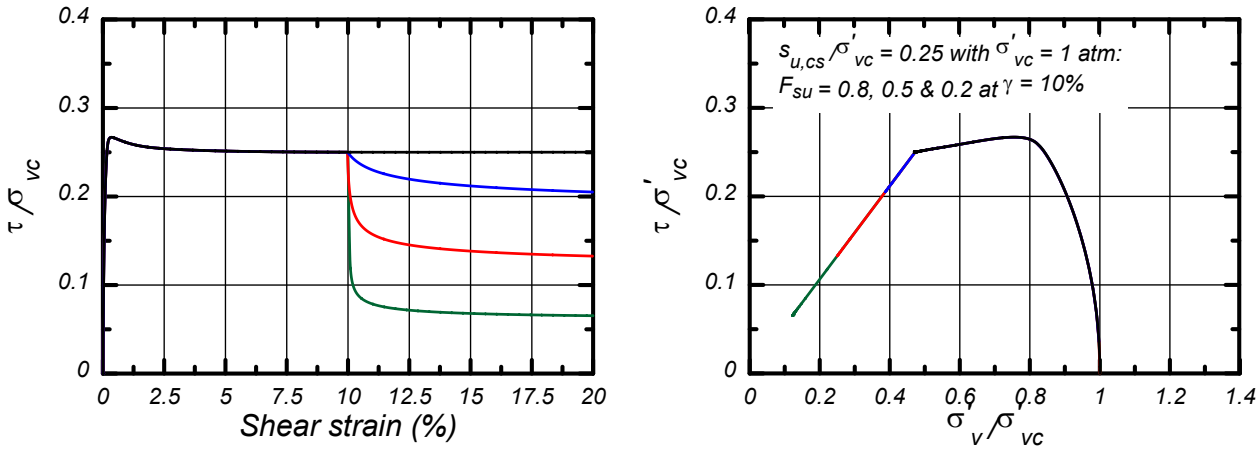

Figure 4.4. Effect of F_{su} on response to undrained monotonic DSS loading for $s_{u,cs}/\sigma'_{vc} = 0.25$.

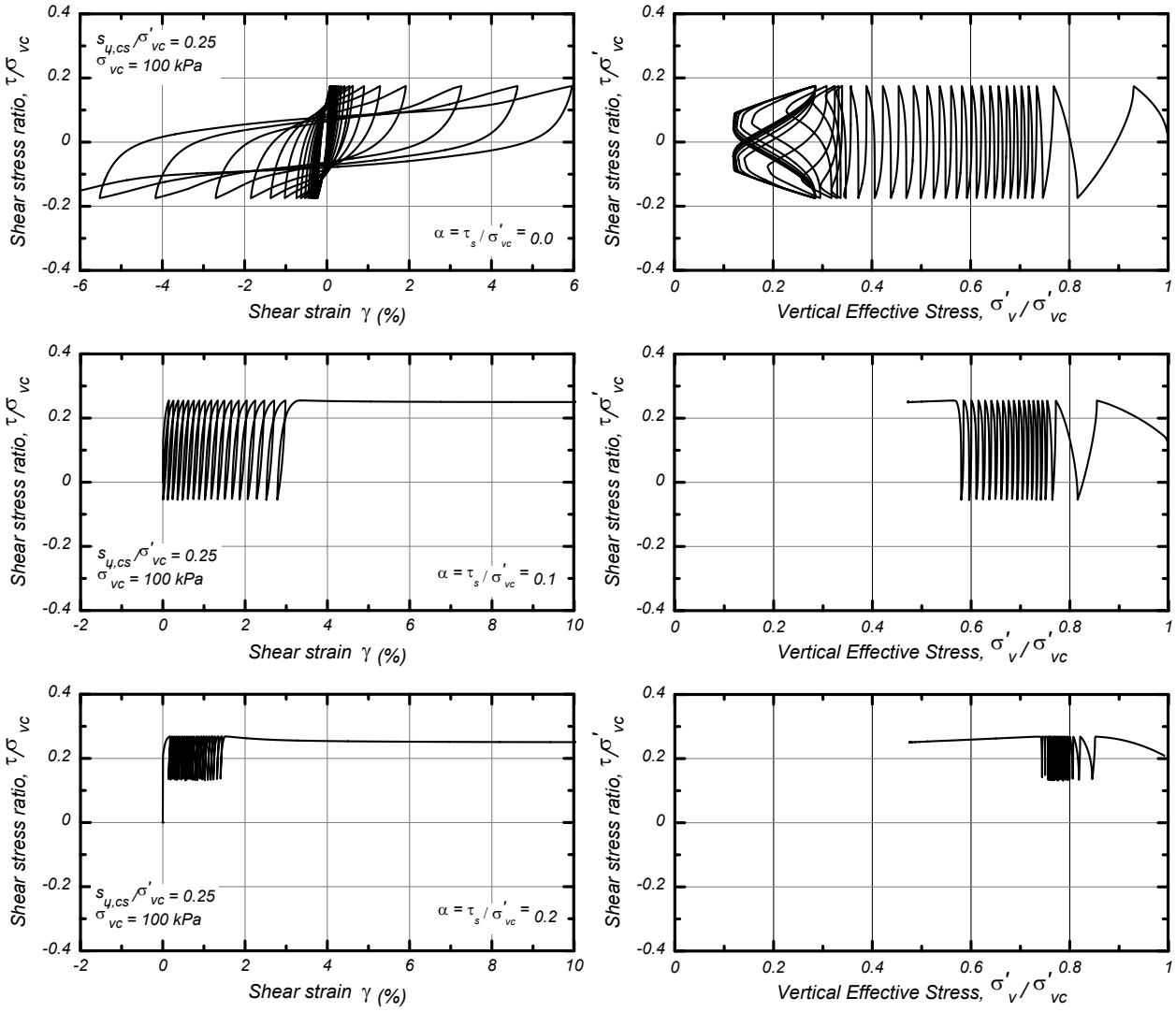

Figure 4.5. Stress-strain and stress path responses for undrained cyclic DSS loading for baseline parameters with $s_{u,cs}/\sigma'_{vc} = 0.25$ and initial static shear stress ratios of 0.0, 0.1, and 0.2.

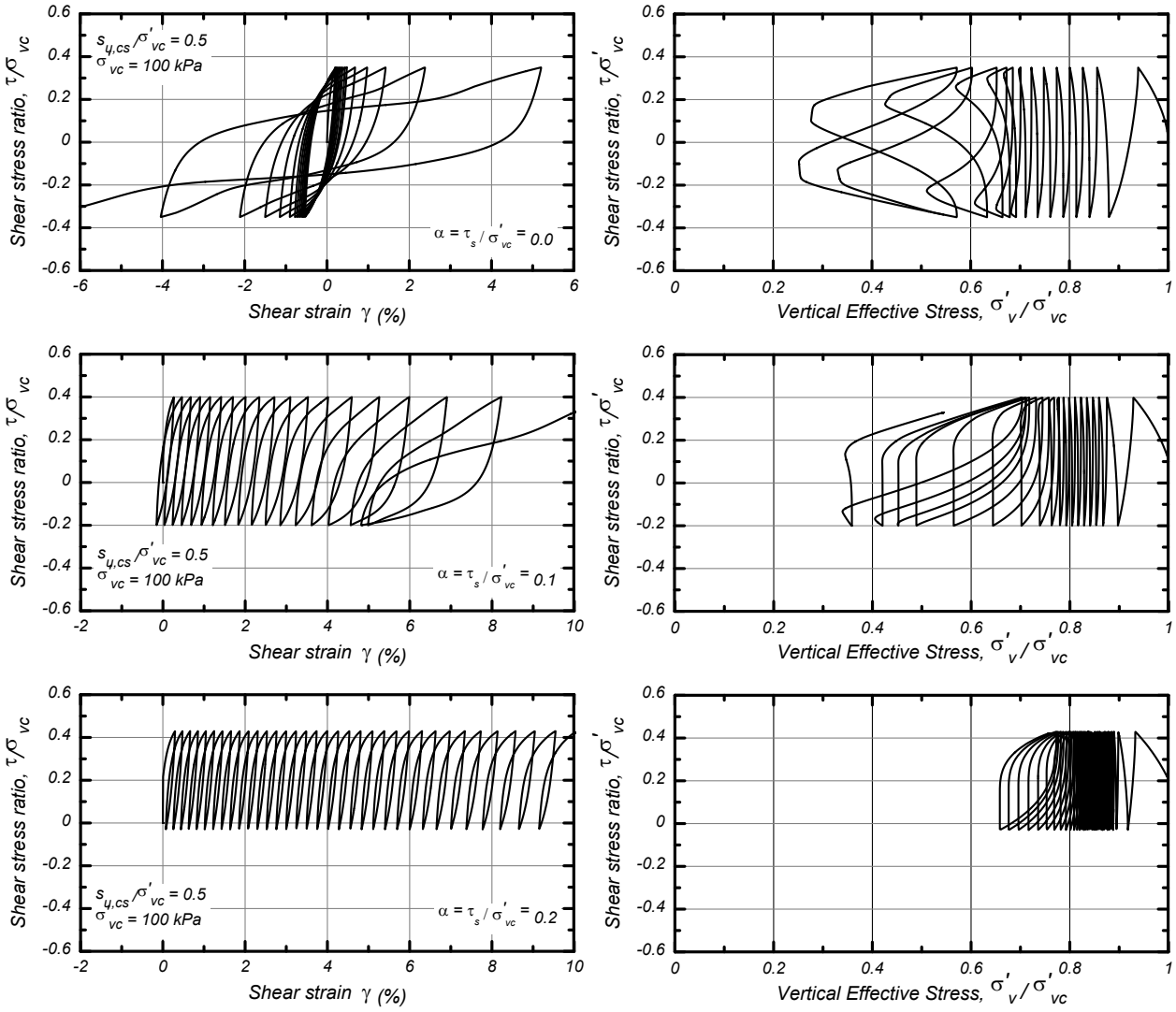

Figure 4.6. Stress-strain and stress path responses for undrained cyclic DSS loading for baseline parameters with $s_{u,cs}/\sigma'_{vc} = 0.50$ and initial static shear stress ratios of 0.0, 0.1, and 0.2.

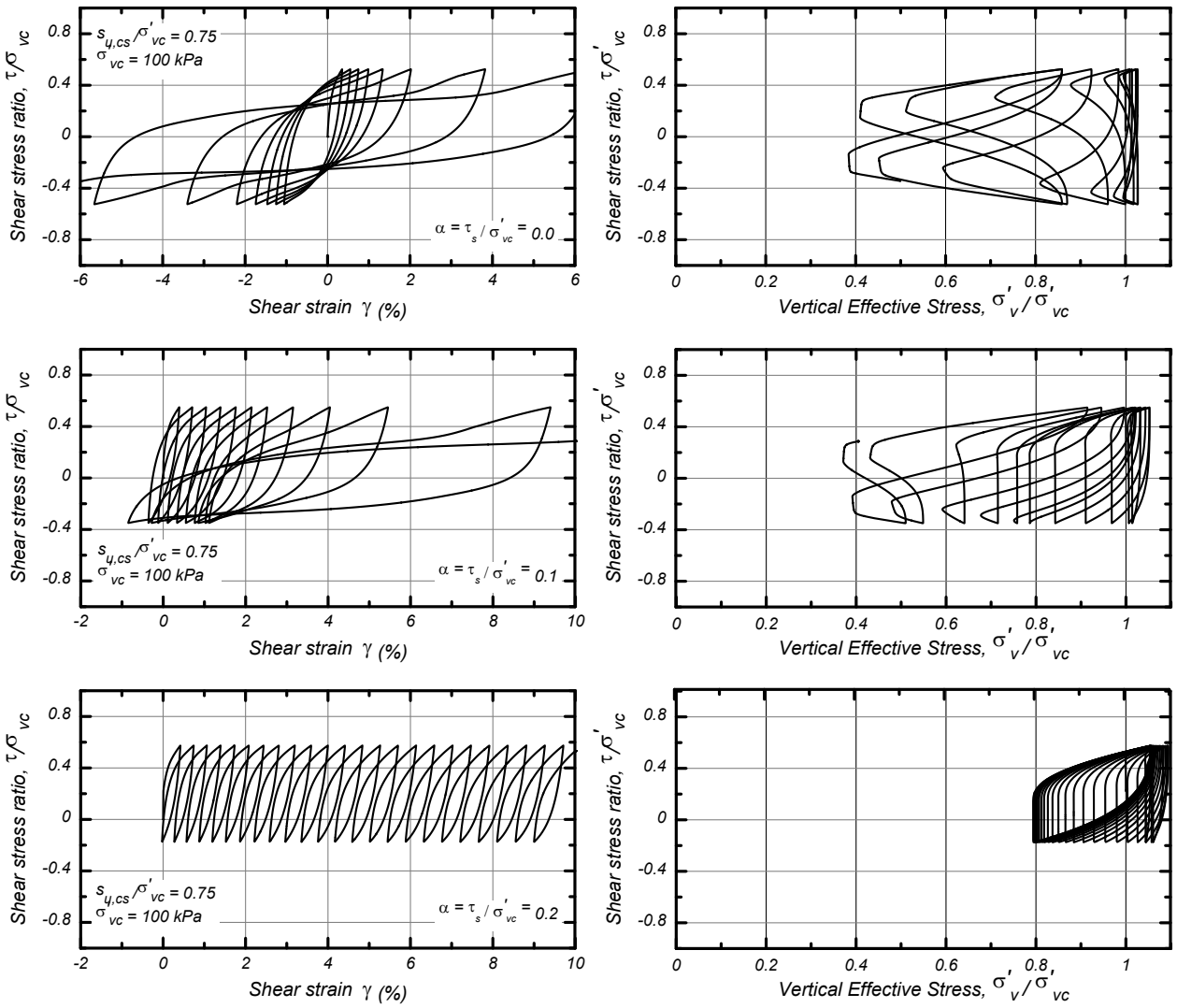

Figure 4.7. Stress-strain and stress path responses for undrained cyclic DSS loading for baseline parameters with $s_{u,cs}/\sigma'_{vc} = 0.75$ and initial static shear stress ratios of 0.0, 0.1, and 0.2.

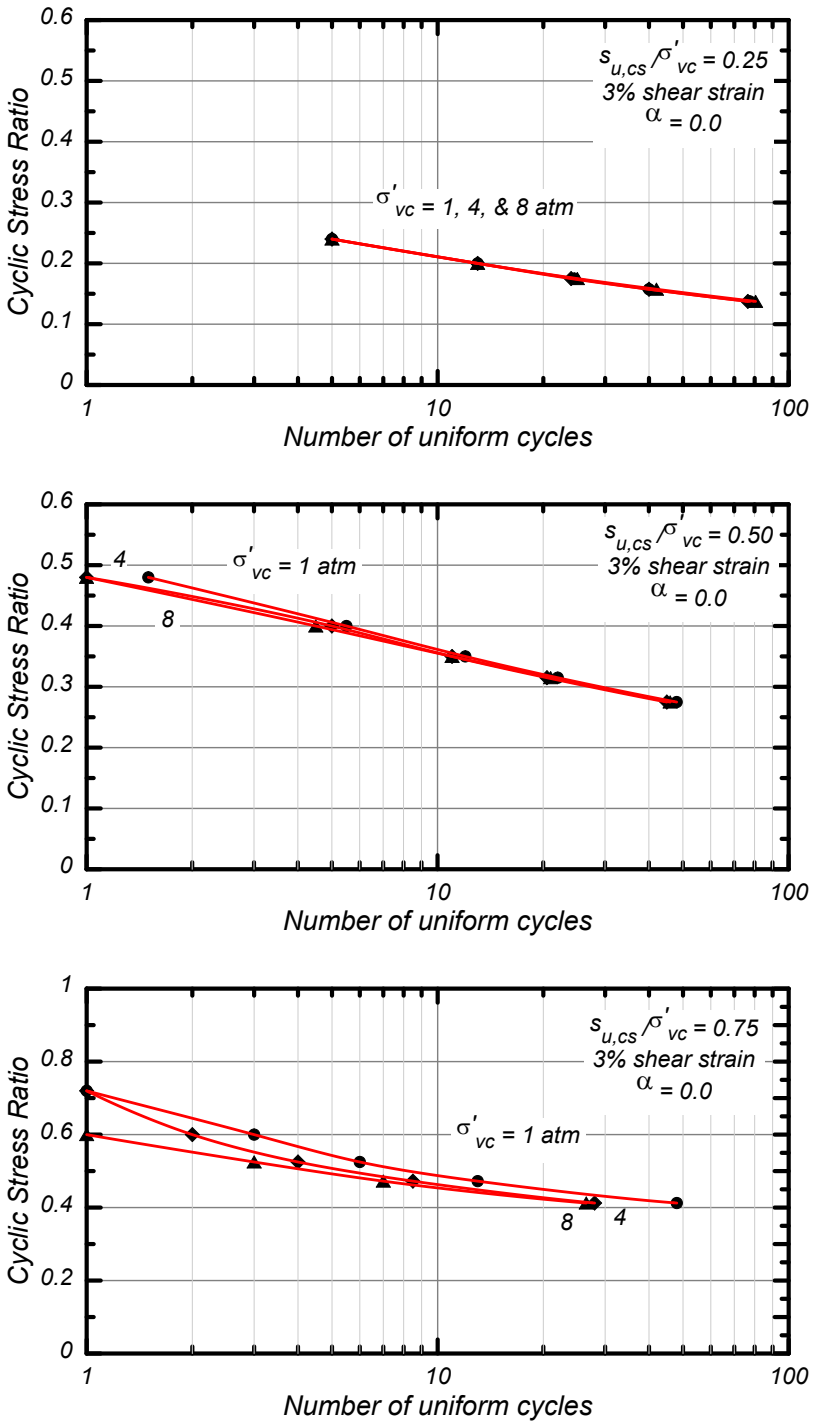

Figure 4.8. Cyclic stress ratio versus number of equivalent uniform loading cycles to cause a peak shear strain of 3% in undrained cyclic DSS loading for baseline parameters with $s_{u,cs}/\sigma'_{vc}$ = 0.25, 0.50, and 0.75 and vertical consolidation stresses of 1, 4, and 8 atm.

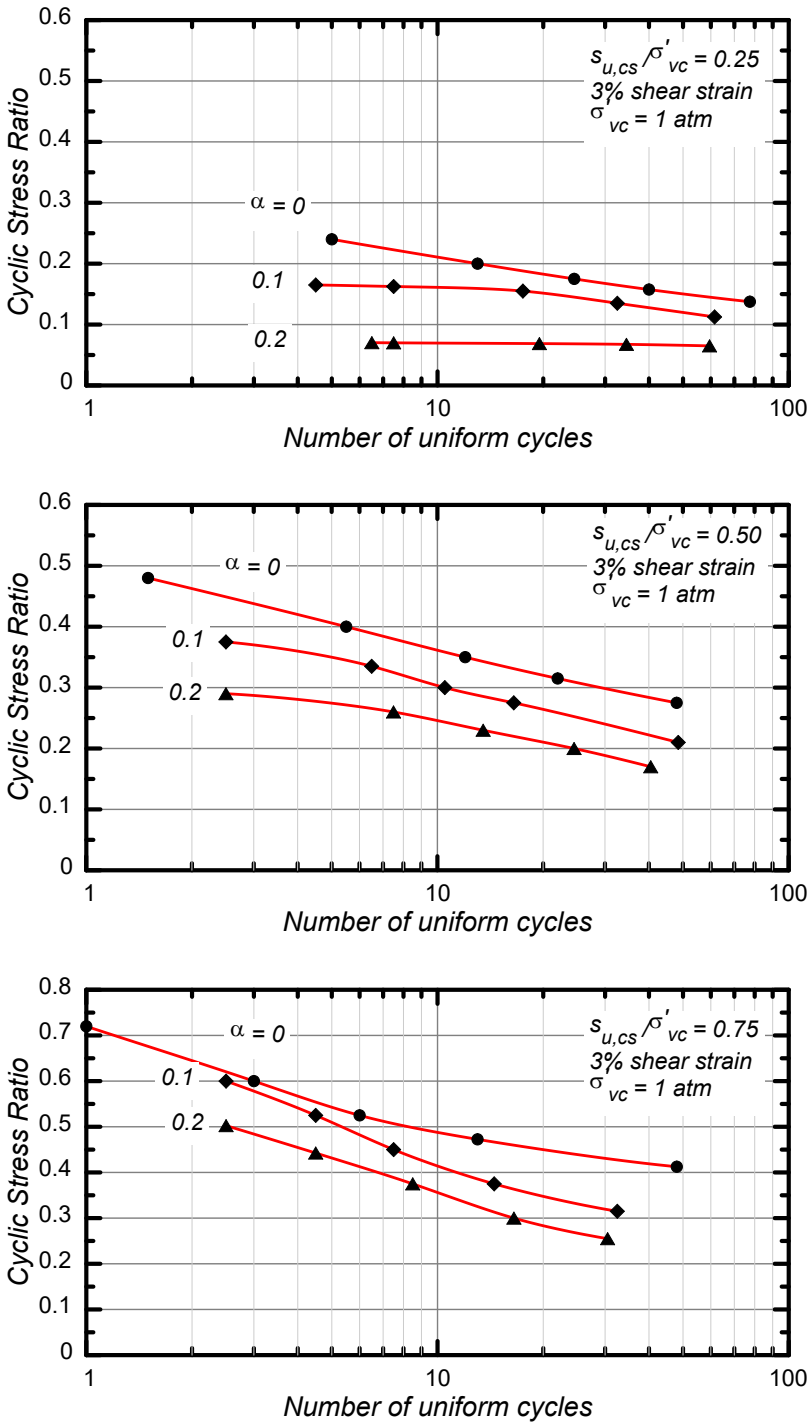

Figure 4.9. Cyclic stress ratio versus number of equivalent uniform loading cycles to cause a peak shear strain of 3% in undrained cyclic DSS loading for baseline parameters with $s_{u,cs}/\sigma'_{vc}$ = 0.25, 0.50, and 0.75 and initial static shear stress ratios of 0.0, 0.2, and 0.3.

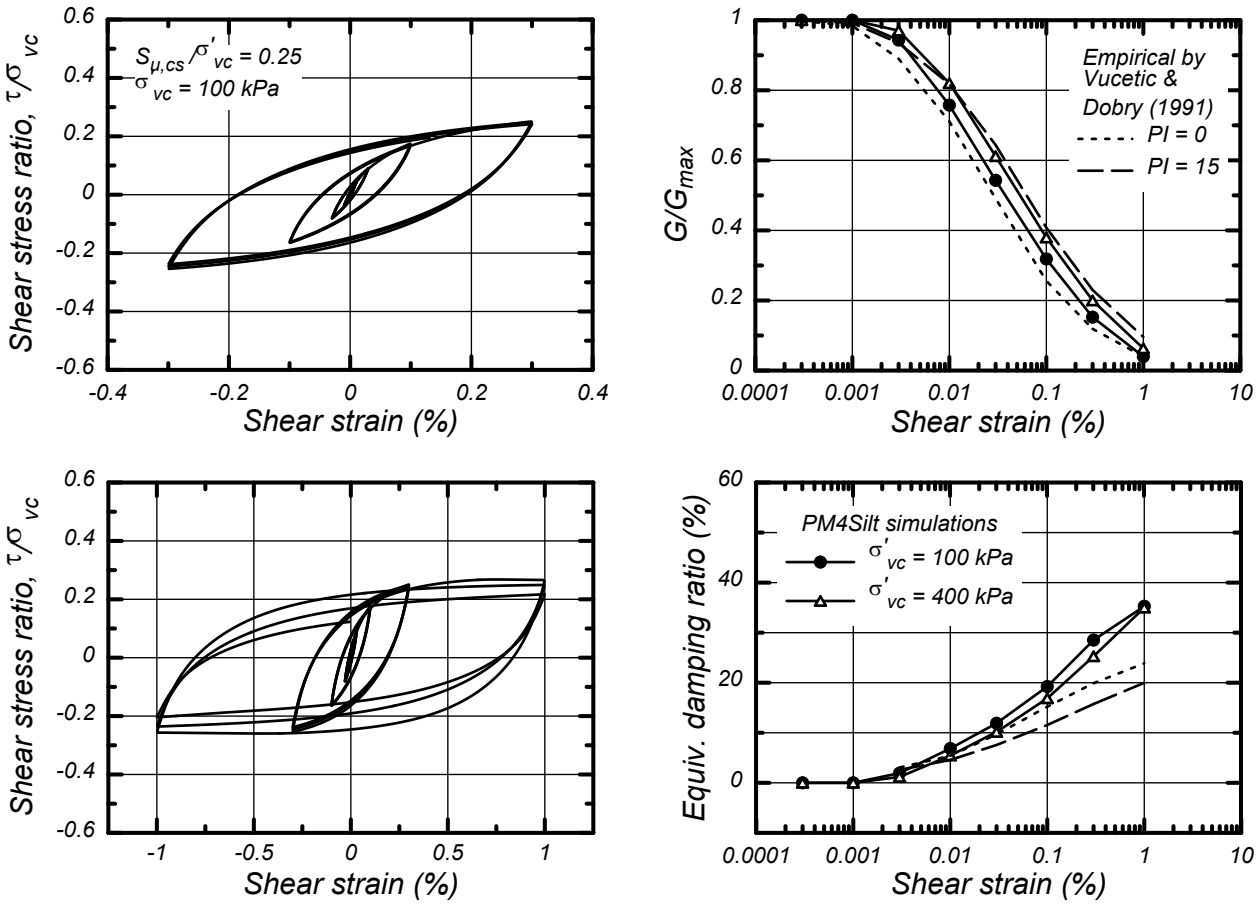

Figure 4.10. Shear modulus reduction and equivalent damping ratios from undrained strain-controlled cyclic DSS loading for baseline parameters with $s_{u,cs}/\sigma'_{vc} = 0.25$.

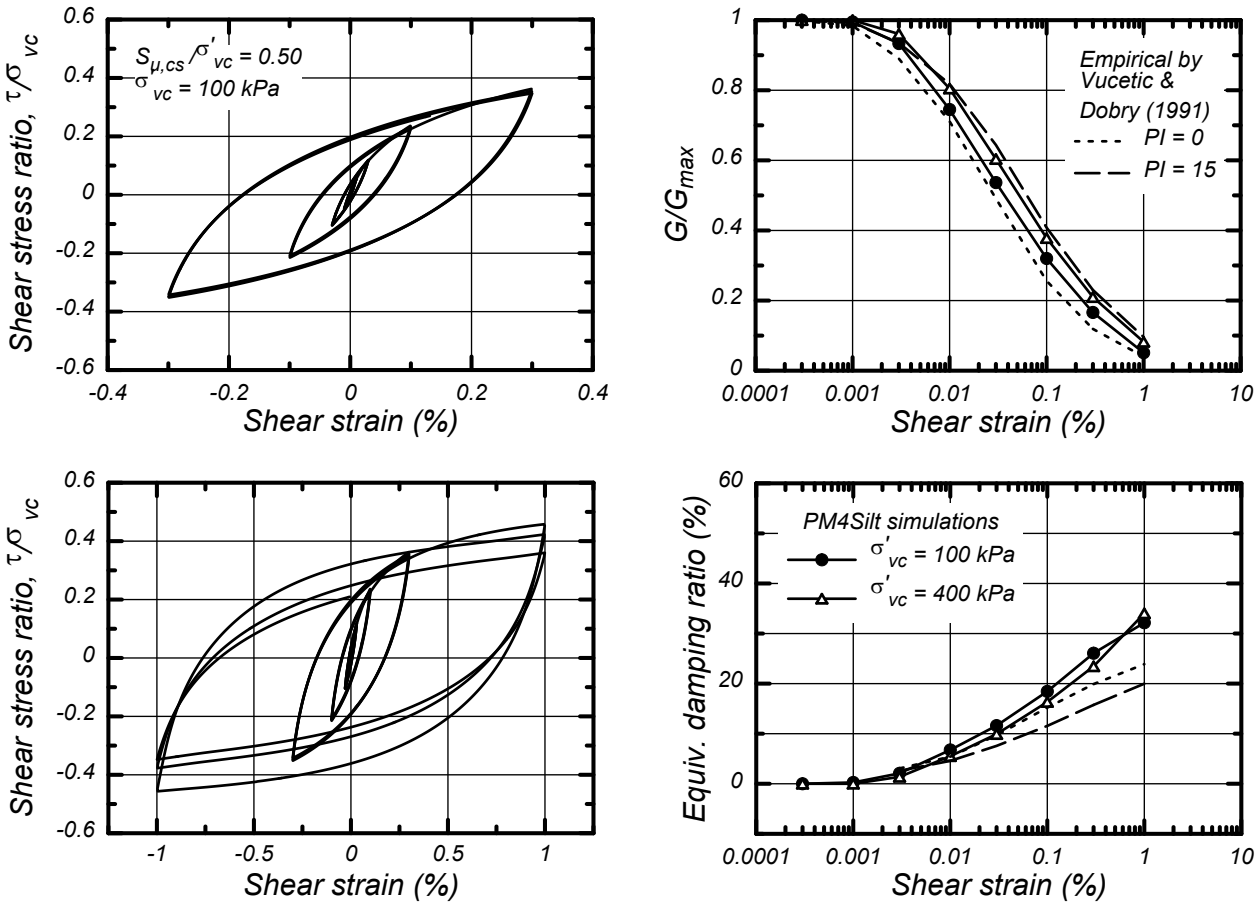

Figure 4.11. Shear modulus reduction and equivalent damping ratios from undrained strain-controlled cyclic DSS loading for baseline parameters with $s_{u,cs}/\sigma'_{vc} = 0.50$.

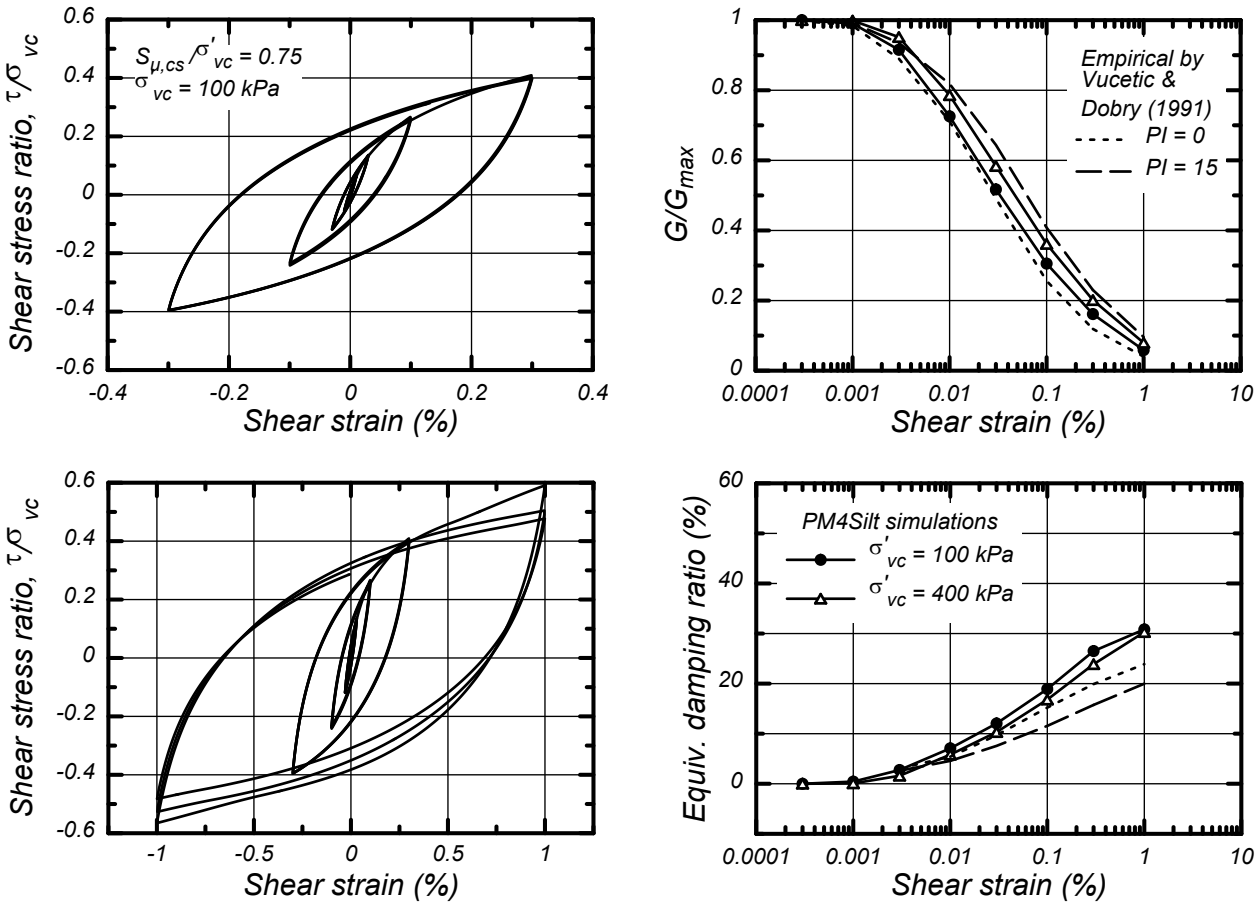

Figure 4.12. Shear modulus reduction and equivalent damping ratios from undrained strain-controlled cyclic DSS loading for baseline parameters with $s_{u,cs}/\sigma'_{vc} = 0.75$.

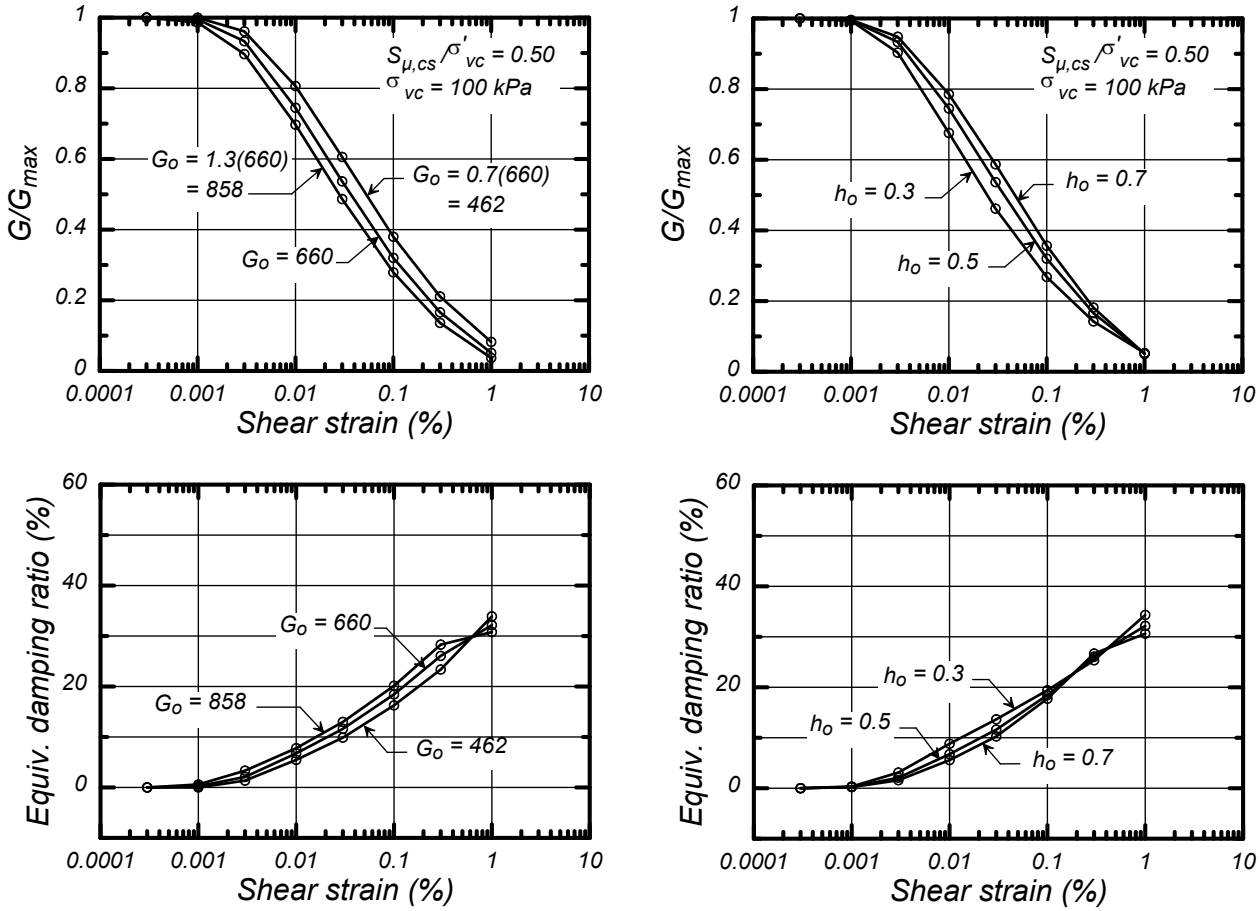

Figure 4.13. Effect of G_o and h_o on the shear modulus reduction and equivalent damping ratios from undrained strain-controlled cyclic DSS loading for baseline parameters with $s_{u,cs}/\sigma'_{vc}$ = 0.50.

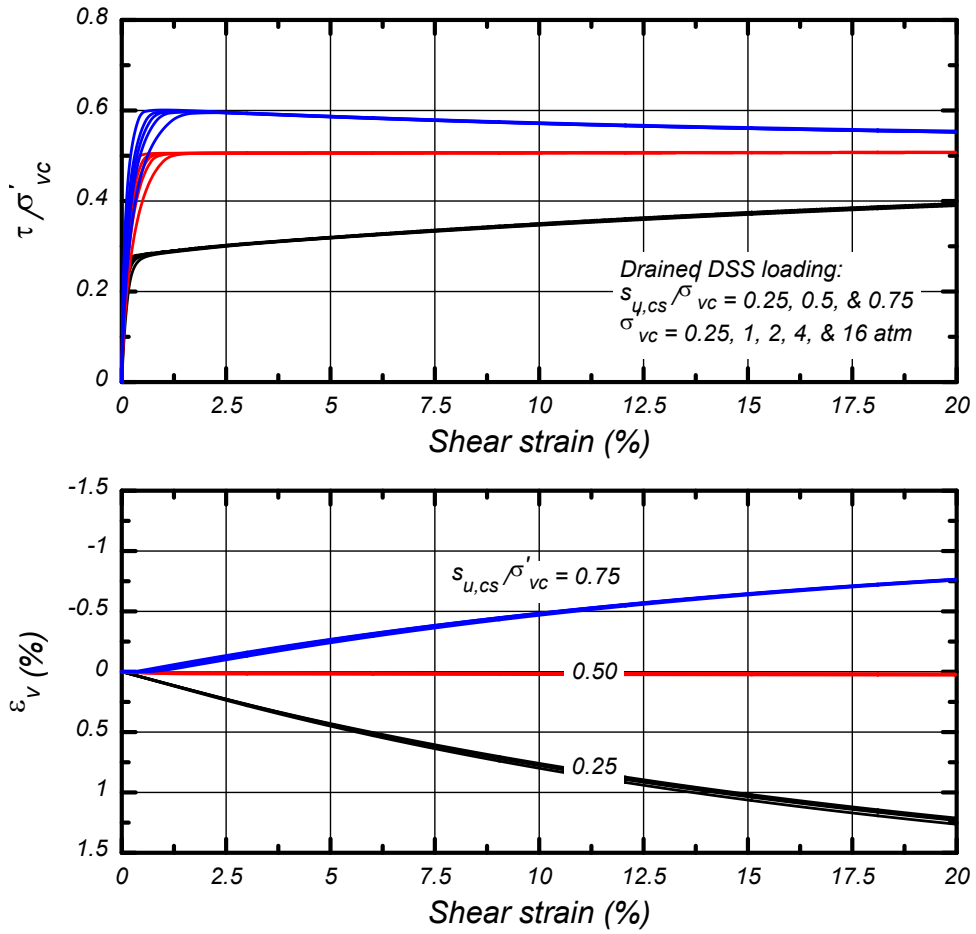

Figure 4.14. Normalized responses in drained monotonic DSS loading for baseline parameters.

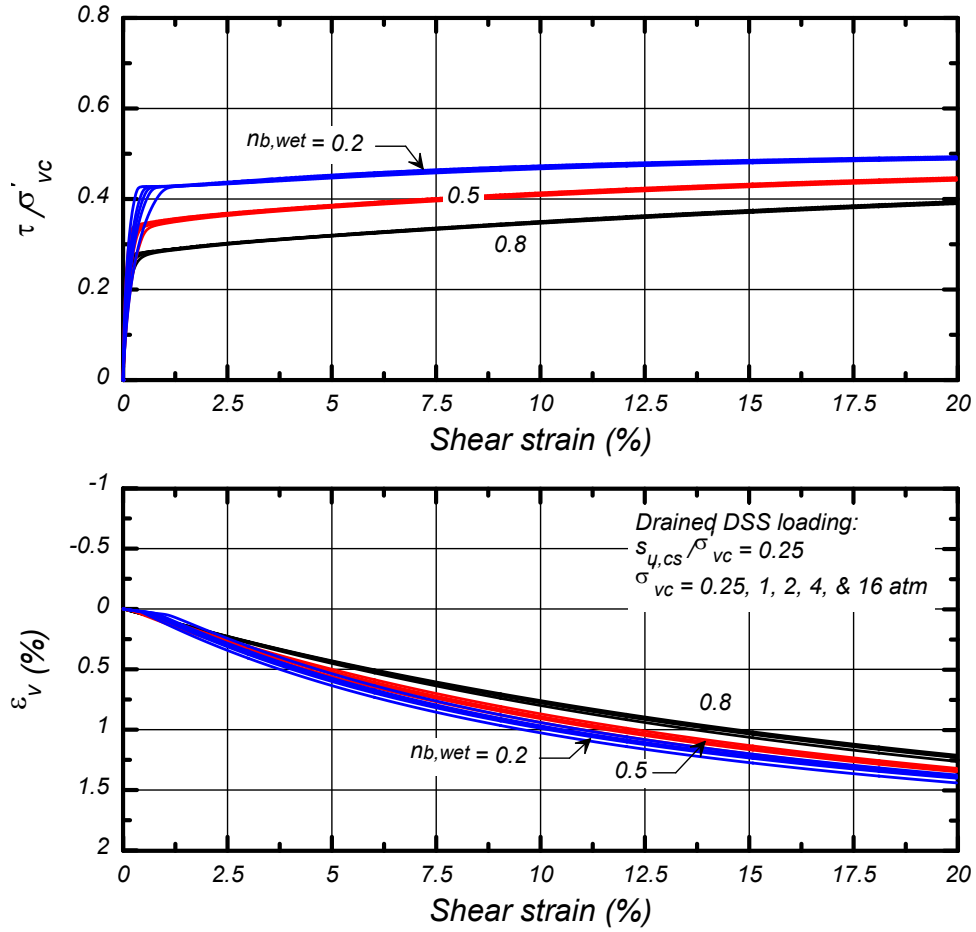

Figure 4.15. Normalized responses in drained monotonic DSS loading for $s_{u,cs}/\sigma'_{vc} = 0.25$ with three values for $n^{b,wet}$.

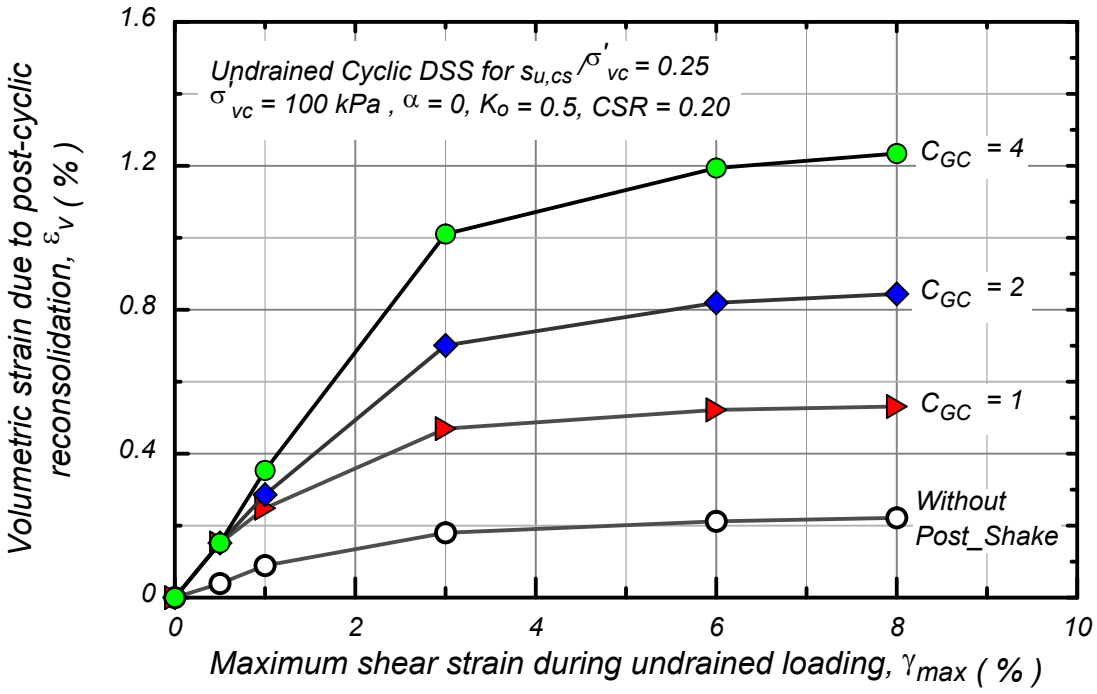

Figure 4.16. Volumetric strains due to post-cyclic, one-dimensional reconsolidation after undrained cyclic DSS loading to different maximum shear strains for baseline parameters with s_u/σ'_{vc} = 0.25.

5. CALIBRATION AND CALIBRATION EXAMPLES

The approach used to calibrate PM4Silt will depend on the available site characterization and laboratory testing data, as well as on the nature of the system being analyzed. The calibration processes and examples presented in this section are intended only as examples, recognizing that alternative approaches will be more appropriate in other situations.

A set of FLAC project files for calibrating PM4Silt using single element simulations are provided at https://pm4silt.engr.ucdavis.edu/. These example "drivers" include files for simulating monotonic DSS loading, cyclic DSS loading with uniform cyclic stress ratios, and cyclic DSS loading at different cyclic strain amplitudes to obtain secant shear moduli and equivalent damping ratios. Each driver loads five single elements with some variation in loading condition, and can be run drained or undrained. Drivers for other loading conditions, such as irregular loading sequences or post-cyclic reconsolidation, can be developed using these examples as guides.

5.1 Calibration with minimum required information

The minimum required information for calibration of PM4Silt corresponds to the primary input parameters plus the determination that the soil is expected to exhibit cyclic loading behaviors associated with plastic silts and clays and not those of purely nonplastic silts or sands. The corresponding calibration process can be summarized as follows.

[1] Select the undrained shear strength ($s_{u,cs,eq}$) or undrained shear strength ratio ($s_{u,cs,eq}/\sigma'_{vc}$) for critical state conditions (i.e., large strains) and earthquake loading rates.

[2] Select the shear modulus coefficient (G_o) to match the small-strain shear modulus (G_{max}) obtained from estimated or measured shear wave velocities.

[3] Simulate the undrained monotonic loading response. If the soil is initially loose of critical state, use $n^{b,wet}$ to adjust the peak $s_{u,eq}$ as desired.

[4] Simulate undrained cyclic loading with uniform cyclic stress ratios and iteratively adjust the contraction rate parameter (h_{po}) to obtain a reasonable slope for the simulated CRR versus number of uniform loading cycles to cause a peak shear strain of 3%. Referring to the laboratory test data compiled in Figure 1.6, a peak shear strain of 3% might reasonably be caused by 10-30 uniform loading cycles at a CSR = 0.7 $s_{u,eq}/\sigma'_{vc}$ or 30-100 uniform loading cycles at a CSR = 0.55 $s_{u,eq}/\sigma'_{vc}$.

[5] Simulate undrained cyclic loading at different strain amplitudes to confirm and document that the resulting secant shear moduli and equivalent damping ratios are reasonable. If desired, the parameter h_o can be iteratively adjusted to improve the fit with an empirical shear modulus and damping ratio correlation (e.g., Figure 1.10).

[6] Repeat steps [3] through [6] if necessary, until no further revisions to model parameters are warranted.

The above calibration process requires few, if any, iterations because only the primary parameters are being adjusted in most cases.

Model responses should be examined for any other loading paths that are expected to be important to the system level response. For example, it would be appropriate to plot the stress-strain responses for cyclic loading with a range of initial static shear stress ratios, if the system being examined involves sloping ground (e.g., an embankment or levee).

Model responses obtained using the above calibration process should be similar to those illustrated in the previous section if the primary input parameters are not greatly outside the range of values used in those examples. Nonetheless, variations in material specific values for $s_{u,cs,eq}/\sigma'_{vc}$, G_o, and h_{po} will affect certain details of behavior and thus the behaviors should always be checked and evaluated for reasonableness.

5.2 Calibration with monotonic and cyclic laboratory test data

Calibrations for two low-plasticity fine-grained soils are presented in this section. The two soils – a silty clay and a clayey silt – exhibit significantly different cyclic loading behaviors. Calibrations using PM4Silt Version 1 were presented in Boulanger et al. (2018) and the Version 1 manual. These calibrations are updated herein using PM4Silt Version 2.1 with the same general calibration process.

These two materials were reconstituted mixtures of silica silt and kaolin and had plasticity indices (PIs) of 6 and 20. Undrained monotonic and undrained cyclic direct simple shear (DSS) tests were performed on normally consolidated, slurry deposited specimens. Test results are presented for specimens consolidated to an initial vertical effective stress (σ'_{vc}) of 100 kPa. Monotonic and cyclic tests were generally performed at the same strain rate of 5%/hr, so no adjustment for strain rate effects was necessary between these two test types. Additional details regarding laboratory tests on these materials are provide in Price et al. (2015, 2017).

The purpose of the following calibrations is to illustrate the ability of the PM4Silt model to approximate a range of monotonic and cyclic loading behaviors, and thus the emphasis is on approximating the specific laboratory test results. In practice, laboratory measured strengths may be adjusted to account for different loading conditions in the field, including multidirectional shaking and higher strain rates. In those situations, model simulations cannot be directly compared to individual cyclic test results, but rather are compared with allowance for the above adjustments. Such adjustments are not included in the following examples.

Calibration of PM4Silt for a PI = 20 silty clay

The first soil examined herein is a normally consolidated, silty clay with a PI of 20, liquid limit (LL) of 42, and USCS classification of CL. This soil was manufactured by mixing 70% kaolin with 30% silica silt by dry mass (Price et al. 2015, 2017).

The calibration process followed the sequence of steps summarized below. These steps are similar to those described in the previous section, but involve a greater number of iterations because several secondary parameters were adjusted.

[1] Select values for the primary input parameters $s_{u,cs,eq}$ (or $s_{u,cs,eq}/\sigma'_{vc}$) and G_o.

[2] Select values for any secondary parameters that can be informed by soil-specific test data, such as n_G, e_o, λ, and ϕ'_{cv}.
[3] Simulate the undrained monotonic loading response and use $n^{b,wet}$ to adjust the peak s_u if the soil is initially wet of critical.
[4] Simulate undrained cyclic loading at different strain amplitudes and use h_o to adjust, as desired, the dependence of secant shear moduli and equivalent damping ratios on cyclic shear strain amplitude.
[5] Simulate undrained cyclic loading with uniform cyclic stress ratios and use h_{po} to adjust the fit to the cyclic DSS data for CRR versus number of uniform loading cycles to cause a peak shear strain of 3%.
[6] Examine the stress-strain and stress-path responses of the above cyclic loading simulations, and use other secondary parameters such as c_z, c_ε, and $r_{up,max}$ to adjust the shear strain accumulation rate and other features of behavior, and
[7] Repeat steps [3] through [6] until no further revisions to input parameters are warranted.

The input parameters obtained by the above process for the PI = 20 silty clay are listed in Table 1. The calibration parameter c_z was revised from that used with PM4Silt Version 1 by Boulanger et al. (2018) to maintain similar rates of shear strain accumulation with the current version. Per step [1], $s_{u,cs,eq}/\sigma'_{vc}$ was set to 0.21 based on the monotonic DSS test results presented later and G_o was set to 345 based on the empirical correlation by Carlton and Pestana (2012), which results in an implied V_s of 120 m/s at σ'_{vc} = 1 atm. Per step [2], e_o was set to 1.0, λ to 0.18, and ϕ'_{cv} to 25° based on the responses of the DSS specimens during consolidation and shearing. Additional comments on the calibration process are provided with the following comparisons of simulated and measured or target responses.

Measured and simulated responses in monotonic undrained DSS loading are compared in Figure 5.1. The simulated and measured shear strengths at critical state are the same, which reflects the fact that $s_{u,cs,eq}$ is an input parameter. The parameter $n^{b,wet}$ was set to 1.0 because this limits the peak shear resistance to $s_{u,cs,eq}$ in the simulation, which matches the strain-hardening response observed in the test. The stress-strain response is initially much stiffer in the simulation than in the test, but this reflects the decision to base G_o and the target G/G_{max} behavior on empirical correlations, rather than attempting to match the measured DSS loading response. The stress-strain response measured in DSS tests is known to underestimate small-strain stiffness due to various limitations with standard equipment, which means that adjusting G_o to match the measured DSS response would underestimate the true small-strain stiffness. The small-strain modulus and modulus reduction behavior are key concerns for any dynamic response analysis, so they were given priority in calibration of the model parameters.

Normalized secant shear moduli (G/G_{max}) and equivalent damping ratios from simulations of undrained cyclic DSS loading at σ'_{vc} of 100 and 400 kPa are compared to the empirical curves by Vucetic and Dobry (1991) for PI = 0 and 15 soils in Figure 5.2. The simulations have three cycles of loading at each strain amplitude, and the secant shear moduli and damping ratio from the last cycle are the values plotted in Figure 5.2. The G/G_{max} and equivalent damping ratios are close the PI = 15 curve for cyclic strain amplitudes less than about 0.03%, which was considered sufficiently reasonable to not warrant adjusting the parameter h_o. The more rapid drop in G/G_{max} and increase in damping ratios as cyclic strain amplitudes exceed about 0.1% reflect cyclic degradation for this

soft soil condition (e.g., see the stress-strain loops in the lower left plot of Figure 5.2). This deviation from the empirical curves at larger strains is considered reasonable for this soft soil condition, and thus no attempt was made to improve the fit with the empirical curves at these larger strains. The simulations show negligible effect of σ'_{vc} on G/G_{max} or equivalent damping ratios because the shear modulus exponent n_G was set equal to 1.0.

Measured and simulated cyclic stress ratios (CSRs) required to cause a peak shear strain of 3% are plotted versus number of uniform loading cycles in Figure 5.3. The simulated cyclic strength will be approximately equal to the peak $s_{u,eq}/\sigma'_{vc}$ ratio near a single loading cycle. The parameter h_{po} was then iteratively adjusted to its final value of 2.2 to bring the simulated cyclic strength curve into average agreement with the cyclic DSS test results.

Measured and simulated stress-strain and stress-path responses are compared for specimens loaded at CSR of 0.16 and 0.13 in Figures 5.4 and 5.5, respectively. The values for c_z and c_ε were reduced to 40 (compared to a default value of 100) and 0.25 (compared to a default value of 0.5), respectively. These adjustments reduced the rates of shear strain accumulation in the simulations to levels consistent with the measured responses at different loading levels. The shear modulus exponent n_G was set to 1.0 because it slightly improved (narrowed) the stress-strain hysteresis loops and is consistent with expectations for this more plastic fine-grained soil; e.g., minimal effects of σ'_{vc} on shear moduli and damping ratio values as shown in Figure 5.2. The maximum excess pore pressure ratio was about 85-86% in the simulations (i.e., minimum σ'_v/σ'_{vc} of 0.14-0.15), which is in reasonable agreement with the measured values of 80-88%. The simulated stress-strain responses are in good agreement with the measured responses for both loading levels.

Calibration of PM4Silt for a PI = 6 clayey silt

The second soil examined herein is a normally consolidated, clayey silt with a PI of 6, liquid limit (LL) of 22, and USCS classification of CL-ML. This soil was manufactured by mixing 20% kaolin with 80% silica silt by dry mass (Price et al. 2015, 2017).

The calibration process for this soil was the same as described in the previous section. The input parameters obtained for this PI = 6 clayey silt are listed in Table 1. The calibration parameters G_o and h_{po} were revised from those presented for Boulanger et al. (2018) PM4Silt Version 1. Per step [1], $s_{u,cs,eq}/\sigma'_{vc}$ was set to 0.145 based on the monotonic DSS test results presented later and G_o was set to 560 to produce an implied V_s of 150 m/s at σ'_{vc} = 1 atm, which is comparable to that for nearly NC Fraser River Silt (PI of about 4; Boulanger and Wijewickreme 2019); this G_o is smaller than the 736 used in Boulanger et al. (2018), which implied a V_s of 172 m/s at σ'_{vc} = 1 atm. Per step [2], e_o was set to 0.61, λ to 0.07, and ϕ'_{cv} to 32° based on the responses of the DSS specimens during consolidation and shearing. Additional comments on the calibration process are provided with the following comparisons of simulated and measured or target responses.

Measured and simulated responses in monotonic undrained DSS loading are compared in Figure 5.6. The simulated and measured shear strengths at critical state are the same, which again reflects the fact that $s_{u,cs,eq}$ is an input parameter. The parameter $n^{b,wet}$ was left at its default value of 0.8 because this produced a slight peak in the shear resistance, consistent with the response observed in the test. The stress-strain response is a bit stiffer in the simulation than in the test,

which again reflects the decision to base G_o and the target G/G_{max} behavior on empirical correlations, rather than attempting to match the measured monotonic DSS loading response.

Shear moduli and equivalent damping ratios from simulations of undrained cyclic DSS loading at σ'_{vc} of 100 and 400 kPa are compared to the empirical curves by Vucetic and Dobry (1991) for PI = 0 and 15 soils in Figure 5.7. The shear moduli and equivalent damping ratios are close the PI = 0 curve for cyclic strain amplitudes less than about 0.03%, which was considered sufficiently reasonable to not warrant adjusting the parameter h_o. The more rapid drop in shear moduli and increase in damping ratios as cyclic strain amplitudes exceed about 0.1% reflect cyclic degradation for this soft soil condition (e.g., stress-strain loops in the lower left plot of Figure 5.7). This deviation from the empirical curves at larger strains is again considered reasonable for this soft soil condition. The simulations show a modest increase in G/G_{max} values and decrease in equivalent damping ratios with increasing σ'_{vc}, which is consistent with experimental trends. The simulations exhibit this stress dependence because the shear modulus exponent n_G was left at its default value of 0.75.

Measured and simulated cyclic stress ratios (CSRs) required to cause a peak shear strain of 3% are plotted versus number of uniform loading cycles in Figure 5.8. The parameter h_{po} was iteratively adjusted to its final value of 4.0 to bring the simulated cyclic strength curve into average agreement with the cyclic DSS test results.

Measured and simulated stress-strain and stress-path responses are compared for specimens loaded at CSR of 0.12 and 0.10 in Figures 5.9 and 5.10, respectively. The parameter $r_{up,max}$ was set to 0.99 to enable the simulations to reach maximum excess pore pressure ratios consistent with those measured in the tests. The values for c_z and c_ε were increased to 150 (compared to a default value of 100) and 1.0 (compared to a default value of 0.5), respectively. These adjustments increased the rates of shear strain accumulation in the simulations to levels consistent with the measured responses at different loading levels. The simulated stress-strain responses are in good agreement with the measured responses for both loading levels.

Table 5.1. Example calibrations using PM4Silt Version 2.1.

Input parameter [a]	Default value	Calibrated values [c]	
		PI = 20 silty clay	PI = 6 clayey silt
$s_{u,cs}/\sigma'_{vc}$ – s_u at critical state	-- [b]	0.21	0.145
G_o – shear modulus coefficient	-- [b]	345	560
h_{po} – contraction rate parameter	-- [b]	2.2	4.0
n_G – shear modulus exponent	0.75	1.0	--
h_o – plastic modulus ratio	0.5	--	--
e_o – initial void ratio	0.9	1.00	0.61
λ - compressibility in e-ln(p') space	0.06	0.18	0.07
ϕ'_{cv} – critical state friction angel	32°	25°	32°
$n^{b,wet}$ – bounding surface parameter	0.8	1.0	--
$n^{b,dry}$ – bounding surface parameter	0.5	--	--
n^d – dilation surface parameter	0.3	--	--
A_{do} – dilatancy parameter	0.8	--	--
$r_{up,max}$ – sets bounding p_{min}	$p_{min} = p_{cs}/8$	--	0.99
z_{max} – fabric term	$10 \leq 40(s_u/\sigma'_{vc}) \leq 20$	--	--
c_z – fabric growth parameter	100	40	150
c_ε - strain accumulation rate factor	$0.5 \leq (1.2s_u/\sigma'_{vc} + 0.2) \leq 1.3$	0.25	1.0
C_{GD} –modulus degradation factor	3.0	--	--
$C_{k\alpha f}$ – plastic modulus factor	4.0	--	--
ν_o – Poisson ratio	0.3	--	--

[a] Excluding post-shaking analysis parameters (F_{su}, PostShake, C_{GC}) and hour-glassing control parameters (cr_{hg}, c_{hg}).

[b] Required input parameter that does not have a default value.

[c] Retained default value if no entry listed.

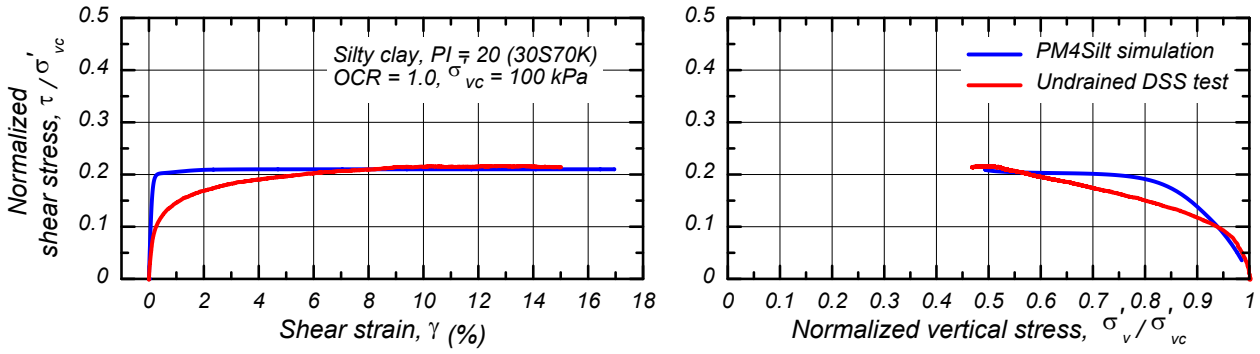

Figure 5.1. Undrained monotonic DSS loading responses for the PI = 20 silty clay.

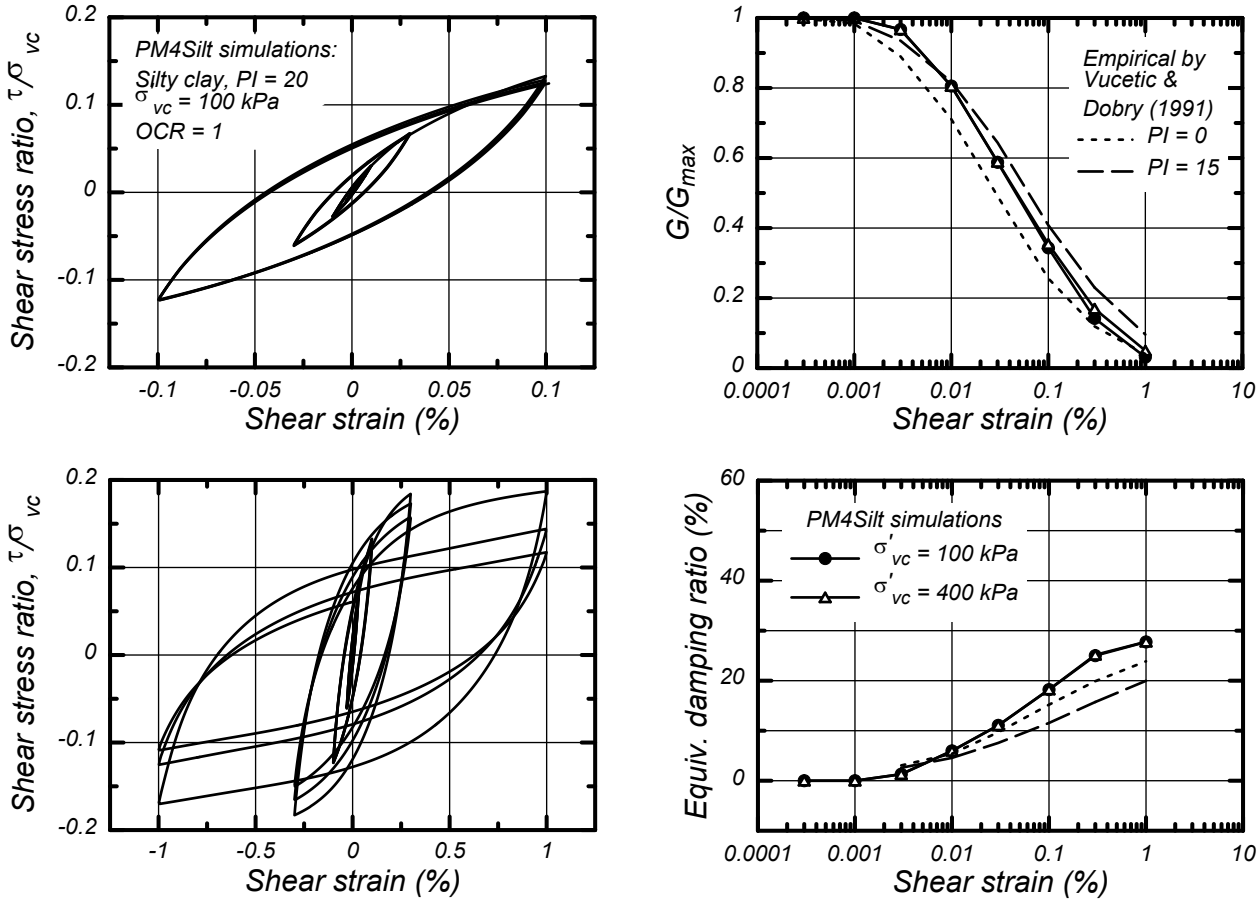

Figure 5.2. Shear modulus and equivalent damping ratios from undrained cyclic loading at different shear strain amplitudes for the PI = 20 silty clay.

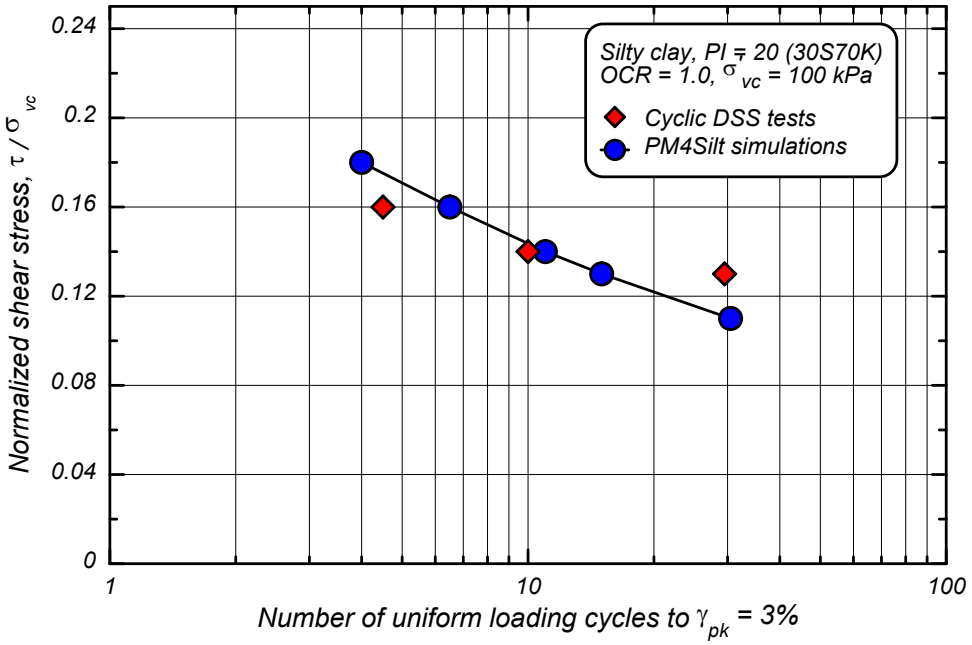

Figure 5.3. Cyclic stress ratio versus number of uniform loading cycles to cause 3% shear strain in undrained cyclic DSS loading for the PI = 20 silty clay.

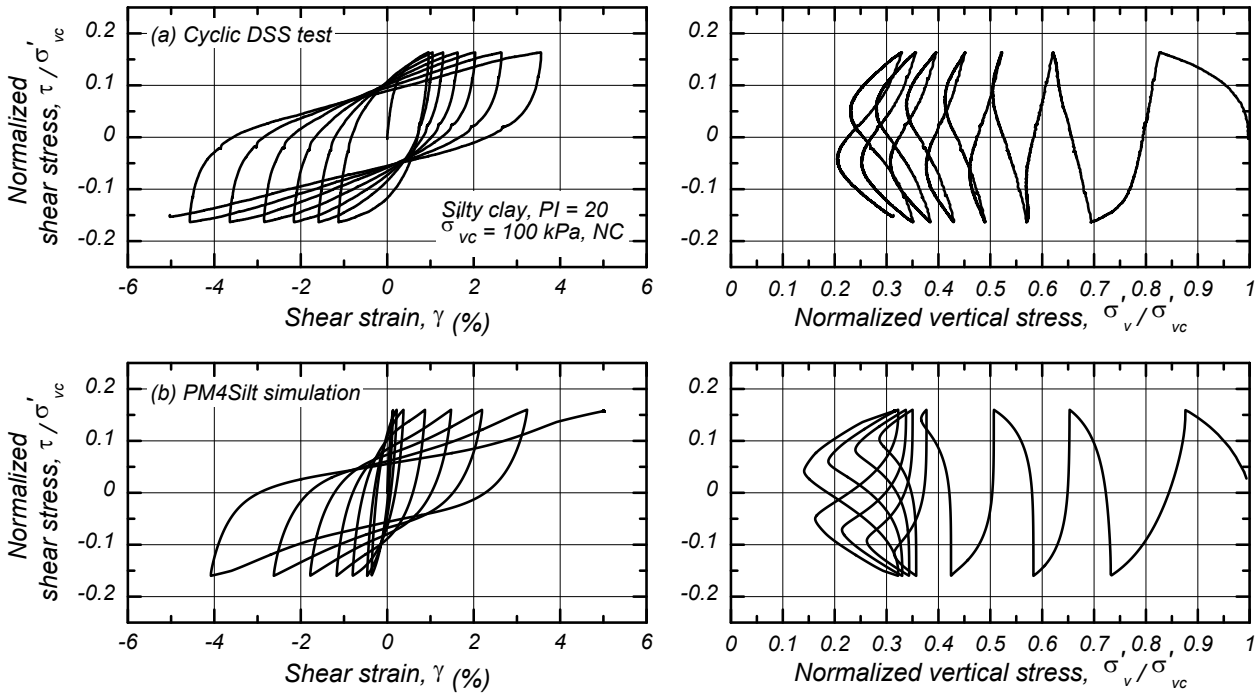

Figure 5.4. Stress-strain and stress path responses in undrained cyclic DSS loading at a relative high loading level for the PI = 20 silty clay.

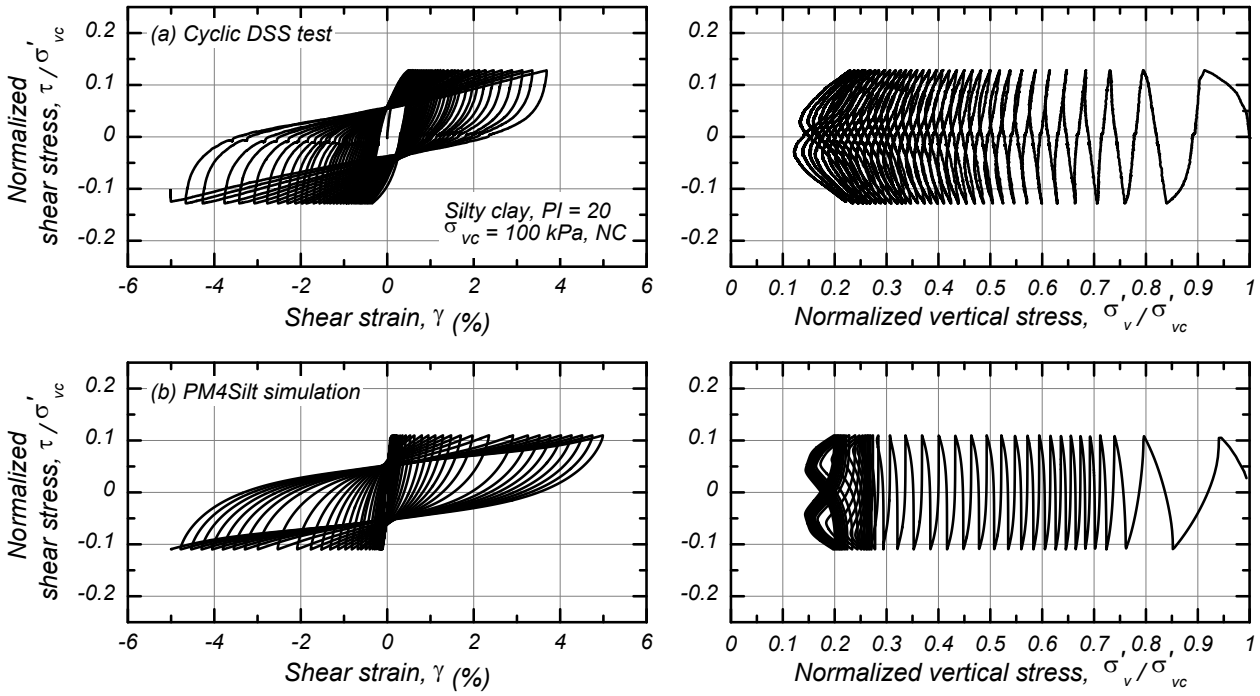

Figure 5.5. Stress-strain and stress path responses in undrained cyclic DSS loading at a relative low loading level for the PI = 20 silty clay.

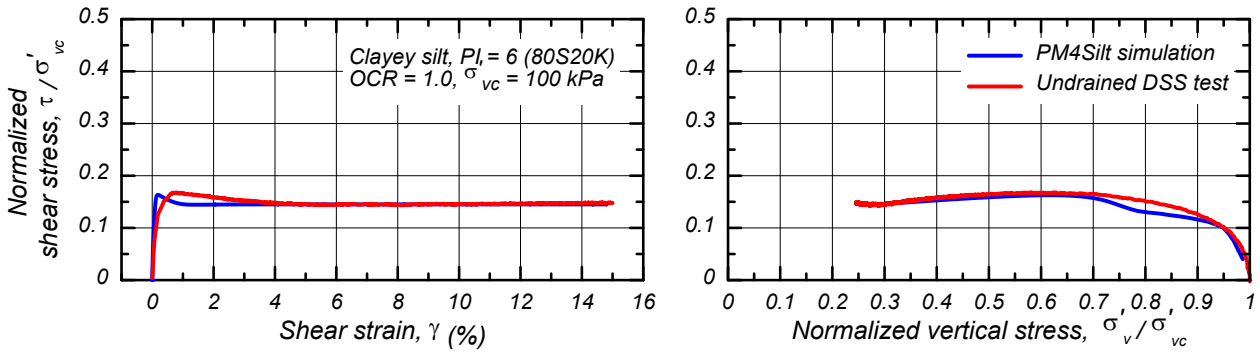

Figure 5.6. Undrained monotonic DSS loading responses for the PI = 6 clayey silt.

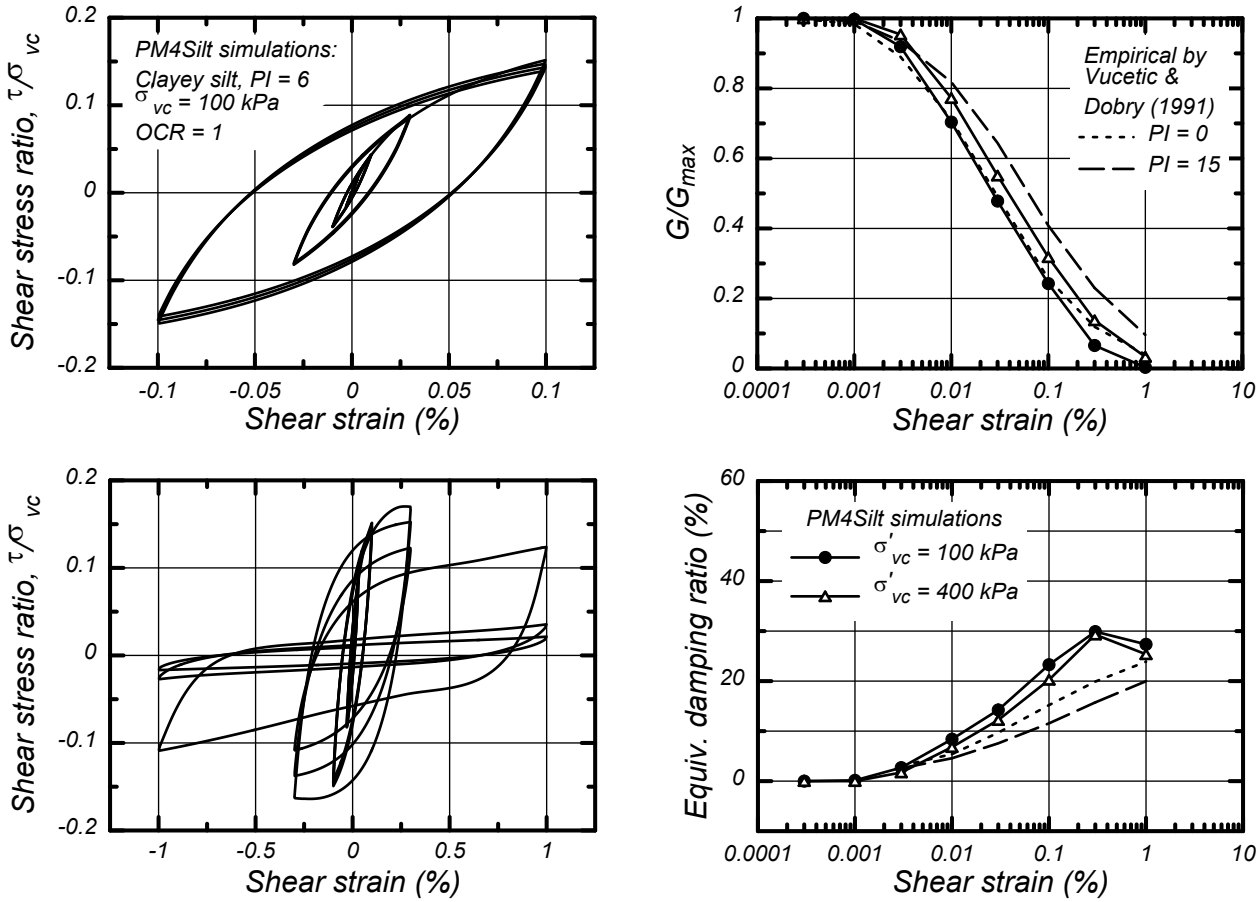

Figure 5.7. Shear modulus and equivalent damping ratios from undrained cyclic loading at different shear strain amplitudes for the PI = 6 clayey silt.

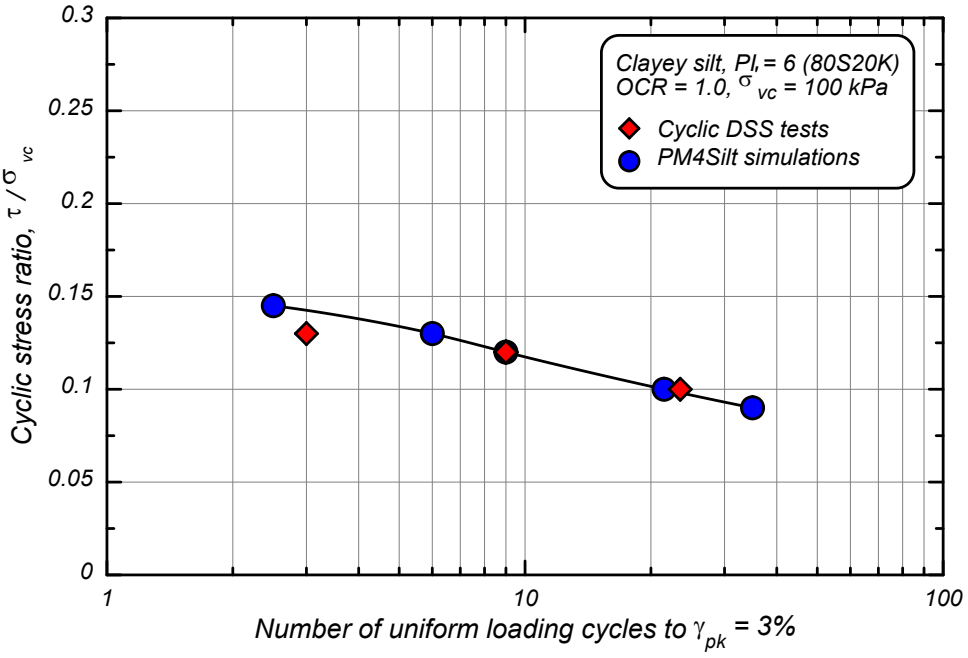

Figure 5.8. Cyclic stress ratio versus number of uniform loading cycles to cause 3% shear strain in undrained cyclic DSS loading for the PI = 6 clayey silt.

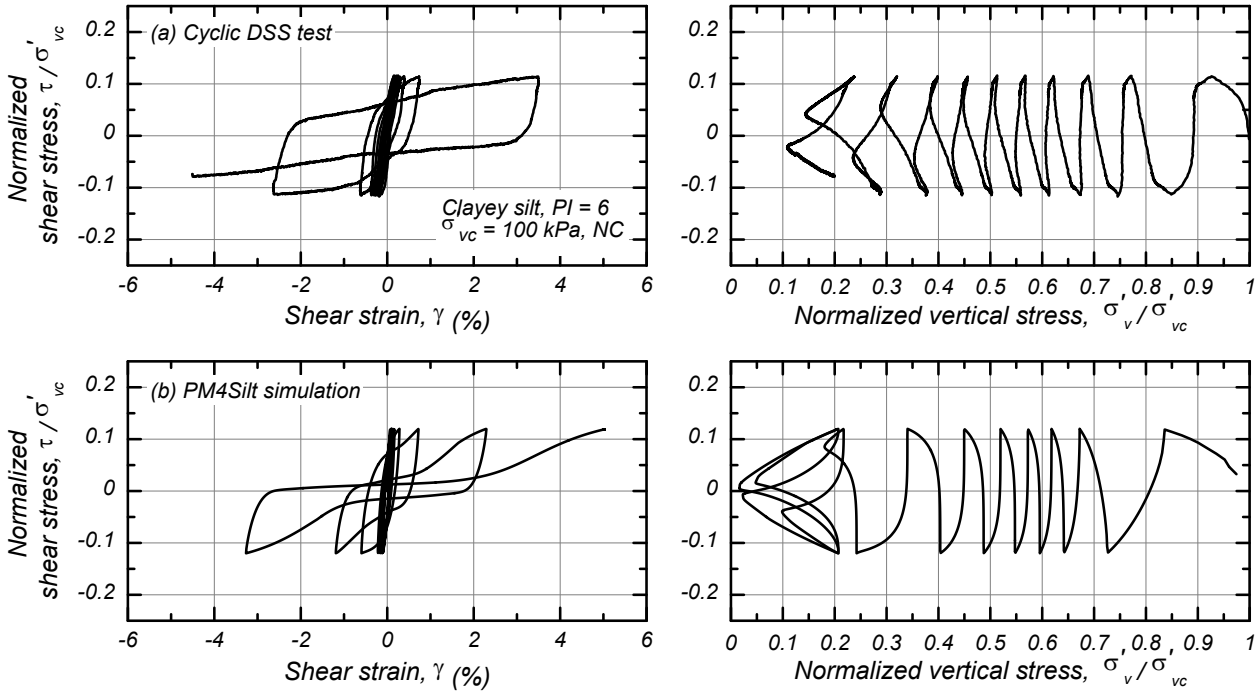

Figure 5.9. Stress-strain and stress path responses in undrained cyclic DSS loading at a relative high loading level for the PI = 6 clayey silt.

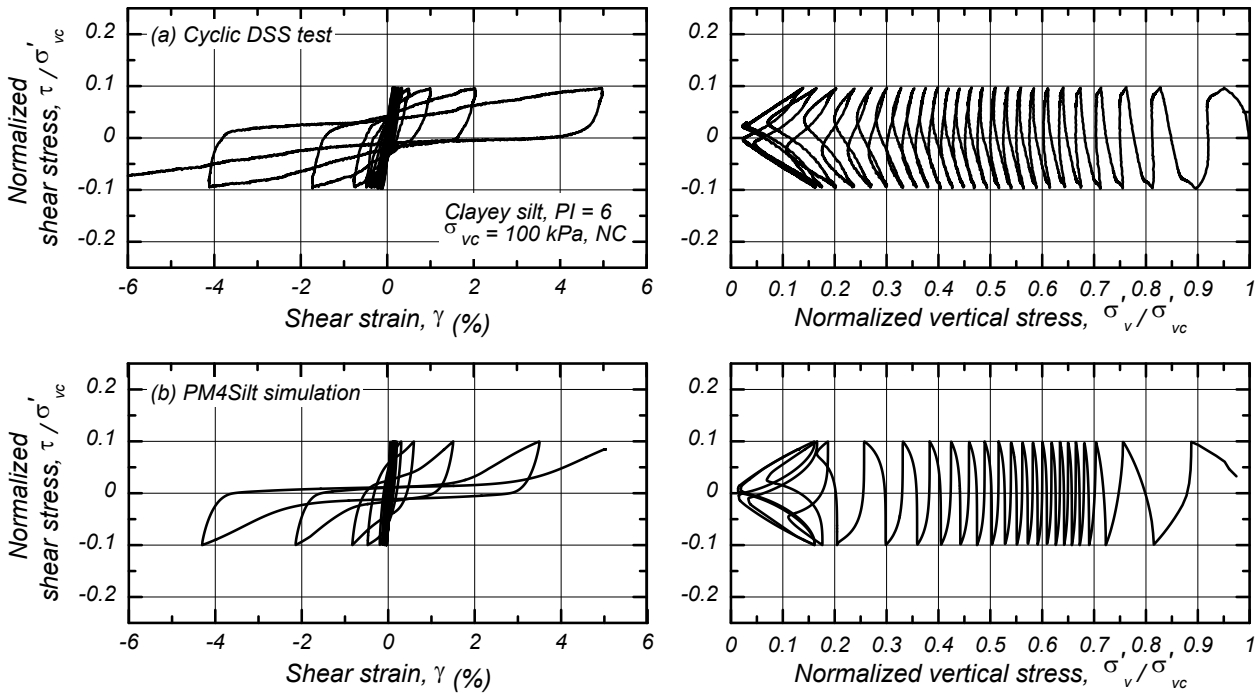

Figure 5.10. Stress-strain and stress path responses in undrained cyclic DSS loading at a relative low loading level for the PI = 6 clayey silt.

6. CONCLUDING REMARKS

The PM4Silt plasticity model was developed for representing clays and plastic silts, as opposed to purely nonplastic silts and sands, in geotechnical earthquake engineering applications. The PM4Silt model builds on the framework of the stress ratio-controlled, critical state-based, bounding surface plasticity PM4Sand model (Version 3.2) described in Boulanger and Ziotopoulou (2022) and Ziotopoulou and Boulanger (2016). Development of PM4Silt emphasized obtaining reasonable approximations of undrained monotonic shear strengths, cyclic shear strengths, and shear modulus reduction and hysteretic damping responses across a range of initial static shear stress and overburden stress conditions. Modifications to the constitutive relationships relative to PM4Sand model included:

- The model was recast in terms of the state parameter and the critical state line was changed to be linear in void ratio versus logarithm of mean effective stress space.
- The bounding surface relationship was modified for both loose (wet) and dense (dry) of critical state conditions.
- The dilatancy and contraction rate relationships were modified to allow for more direct control of the maximum excess pore pressure ratio obtained in undrained cyclic loading.
- The ability to modify the stress exponent in the elastic shear modulus relationship was added.
- An undrained shear strength reduction factor for evaluating post-strong shaking static stability was implemented.
- Default values were developed for all but three required input parameters.

The model was coded as a user defined material in a dynamic link library (DLL) for use with the commercial programs FLAC 8.1 (Itasca 2019) and FLAC2D (Itasca 2023).

The primary soil parameters are the undrained shear strength ratio (or undrained shear strength) at critical state, shear modulus coefficient, contraction rate parameter, and post-strong-shaking shear strength reduction factor. The shear modulus coefficient should be calibrated to the measured or estimated in-situ shear wave velocities. The contraction rate parameter should be calibrated to approximate the expected slope of the CRR versus number of uniform loading cycles curve. The post-strong shaking shear strength reduction factor should be selected based on the soil characteristics and shear strains that developed during strong shaking. Other secondary parameters may warrant adjustment based on site-specific laboratory test data.

The behavior of the model was illustrated by single-element simulations of undrained monotonic and cyclic loading tests for a range of initial consolidation stresses and initial static shear stress ratios important to many earthquake engineering applications. The model is stress ratio-based and therefore not applicable for modeling static consolidation problems (e.g., staged construction). The current formulation is limited to plane strain applications. Simulations presented in this report were completed using the dynamic link library (DLL) version *modelpm4silt005_64.dll* compiled on February 2, 2023 compatible with FLAC 8.1, except as noted for previously published results. The DLL module *cmodelPM4Silt2D009.dll* compiled on June 12, 2023 compatible with FLAC2D 9.00 produces the same responses. The model was shown to provide reasonable approximations of behaviors important to many earthquake engineering applications and to be relatively easy to calibrate.

ACKNOWLEDGMENTS

The development of PM4Silt progressed under projects for the California Division of Safety of Dams under Contract 4600009523, the Department of Water Resources under Contract 4600009751, and the National Science Foundation under grant CMMI-1635398. Any opinions, findings, conclusions, or recommendations expressed herein are those of the authors and do not necessarily represent the views of these organizations.

Beta versions of the model were utilized by Dr. Glenn Rix, whose feedback resulted in improvements to the model. Comments and results from trial applications by Professor Jack Montgomery, Dr. Rambod Hadidi, and Mr. Doug Wahl were also helpful and greatly appreciated. Dr. Ashraf Zekri's study of the PM4Sand model and manual resulted in improvements in both manuals as well as the creation of Figure 2.6. Dr. Tyler Oathes' work on the related PM4SiltR model resulted in improvements to the back-stress initialization routine. Feedback from Drs. Mahmood Seid-Karbasi and Mr. Viji Fernando comparing results obtained with Versions 1 and 2 identified the problem corrected in Version 2.1.

REFERENCES

Andersen, K., Kleven, A., and Heien, D. (1988). "Cyclic soil data for design of gravity structures," Journal of the Geotechnical Engineering Div., ASCE, 114(5): 517-539.

Arai, H. (2006). "Detection of subsurface V_s recovery process using microtremor and weak ground motion records in Ojiya, Japan." Third International Conference on Urban Earthquake Engineering, Tokyo Institute of Technology, Tokyo, Japan.

Azzouz, A. S., Malek, A. M., and Baligh, M. M. (1989). "Cyclic behavior of clays in undrained simple shear, J. Geotechnical Engineering Div., ASCE, 115(5): 637-657.

Been, K., and Jefferies, M. G. (1985). "A state parameter for sands." Géotechnique 35(2), 99–112.

Bolton, M. D. (1986). "The strength and dilatancy of sands." Géotechnique 36(1), 65–78.

Boulanger, R. W., Moug, D. M., Munter, S. K., Price, A. B., and DeJong, J. T. (2016). "Evaluating liquefaction and lateral spreading in interbedded sand, silt, and clay deposits using the cone penetrometer." Geotechnical and Geophysical Site Characterisation 5, B. M. Lehane, H. Acosta-Martinez, and R. Kelly, eds., Australian Geomechanics Society, Sydney, Australia, ISBN 978-0-9946261-2-7.

Boulanger, R. W., Price, A. B., and Ziotopoulou, K. (2018). "Constitutive modeling of the cyclic loading response of low plasticity fine-grained soils." GSIC 2018, Proceedings of GeoShanghai 2018 International Conference: Fundamentals of Soil Behaviours, A. Zhou et al. (Eds.), Springer Nature Singapore Pte Ltd., pp. 1–13, https://doi.org/10.1007/978-981-13-0125-4_1.

Boulanger, R. W., and Wijewickreme, D. (2019). "Calibration of a constitutive model for the cyclic loading response of Fraser River Delta Silt." Earthquake Geotechnical Engineering for Protection and Development of Environment and Constructions: Proceedings of the 7th International Conference on Earthquake Geotechnical Engineering, F. Silvestri and N. Moraci (eds), Associazione Geotecnica Italiana, Rome, Italy, ISBN 978-0-367-14328-2, 121-137.

Boulanger, R. W., and Ziotopoulou, K. (2013). "Formulation of a sand plasticity plane-strain model for earthquake engineering applications." Journal of Soil Dynamics and Earthquake Engineering, Elsevier, 53, 254-267, 10.1016/j.soildyn.2013.07.006.

Boulanger, R. W., and Ziotopoulou, K. (2022). "PM4Sand (Version 3.2): A sand plasticity model for earthquake engineering applications." Report No. UCD/CGM-22/01, Center for Geotechnical Modeling, Department of Civil and Environmental Engineering, University of California, Davis, CA.

Boulanger, R. W., and Ziotopoulou, K. (2019). "A constitutive model for clays and plastic silts in plane-strain earthquake engineering applications." Soil Dynamics and Earthquake Engineering, 127(2019): 105832, 10.1016/j.soildyn.2019.105832.

Boulanger, R. W., and Idriss, I. M. (2007). "Evaluation of cyclic softening in silts and clays." Journal of Geotechnical and Geoenvironmental Engineering, ASCE, 133(6), 641-652.

Boulanger, R. W., and Idriss, I. M. (2006). "Liquefaction susceptibility criteria for silts and clays." Journal of Geotechnical and Geoenvironmental Engineering, ASCE, 132(11), 1413-1426.

Boulanger, R. W., Meyers, M. W., Mejia, L. H., and Idriss, I. M. (1998). "Behavior of a fine-grained soil during Loma Prieta earthquake." Canadian Geotechnical Journal. 35: 146-158.

Byrne, P. M., Park, S. S., Beaty, M., Sharp, M., Gonzalez, L., and Abdoun, T. (2004). "Numerical modeling of liquefaction and comparison with centrifuge tests." Canadian Geotechnical Journal. 41 (2): 193-211.

Cubrinovski, M., and Ishihara, K. (1998). "State concept and modified elastoplasticity for sand modelling." Soils and Foundations; 38(4): 213-225.

Dafalias, Y. F. (1986). "Bounding surface plasticity. I: Mathematical foundation and hypoplasticity." Journal of Engineering Mechanics, 112(9), 966-987.

Dafalias, Y. F., and Manzari, M. T. (2004). "Simple plasticity sand model accounting for fabric change effects." Journal of Engineering Mechanics, ASCE, 130(6), 622-634.

Dafalias Y. F., Manzari M. T., and Papadimitriou, A. G. (2006). "SANICLAY: simple anisotropic clay plasticity model." International Journal for Numerical and Analytical Methods in Geomechanics; 30(12):1231–1257.

Dafalias, Y.F., and Taiebat, M. (2016). Sanisand-Z: Zero elastic range sand plasticity model. Géotechnique 66, 999–1013, 10.1680/jgeot.15.P.271.

Dahl, K. R., DeJong, J. T., Boulanger, R. W., Pyke, R., and Wahl, D. (2014). "Characterization of an alluvial silt and clay deposit for monotonic, cyclic and post-cyclic behavior." Canadian Geotechnical Journal, 51(4): 432-440, 10.1139/cgj-2013-0057.

Dahl, K. R. (2011). "Evaluation of seismic behavior of intermediate and fine-grained soils." Doctoral thesis, University of California, Davis.

Dahl, K. R., Boulanger, R. W., DeJong, J. T., and Driller, M. W. (2010). "Effects of sample disturbance and consolidation procedures on cyclic strengths of intermediate soils." Fifth International Conference on Recent Advances in Geotechnical Earthquake Engineering and Soil Dynamics, San Diego, CA, paper OSP-1.

Dawson, E. M., Roth, W. H., Nesarajah, S., Bureau, G., and Davis, C. A. (2001). "A practiceoriented pore pressure generation model." Proceedings, 2nd FLAC Symposium on Numerical Modeling in Geomechanics. Oct. 29-31, Lyon, France.

Duque, J., Yang, M., Fuentes, W., Masin, D., and Taiebat, M. (2021). Characteristic limitations of advanced plasticity and hypoplasticity models for cyclic loading of sands. Acta Geotechnica, 10.1007/s11440-021-01418-z.

Hoeg, K., Dyvik, R., and Sandbaekken, G. (2000). "Strength of undisturbed versus reconstituted silt and silty sand specimens." Journal of Geotechnical and Geoenvironmental Engineering, ASCE, 126(7), 606-617.

Hu C., and Liu H. (2015). "A new bounding-surface plasticity model for cyclic behaviors of saturated clay." Communications in Nonlinear Science and Numerical Simulation, 22, 101-119, 10.1016/j.cnsns.2014.10.023.

Hyodo, M., Yamamoto, Y., and Sugiyama, M. (1994). "Undrained cyclic shear behavior of normally consolidated clay subjected to initial static shear stress," Soils and Foundations, JSSMFE, 34(4), 1-11.

Itasca (2019). FLAC – Fast Lagrangian Analysis of Continua, Version 8.1, Itasca Consulting Group, Inc., Minneapolis, Minnesota.

Itasca (2023). FLAC2D – Fast Lagrangian Analysis of Continua, Version 9.00 – Pre-Release1, Itasca Consulting Group, Inc., Minneapolis, Minnesota.

Kokusho, T., Yoshida, Y., and Esashi, Y. (1982). "Dynamic properties of soft clay for wide strain range." Soils and Foundations, 22(4), 1–18.

Ladd, C. C., and Foott, R. (1974). "New design procedure for stability of soft clays." Journal of the Geotechnical Engineering Div., ASCE, 100(7), 763-786.

Lefebvre, G., and Pfendler, P. (1996). "Strain rate and preshear effects in cyclic resistance of soft clay." Journal of Geotechnical and Geoenvironmental Engineering, ASCE, 122(1), 21-26.

Lefebvre, G., and LeBouef, D. (1987). "Rate effects and cyclic loading of sensitive clays," Journal of Geotechnical Engineering, ASCE, 113(5), 476-489.

Manzari, M. T., and Dafalias, Y. F. (1997). "A critical state two-surface plasticity model for sand." Géotechnique, 47(2), 255-272.

Moriwaki, Y., Akky, M. R., Ebeling, R., Idriss, I. M., and Ladd, R. S. (1982). "Cyclic strength and properties of tailing slimes." Specialty Conference on Dynamic Stability of Tailings Dams, Preprint 82-539, ASCE.

Ni J., Indraratna B., Geng X.-Y., Carter, J. P., and Chen Y. L. (2015). "Model of soft soils under cyclic loading." International Journal of Geomechanics, ASCE, 04014067, 10.1061/(ASCE)GM.1943-5622.0000411.

Papadimitriou, A. G., Bouckovalas, G. D., and Dafalias, Y. F. (2001). "Plasticity model for sand under small and large cyclic strains." Journal of Geotechnical and Geoenvironmental Engineering, 127(11), 973-983.

Pestana, J. M., and Whittle, A. J. (1999). "Formulation of a unified constitutive Model for clays and sands." International Journal for Numerical and Analytical Methods in Geomechanics, 23: 125-1243.

Price, A. B., Boulanger, R. W., DeJong, J. T., Parra Bastidas, A. M., and Moug, D. M. (2015). "Cyclic strengths and simulated CPT penetration resistances in intermediate soils." 6th International Conference on Earthquake Geotechnical Engineering, November 1 4, Christchurch, New Zealand.

Price, A. B., DeJong, J. T., and Boulanger, R. W. (2017). "Cyclic loading response of silt with multiple loading events." Journal of Geotechnical and Geoenvironmental Engineering, ASCE, 2017, 143(10): 04017080, 10.1061/(ASCE)GT.1943-5606.0001759.

Qiu, Z., and Elgamal, A. (2020). Three-dimensional modeling of strain-softening soil response for seismic-loading applications. Journal of Geotechnical and Geoenvironmental Engineering, 146(7): 04020053, 10.1061/(ASCE)GT.1943-5606.0002282.

Richart, F. E., Jr., Hall, J. R., and Woods, R. D. (1970). "Vibration of soils and foundations." International series in theoretical and applied mechanics, Prentice-Hall, Englewood Cliffs, N.J.

Romero, S. (1995). "The behavior of silt as clay content is increased." MS thesis, University of California, Davis, 108 pp.

Rowe, P. W. (1962). "The stress-dilatancy relation for static equilibrium of an assembly of particles in contact." Proc. R. Soc. London, Ser. A, 269, 500-527.

Seidalinov G., and Taiebat M. (2014). "Bounding surface SANICLAY plasticity model for cyclic clay behavior." International Journal for Numerical and Analytical Methods in Geomechanics, 38: 702-724.

Sheahan, T. C., Ladd, C. C., and Germaine, J. T. (1996). "Rate-dependent undrained shear behavior of saturated clay." Journal of Geotechnical Engineering, 122(2), 99-108.

Taiebat M., Dafalias Y. F., and Peek R. (2010)."A destructuration theory and its application to SANICLAY model." International Journal for Numerical and Analytical Methods in Geomechanics, 34(10):1009–1040.

Vucetic, M., and Dobry, R. (1991). "Effect of soil plasticity on cyclic response." Journal of Geotechnical Engineering, 117(1), 89–107.

Wang, Z. L., Dafalias, Y. F., and Shen, C. K. (1990). "Bounding surface hypoplasticity model for sand." Journal of Engineering Mechanics, ASCE, 116(5), 983-1001.

Woodward-Clyde Consultants (1992a). "California Water Operations Center – Site Evaluation and Remediation – Conceptual Design. Appendix E: CWOC Site Characterization Memo. " Oakland, California.

Woodward-Clyde Consultants (1992b). Seismic Stability Evaluation and Piezometer Installation, Tailing Pond No. 7. Denver, Colorado.

Yang, M., Taiebat, M., Dafalias, Y. (2022). SANISAND-MSf: a memory surface and semifluidized state enhanced sand plasticity model for undrained cyclic shearing. Géotechnique, 10.1680/jgeot.19.P.363.

Yang, Z., Elgamal, A., and Parra, E. (2003). "Computational model for cyclic mobility and associated shear deformation." Journal of Geotechnical and Geoenvironmental Engineering, ASCE, 129(12), 1119-1127.

Yang Z., Lu J. L., and Elgamal A. (2008). "OpenSees soil models and solid-fluid fully coupled elements: User's manual, Version 1.0." Department of Structural Engineering, University of California, San Diego.

Yu, P., and Richart, F. E., Jr. (1984). "Stress ratio effects on shear modulus of dry sands." J. Geotechnical Engineering, ASCE, 110(3), 331-345.

Zergoun, M., and Vaid, Y. P. (1994). "Effective stress response of clay to undrained cyclic loading," Canadian Geotechnical Journal, 31, 714–727.

Ziotopoulou, K., and Boulanger, R. W. (2012). "Constitutive modeling of duration and overburden effects in liquefaction evaluations." 2nd International Conference on Performance-Based Design in Earthquake Geotechnical Engineering, ISSMGE, Taormina, Italy, May 28-30, paper no. 03.10, 467-482.

Ziotopoulou, K., and Boulanger, R. W. (2013). "Calibration and implementation of a sand plasticity plane-strain model for earthquake engineering applications." Journal of Soil Dynamics and Earthquake Engineering, 53, 268-280, 10.1016/j.soildyn.2013.07.009.

Ziotopoulou, K., and Boulanger, R. W. (2016). "Plasticity modeling of liquefaction effects under sloping ground and irregular cyclic loading conditions." Soil Dynamics and Earthquake Engineering, 84 (2016), 269-283, 10.1016/j.soildyn.2016.02.013.